Phase Mixed Alfvén Waves in Partially Ionised Solar Plasmas

Max McMurdo

Supervisors:
Dr Istvan Ballai
Dr Gary Verth
Professor Viktor Fedun

The University Of Sheffield.

University of Sheffield

School of Mathematics and Statistics

A thesis submitted in partial fulfilment of the requirements for the degree of

Doctor of Philosophy

May 2024

Acknowledgements

I want to thank my mother, for being my sounding board over the past three and a half years, I think you probably know as much as I do about phase mixed Alfvén waves in partially ionised plasmas. I want to thank my father, for showing me what hard work can achieve, thank you for your unwavering support.

I would like to thank Istvan Ballai for his consistent support throughout my time as a doctoral student at Sheffield, you showed me the standard I should hold myself to. I will take this forward throughout my career. I want to thank Viktor Fedun who was always in my corner, you gave me confidence in myself and my abilities, you truly showed me how to enjoy the academic lifestyle. I want to thank Gary Verth for never blowing smoke up my arse until I deserved it, you have been my tutor ever since I came to Sheffield as an undergraduate and encouraged me to pursue a career in academia.

Last but not least, I want to thank me. I want thank me for doing all this hard work and never quitting.

Declaration of Authorship

I hereby declare that, except where clear reference is made to the work of others, the contents of this dissertation are original and have not, in whole or in part, been submitted to this or any other university for consideration for any other degree or qualification. This dissertation is my own work and contains nothing which is the outcome of work done in collaboration with others, except as specified in the text and Acknowledgements.

Max McMurdo
May 2024

List of Publications

- McMurdo, M., Ballai, I., Verth, G. & Fedun, V., "Phase Mixing of Propagating Alfvén Waves in a Single-fluid Partially Ionized Solar Plasma", 2023, The Astrophysical Journal, 958, 81.
- Ballai, I., Forgács-Dajka, E., McMurdo, M., "Parametric resonance of Alfvén waves driven by ionization-recombination waves in the weakly ionized solar atmosphere", 2024, Philosophical Transactions of the Royal Society A, 382, 2272.
- Aldhafeeri, A., Verth, G., Brevis, W., Jess, D., McMurdo, M., Fedun, V., "Magnetohydrodynamic Wave Modes of Solar Magnetic Flux Tubes with an Elliptical Cross Section", The Astrophysical Journal, 912, 50.

Contents

List of Figures

List of Tables

CHAPTER 1
Introduction

1.1 Background and context

Solar physics encompasses the investigation of the Sun's evolution, dynamics, and behaviors within the framework of the Sun-Earth relation, using a wide range of techniques. Although the last few decades has seen an exponentially increasing wealth of observations at high resolution and high cadence, we are still very far from fully understanding important aspects of how our star works, and how it influences life on Earth. Observations provide key results that can drive theoretical (analytical and numerical) studies, but also serve as validations of previous theoretical results. Observations have changed the theoretical field in so many ways by imposing constraints on modelling.

Numerical simulations, often referred to as synthetic observations, can provide insight into what is not yet observationally verifiable. They are not bound by the resolution limits of solar telescopes, which struggle to resolve coherent structures smaller than a few hundred kilometers. Numerical models are able to resolve far smaller intricacies, since the resolution is often a user defined quantity. With the advancements of solar telescopes, perhaps one day we may be able to forego numerical simulations, as it could be possible to resolve even the smallest features of the Sun with a high powered quantum telescope. However, for now, there are two distant parties sitting across the same table, one arguing about what we can model and the other about what we can see, both working to meet in the middle.

Plasma is the most common form of matter, it is present in hot stars and near other celestial bodies. Plasma is often defined as the collection of charged and neutral particles that show a collective behaviour. Due to the existence of charges, plasmas are permeated by electric and magnetic fields that control the dynamical and thermodynamical state as well as the stability of the plasma. Our Sun is the only feasible star that we can study that contains

plasma under extreme conditions, its study can lead to profound insights into the evolution of other astronomical objects and their enduring influence on the universe surrounding us. To understand why we take such an interest in the Sun rather than any other star, we can compare the observational results obtained in the case of a near star and our Sun. Figure 1.1 displays the highest resolution image of a relatively near star to Earth taken by the Atacama Large Millimeter/submillimeter Array (ALMA), the most powerful radio telescope in the world. In this figure, one pixel equates to approximately 2×10^5 km.

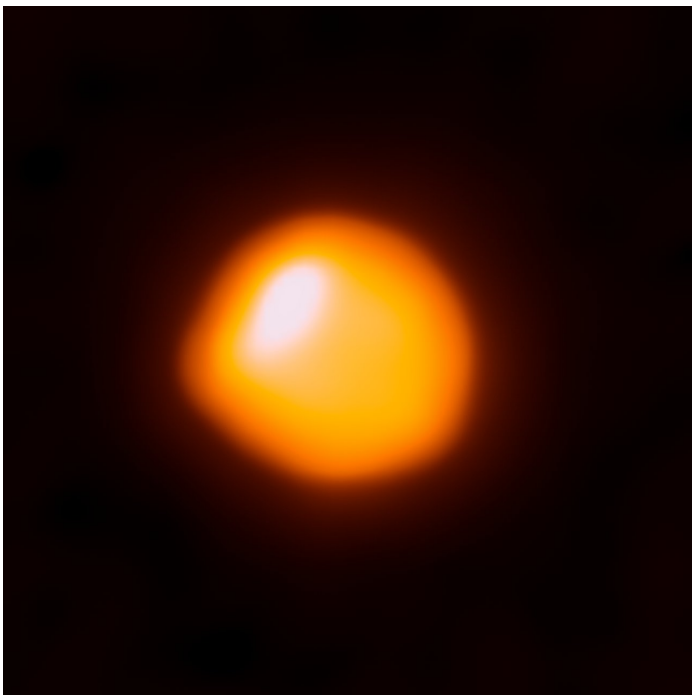

Figure 1.1: Image of Betelgeuse, a red supergiant star approximately 650 million light years away from Earth, taken by the ALMA telescope. Image courtesy of O'Gorman et al. (2017).

In contrast, the image shown in Fig. 1.2 displays the entire disk of the Sun as seen by Solar Orbiter in extreme ultraviolet light from a distance of about 75 million kilometers with a resolution of approximately $50 - 100$ km/pixel. The differences speak for themselves, but it is clear we can use images such as the one shown in Figure 1.2 to far greater effect to study coherent structures using the framework of plasma physics. The Daniel K. Inouye Solar Telescope (DKIST), which became operational in the last year can provide observations with unprecedented resolution of the order of 8 km/pixel, which will revolutionise our understanding in many ways. Comparing this value with the approximate resolution of the image taken by the ALMA telescope means we can resolve features approximately 10^4 times smaller on the Sun than Betelgeuse.

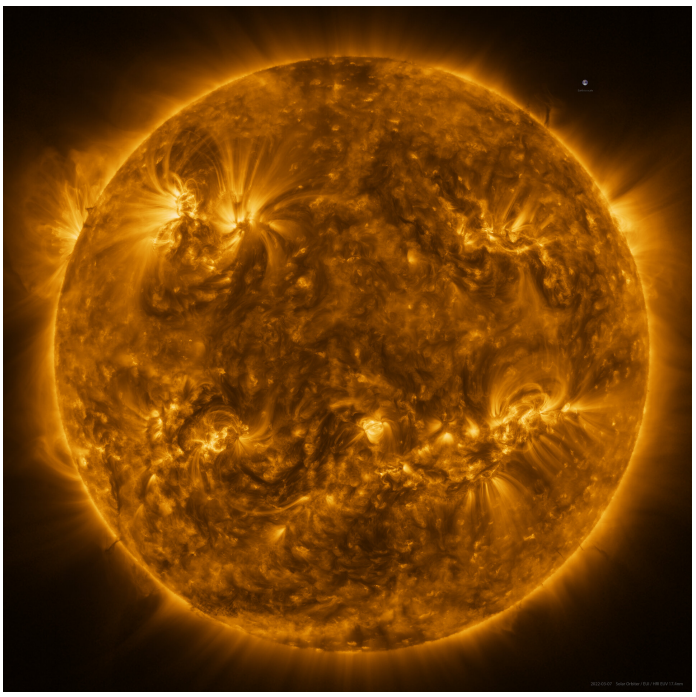

Figure 1.2: Full solar disk obtained by the Solar Orbiter space telescope in extreme ultraviolet wavelengths (EUV). Many small scale structures are clearly visible such as coronal loops and spicules on the disk edge, as well as bright active regions. Image courtesy of ESA & NASA/Solar Orbiter/EUI team; Data processing: E. Kraaikamp (ROB).

Solar spectroscopy is a technique that separates light from the Sun into constituent spectra and looks for the presence or absence of particular lines that give hints regarding the chemical composition of the plasma and its ionisation degree. Spectroscopic studies during solar eclipses can examine the atmosphere of the Sun in great detail and are able to provide better understanding of the composition of the solar atmosphere. In 1869, Harkness and Young discovered a prominent spectral line during the total solar eclipse of August 7 (Lockyer, 1869). The result shown by Figure 1.3 was taken through a green narrow-band filter on the wavelength of the most intense coronal spectral line. For 70 years scientists were left puzzled as to identify the element responsible for the line and through a combination of optimism and despair named the element Coronium. The problem was solved by Grotrian (1939) and independently by Edlén (1945), who observed spectral lines emitted by iron (as well as calcium and nickel) in high stages of ionisation. Specifically, today we know that the result observed by Harkness and Young is, in fact, caused by the spectroscopic light corresponding to an iron atom that was stripped of 13 electrons (Fe XIV). In order to have an atom in this state, one needs temperatures of the order of a few million degrees Kelvin.

The Sun is made up of a large range of elements in various stages of ionisation, with each element contributing towards a certain percentage of the total composition of the Sun. The relative populations of each element present in the Sun are given in Table 1.1. It is believed that the chemical composition presented in this table is representative for the entire Sun with the exception of the solar core due to the substantial mixing of the Sun's interior and extremely high pressure. In total, 67 elements have been detected in the solar spectrum, those not listed here are present in even smaller quantities.

The high temperature of the solar atmosphere (required to produce Fe XIV) was a result that puzzled solar scientists even more, as this result was against every model of a star. This finding was the very first step into what today is known as probably the most mysterious aspect of the Sun, the famous *coronal heating problem* or even better, the *atmospheric heating problem*, whose explanation still eludes us. Studies were carried out to estimate the temperature of the solar surface. Stefan, in 1879, formulated that the luminosity of an object is proportional to the fourth power of surface temperature, predicting a value of the temperature at the surface of the Sun of 5700 K. While initially Stefan's law was not generally accepted, Langley wrote in Hoskin et al. (1900) that *it is probable from all experiments made to date, that the solar effective*

Element	% number of atoms	% total mass
Hydrogen	91.2	71.0
Helium	8.7	27.1
Oxygen	0.078	0.97
Carbon	0.043	0.40
Nitrogen	0.0088	0.096
Silicon	0.0045	0.099
Magnesium	0.0038	0.076
Neon	0.0035	0.058
Iron	0.0030	0.14
Sulfur	0.0015	0.040

Table 1.1: The chemical composition of the photosphere and chromosphere derived from spectroscopic analysis (Lodders, 2003).

temperature is not less than $3,000$ *nor more than* $30,000$ *degrees of the centigrade thermometer*. Further estimates were deduced from black body radiation curves in the late 20^{th} century and the accepted modern value for the solar surface is considered to be approximately $6,000$ K. This result added another twist in the problem of solar atmospheric heating and the question translated into asking what mechanism(s) are acting in the atmosphere of the Sun that can produce the increase in temperature by many orders of magnitude. The need to have heating mechanisms acting in the solar atmosphere can be substantiated through very simple reasoning. Idealistically one can expect that the temperature from a source decays with distance according to an inverse square law, i.e., it decays as $1/r^2$, where r denotes the distance from the source. Assuming a solar surface temperature of 6,000 degrees K, an observer would measure the average temperature at the Earth's magnetosphere (the boundary where the Earth's magnetic field influences solar wind particles) should drop to approximately 0.1 K. Direct measurements have found this area to be in the region of tens of thousands of K. This significant discrepancy indicates that additional heating mechanisms must be at work beyond the simple inverse square law, requiring us to explore more complex processes to explain the observed high temperatures in the solar atmosphere.

To better understand how the temperature of the solar atmosphere varies

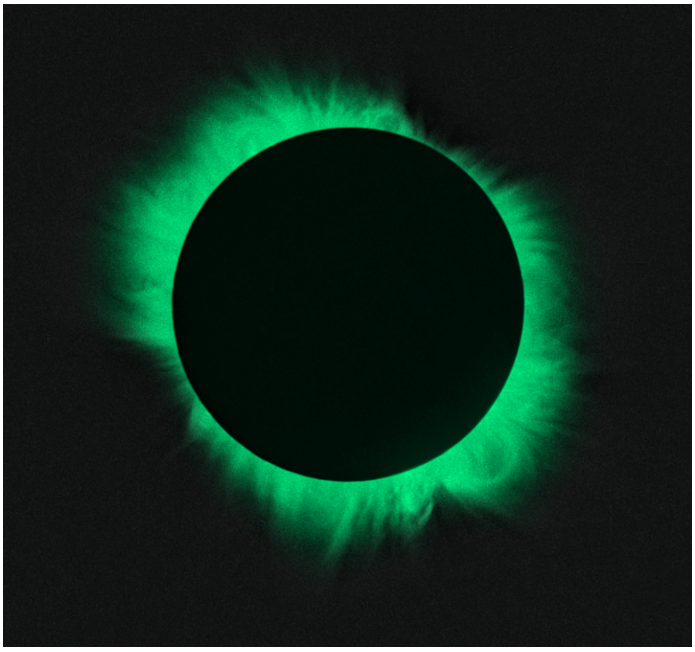

Figure 1.3: Image taken during a total solar eclipse of July 31, 1981, in Bratsk (Russia). The image was taken through a green narrow-band filter 530.3 nm (0.2 nm half-width) on Fomapan N30 film and later processed using Corona software in 2007. Image courtesy of Július Sýkora and Miloslav Drukmüller.

with height one can use one of the standard solar atmospheric models (e.g., the VAL, AL, FAL, models) that return the values of the temperature, pressure and number density of particles with height above the solar surface. These values were obtained by averaging the results drawn from several spectroscopic lines that are emitted in various locations in the solar atmosphere. A typical variation of the temperature and total number density of particles with height is given by Figure 1.4. Given the significantly lower abundance of all other elements compared with hydrogen (as shown in Table 1.1), we omit additional elements from our investigation. This assumption allows us to consider a quasi-neutral plasma, so, we equate the number density of ions with that of electrons.

The formation conditions of many spectral lines observed by various instruments show that the temperature in the solar atmosphere undergoes a gradual increase from the temperature minimum in the photosphere (first layer of the atmosphere) through the chromosphere (second layer of the atmosphere), to a very steep increase in the narrow transition region and reaches values of several million degrees in the solar corona (outer atmosphere). The energy in the upper part of the solar atmosphere is lost due to, e.g., radiation and this needs to be compensated by mechanisms that can balance the loss.

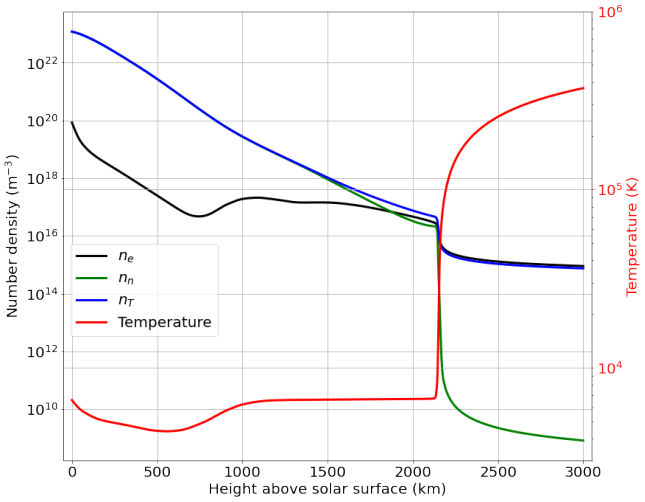

Figure 1.4: The variation of the electron (n_e), neutral (n_n), total (n_T) number densities and temperature for altitudes corresponding to the lower solar atmosphere are presented based on the data extracted from the AL C7 model (Avrett and Loeser, 2008).

The fundamental scenario of heating implies the generation of heat somewhere in the solar atmosphere, however, this aspect (and taking into account the realistic parameters of the Sun) means that in reality, we have a conversion of various energies into heat. When we discuss the problem of heating, we have to understand that a general heating process is a multi-faceted problem, i.e., the heating model of the solar atmosphere should be able to explain aspects such as the source of the energy, how this energy is transported into the location where heating is needed and how it is dissipated into heat. Nowadays it is widely accepted that the reservoir of energy resides in the granular buffeting of magnetic field lines in the solar photosphere (see, e.g., Roberts, 1979; Evans and Roberts, 1990; Ballai et al., 2006; Vigeesh et al., 2012; Mumford et al., 2015; Stangalini et al., 2017). As a result, the generated energy can appear as kinetic energy (waves, flows) or magnetic energy in the form of magnetic stresses deposited in magnetic field lines.

Waves are ideal tools to transport energy, however, the way they dissipate this energy is problematic. In a non-ideal, dissipative plasma, waves undergo damping resulting in a transfer of their kinetic energy into heat, however, given the realistic values of transport coefficients, this damping is not very efficient, as damping lengths can often be of the order of several solar radii (Cranmer and van Ballegooijen, 2005). Theoretical results of the last few decades confirmed that waves can damp their energy and contribute to the heating of

the solar atmospheric plasma only when this heating occurs over very short length scales (see, e.g., Klimchuk, 2006; van Ballegooijen et al., 2011). While for mechanisms such as turbulence, the creation of small scales is a natural aspect, in the case of waves the situation is far from obvious. Although effects such as dispersion create naturally small scales, these were not shown to be sufficient for effective damping to take place (Ballai et al., 2019). Currently, two proposed mechanisms are able to satisfy the requirements: resonant absorption and phase mixing.

Resonant absorption, first proposed by Ionson (1978) as a heating mechanism for coronal loops is based on the fact that in a plasma with transversal inhomogeneity, the spectrum of waves becomes continuous. An effective wave energy transfer occurs between incident waves and the plasma if the frequency of the wave lies in the frequency continuum of the plasma. In this situation, the energy of the wave is transferred to the local perturbations in the inhomogeneous regions of the magnetic structure, leading to a growth in the amplitude (Davila, 1987; Sakurai et al., 1991*a*,*b*; Goossens et al., 1995; Goossens and Ruderman, 1995; Erdélyi et al., 1999; Cally and Andries, 2010). The growth of the amplitude leads to nonlinear behaviour of waves near the resonant point that can be balanced by dissipative processes that do not need to be excessively large for resonant absorption to work effectively and dissipate the energy of the wave to heat the surrounding plasma. The theory of resonant absorption predicts a damping time of kink waves that is proportional to the period of waves and was proposed by Ruderman and Roberts (2002) to explain the rapid damping of kink oscillations of coronal loops. For a review of the theory of resonant absorption of kink waves see, e.g., Goossens et al. (2011).

The other proposed model to address the deposition of waves' energy into the plasma is through the so-called phase mixing of waves, which constitutes the subject of the present thesis. Broadly speaking, the theory of phase mixing states that waves, propagating along neighbouring field lines in a plasma (which is permeated by a magnetic field) that exhibits transversal inhomogeneity in the background magnetic field, density, or both, will quickly oscillate out of phase with one another. As this mixing progresses the transversal gradients between the magnetic surfaces with which the waves are propagating becomes larger, enhancing the dissipative mechanisms which act to damp the waves more effectively. Although, very often, phase mixing requires very small-scale inhomogeneities (sometimes below the spatial resolution of the current observational facilities), observations of waves in inhomogeneous plasma (such as in

spicules, prominences and fibrils) are nowadays ubiquitous (see, e.g., He et al., 2009; Okamoto and De Pontieu, 2011; Hillier et al., 2013; Gafeira et al., 2017; Jafarzadeh et al., 2017; Bate et al., 2022). Magnetoconvection codes have also shown to produce such transversal density enhancements in fibrils and spicules due to magnetic forces (see, e.g., Leenaarts et al., 2015, 2012; Martínez-Sykora et al., 2011; Martínez-Sykora et al., 2017).

The magnetic field in the solar plasma is not diffuse, rather, it tends to accumulate into larger or smaller structures that exhibit inhomogeneity (see, e.g., Rezaei et al., 2012; Sobotka et al., 2013; Schlichenmaier et al., 2016; Bellot Rubio and Orozco Suárez, 2019; Jafarzadeh et al., 2019). Sunspots occur in regions of an intense magnetic field that emerges from the Sun's surface. This provides an ideal pathway for wave propagation while also exhibiting significant transverse inhomogeneity, as evidenced by intensity observations by Stangalini et al. (2022). Sunspots form active regions that are often associated with solar flares (Aschwanden et al., 1999*a*). They appear as dark and cold spots (the umbra) surrounded by a more striated and structured penumbra. Sunspots vary in size (typically 10 - 100 Mm in diameter) and shape, and are transient, appearing and disappearing over days to weeks. Magnetic pores are somewhat comparable to a small-scale sunspot since they also appear as cold, dark regions of plasma associated with heightened solar activity, albeit with weaker magnetic fields compared to sunspots. Unlike sunspots, they are much smaller in size (typically 1-10 Mm in diameter) and lack a penumbra. Morton et al. (2011) observed MHD sausage modes in magnetic pores with periods between 30 - 450 s, while Albidah et al. (2022) evidenced higher order fluting modes for the first time, additional studies by Albidah et al. (2021, 2023*a*,*b*) demonstrate a wealth of evidence for oscillating modes present in sunspots. In addition to sunspots and pores, the solar magnetic field forms other structures, such as bright plages and faculae observed, for instance, using the balloon-borne SUNRISE solar observatory (Solanki et al., 2010). Plages, best observed in H_α (a spectral line of hydrogen that lies within the visible spectrum), are large more diffuse bright regions typically observed in the chromosphere and are often found near sunspots where often spicules are observed to carry Alfvén waves with significant amplitudes of the order 20 kms^{-1} (de Pontieu et al., 2007). Faculae, on the other hand, are smaller bright regions usually observed in the photosphere, particularly in the vicinity of sunspots (Keller et al., 2004). Like plages, they are associated with strong magnetic fields, but they are best observed near the solar limb in white light. While both features are

manifestations of strong magnetic activity, their distinction lies in their size and location within the solar atmosphere.

Over the past decades, a large number of studies have addressed the problem of coronal heating, with a variety of mechanisms being proposed to explain the multi-million-degree solar corona (see, e.g., Osterbrock, 1961; Brueckner and Bartoe, 1983; Heyvaerts and Priest, 1984; Hudson, 1991; Shimizu, 1995; Matthaeus et al., 1999; Klimchuk, 2006; Tomczyk et al., 2007; Cranmer et al., 2007; van Ballegooijen et al., 2011; van der Holst et al., 2014*a*). To a certain extent, the corona is a simpler environment to model. With the exclusion of coronal loops, the magnetic field is mostly vertical (especially in polar regions and coronal holes), with flows being field-aligned, the plasma very tenuous and optically thin, and temperatures that are high enough so that at least the hydrogen (the most abundant element in the solar plasma) is fully ionised. However, the problem of atmospheric heating is not necessarily connected only to the solar corona. The height-dependence of the temperature suggests that the heating of the corona is a process where the chromosphere also plays a key role and here the description of heating processes requires much more sophisticated modeling. In the solar chromosphere, the process of plasma heating has to be strong enough to explain spectral diagnostics formed under optically thick, non-local thermodynamic equilibrium (non-LTE) conditions, such as the resonance lines of Mg II and Ca II, which require detailed three-dimensional (3D) radiative transfer calculations including partial frequency redistribution (see, e.g., de la Cruz Rodríguez and van Noort, 2017; Carlsson et al., 2019). Energy losses are much greater in the chromosphere than in the corona. While in the chromosphere the quiet and active regions require a heating rate that can compensate for the average losses of 4 kW m^{-2} and 20 kW m^{-2}, respectively, the corresponding losses in the solar corona are 0.3 kW m^{-2} and about 10 kW m^{-2} (Withbroe and Noyes, 1977). The chromospheric radiative losses per volume in 1D models are largest just above the temperature minimum, implying that the largest energy deposition rate occurs there, too. The temperature minimum itself is close to its radiative equilibrium value in models like the VAL C model (Holweger and Mueller, 1974; Vernazza et al., 1981; Carlsson and Stein, 1992; Leenaarts et al., 2018).

The problem of chromospheric heating has been recognised since it was shown that the solar chromosphere is hotter than the photosphere. The very first process, prior to phase mixing and resonant absorption, that was proposed to explain this increase in temperature, was the dissipation of acoustic

waves that are generated by turbulent motions in the convection zone (Biermann, 1946; Schwarzschild, 1948). The power and spectrum of these waves was determined from the theory of wave emission by Stein (1967, 1968), which was adapted from the theory of wave emission in the Earth's atmosphere as a quadrupole spectrum by Lighthill (1952). A second mechanism might operate in the lanes between granules, where acoustic monopole emission might provide the waves for chromospheric oscillations that are observed, for example, in Ca II bright points (Lites et al., 1993). Nowadays it is accepted that the heating of the non-magnetic chromosphere is acoustic, at least in the internetwork chromosphere, and that the power of acoustic waves emitted from the convection zone is sufficiently high to account for the radiative emission of the chromosphere. For a detailed review on chromospheric heating by waves, see the comprehensive study by Srivastava et al. (2021). However, much of the motion of particles in the chromosphere (especially the upper chromosphere) are governed by the magnetic field. It is here we expect phase mixing to be an efficient contributor towards the solution of the atmospheric heating problem.

One key aspect that all chromospheric heating models need to take into account is that the temperature of the plasma is not high enough to ensure a fully ionised plasma, therefore this important layer of the solar atmosphere is partially ionised. In these plasmas, the existence of neutral species is known to introduce not only specific effects such as ambipolar diffusion, but also very often impose conditions on the numerical modelling. A multi-fluid description is required when considering waves in a frequency regime that is comparable with the collisional frequencies between particles. A detailed introduction of the consequences of partial ionisation on the numerical modelling of the propagation of waves and the relevant transport mechanisms will be presented in Chapters 2 and 3.

The research presented in this thesis involves merging various important aspects relevant to the chromospheric plasma and the heating due to waves. Understanding the role of neutrals in heating the plasma via wave damping due to phase mixing will play an important role in understanding this unsolved phenomenon.

1.2 Why waves?

Waves pervade the entire universe, touching every aspect of our daily existence. Whether it is in the form of sound waves that resonate through our

ear bones, allowing for transmission of sound vibrations, undulating waves in the ocean that beckons the adventurous thrill seekers to surf, or microwaves that have revolutionised the modern student's culinary skills, waves are not an uncommon occurrence in our every day lives, and nor are they in the solar environment. A wave is a natural manifestation of physical systems when perturbations of an equilibrium state are opposed by various restoring forces that act to bring back the system to equilibrium. Although a physical system can be subject to various equilibria (e.g., dynamical equilibrium, thermal equilibrium, chemical equilibrium), the general view of an equilibrium states the systems are neither in the state of motion nor is its internal energy changing with time. The condition of an equilibrium can be traced back to Newton's first law that states that a body is in equilibrium if it does not experience linear acceleration or angular acceleration. Therefore, unless it is disturbed by an outside force, the body will continue in that condition indefinitely. A particle is considered to be in equilibrium if the sum of all forces acting upon it is zero. A rigid body will be in equilibrium if, in addition to the states listed for the particle above, the vectorial sum of all torques acting on the body equals zero so that its state of rotational motion remains constant. An equilibrium is said to be stable if small, external perturbations produce forces that oppose the displacement and return the body or particle to its equilibrium state.

Restoring forces play an important role when considering the evolution of physical systems. Gravitational forces oppose any displacement of fluids in the direction of gravitational attraction, tension forces in a string tend to work against any plucking, electrostatic forces acting between the core of an atom and its electrons tend to redress the spatial distribution of electron shells when the atom is subject to a collision with another atom; all these simple examples show what an important role restoring forces play. The Sun, a massive ball of plasma, held together by its own gravitational attraction is an environment where all the above restoring forces are acting and their effect can be observationally validated. The solar atmosphere is permeated by a magnetic field that is generated by dynamo effects in the solar tachocline situated at the boundary between the radiative and convective zone in the solar interior and emerges to the solar surface either as unified structures such as sunspots or pores, or diffusely at the edges of granules, and has the ability to fill-up the whole corona. Extreme ultraviolet (EUV) and magnetogram observations show that regions of high emissivity are co-spatial with regions of enhanced magnetism (Wang et al., 2022), therefore the heating must be

somehow connected to the magnetic field (see, e.g., Howard, 1959; Leighton, 1959; Parnell and De Moortel, 2012; Aschwanden and Nhalil, 2023; Judge et al., 2024).

Magnetic fields exhibit behaviour akin to guitar strings (standing waves) or as the result of shaking a hosepipe (propagating waves), in that the reaction to a perturbation causes a wave to propagate. When working within the linear framework, any perturbation affecting the magnetic field lines can be balanced by magnetic tension resulting in a wave type that can appear only in plasmas, the very famous Alfvén wave (Alfvén, 1942). Charged particles (electrons, protons, ions) are attached to these magnetic field lines, providing the inertia necessary for Alfvén waves and other MHD waves. In an ideal case, the magnetic field and the plasma are to be tightly connected and hence the behaviour of these waves is governed by the interplay of plasma with a magnetic field such that these disturbances trace out the magnetic forces. In the absence of plasma, any perturbation in the magnetic field would propagate as an electromagnetic wave travelling at the speed of light.

Alfvén waves, first proposed by Hannes Alfvén, who was later awarded a Nobel Prize in Physics in 1970 for his work in MHD, are a fundamental concept in MHD and provide critical insight into understanding the behaviour of magnetised plasmas. Alfvén waves propagate through a magnetised plasma without perturbing the density of the surrounding plasma, which places conditions on the governing equations. The amplitude of this wave is dependent on the injection of energy supplied by the perturbation, generally the larger the amplitude, the greater the energy. In a non-ideal environment, Alfvén waves can lose their energy to its surroundings due to diffusive or specific viscous effects (see, e.g., De Pontieu et al., 2001; Ruderman and Petrukhin, 2018).

For a considerable period of time, Alfvén waves remained largely undetected due to their inability to perturb density, rendering them "invisible" to EUV instruments. Nevertheless, they have proven crucial in elucidating the heating mechanisms of solar atmospheric plasma. Their incompressibility enables them to traverse the layered solar atmosphere without significant reflection, except at the transition region where partial reflection occurs, allowing them to reach heights inaccessible to other waves.

Alfvén waves are generated as a response to a perturbation of magnetic field lines, typically caused by photospheric motions, magnetic reconnection or mode conversion, and have been observed in the solar atmosphere by Jess et al. (2009*a*), who presented observational evidence of Alfvén waves in the lower

solar atmosphere with sufficient amplitude ($\approx$ 2.6 kms $^{-1}$) and an associated energy flux to heat the solar atmosphere. This constituted a massive step forward for solar physicists. Furthermore, McIntosh et al. (2011) presented observational evidence of coronal Alfvénic waves with sufficient amplitude ($\approx$ 25 km s^{-1}) and, therefore, energy to power the quiet solar corona and drives the fast solar wind. The amplitude of Alfvén waves increase with height due to the stratification of the plasma density, so it is possible to have apparent wave amplification associated with energy dissipation. However, an energy flux sufficient to heat the solar atmosphere is one thing, proving the energy in these waves damps fast enough is another. Alfvén (1947) studied coronal heating by MHD waves, and gave an estimation that the damping of MHD waves transmits of the order of one percent of the total energy radiated by the Sun, however, this value is comparable to the total radiation of the corona. Morton et al. (2014) present evidence of a flattening of the power spectra of kink waves at higher frequencies in the quiescent chromosphere and a positive correlation between frequency and power in the case of a magnetically active region, quite the opposite to the power spectra in the photosphere. They suggest that incompressible wave energy is more efficiently converted to heat at higher frequencies, providing us with further evidence for high frequency waves to be responsible for heating the solar atmosphere.

The plasma heating by waves was indirectly evidenced by several recent studies that further imposed key conditions on how the process could work. Verth et al. (2010) presented observational evidence of resonantly damped propagating kink waves in the solar corona, suggesting heating occurs over very short length scales, while Bate et al. (2022) found observational evidence of a wave reducing in amplitude concurrent with signatures of heating. This is very compelling evidence for plasma heating due to the damping of waves and dissipation of magnetic energy associated with waves.

A comprehensive review of heating mechanisms in solar and stellar coronae was conducted by Erdélyi and Ballai (2007). This study highlighted the intricate interplay between various mechanisms and their dependence on local conditions. Their findings suggest that the effectiveness of these mechanisms varies significantly, making it challenging to isolate a single dominant heating process. They also state that the small scales that heating takes place at (100s of meters), make it currently very difficult to observe mechanisms such as resonant absorption or phase mixing. Another important result that imposes restrictions on the efficiency of wave-based heating mechanisms is the

realisation that in order to have effective heating, one needs high frequency waves. Unfortunately, the observation of these waves is a challenge, since the temporal cadence of the current observational facilities are not adequate for this frequency regime. Nevertheless, there are a number of studies that evidenced high frequency waves as observed by Jafarzadeh et al. (2017), who found high-frequency oscillations in small magnetic elements observed with Sunrise/SuFI.

Numerical models provide us with synthetic observations which play a crucial role in validating theoretical frameworks. Notably, recent MHD simulations conducted by Martínez-Sykora et al. (2011) and Martínez-Sykora et al. (2017) used the Bifrost code (Gudiksen et al., 2011) to successfully capture the process of spicule formation and the identification of Alfvénic waves in numerical simulations. This provides evidence that our current theory of MHD captures key features of the Sun's behaviour, which instills confidence in the capability of large MHD codes to accurately depict phenomena that may not be directly observable. For example, observations allow for wavelengths of approximately 1 Mm to be resolved quite clearly. However, the limitations imposed by current ground and space-based instruments does not mean that much higher frequency waves do not exist.

In the context of phase mixing studies, numerical investigations also use some simplifications that lead to credible results, however, very often these are not totally realistic. One aspect very often neglected is the back reaction of the medium on the efficiency of phase mixing as shown by Cargill et al. (2016). These authors found that wave damping due to phase mixing destroyed an assumed transversal density profile. Since a larger force is required to produce an inhomogeneity in the chromosphere, one could postulate that more heating would be required to destroy this assumed structure. However, the effects of a magnetic field may also work to homogenise the density structure. These constitute possible extensions to the research presented in this thesis proposed in Chapter 7.

The current investigations into phase mixing have overlooked the partially ionised nature of the plasma in the lower solar atmosphere, solely focusing on fully ionised plasmas when discussing the efficiency of damping Alfvén waves. Addressing partial ionisation necessitates a fundamentally new perspective on wave propagation, as the presence of neutrals often alters wave properties (Soler et al., 2015). Moreover, accounting for partial ionisation entails a more intricate system of equations and a novel physical approach involving plasma

physics, atomic physics, and spectroscopy. Considering that waves in partially ionised plasma operate at much higher frequencies than those in a fully ionised plasma, they can significantly impact plasma heating processes. My research consists of extensive investigations aiming to explore the influence of partial ionisation on phase mixing which aims to initiate a movement towards more comprehensive research within this field.

1.2.1 Methodology and approach

Assuming incompressible, linearly polarised transverse waves propagating strictly along magnetic field lines offers a simple mathematical framework. Therefore, Alfvén waves, whose propagation speed is determined by the ratio between the background magnetic field and the square root of the plasma density, are the most natural candidates for studying phase mixing. Of course, phase mixing can occur for any kind of wave, however, the discussion of the properties of these waves in the context of phase mixing is not yet available. Recently, Stangalini et al. (2021) observed torsional oscillations within magnetic pores and Chae et al. (2022) observed Alfvénic waves in the chromosphere around a small sunspot presenting further evidence of the ubiquity of Alfvén waves in the inhomogenous lower solar atmosphere. These observations, in conjunction with the investigations previously mentioned, highlight the importance of further study of phase mixed Alfvén waves in the lower solar atmosphere.

The analysis presented in this thesis uses the framework of both a single-fluid and two-fluid plasma. In the case of a single-fluid framework, the partial ionisation effects appear only through specific transport mechanisms. We consider linearly polarised Alfvén waves in a non-stratified plasma, with a plasma inhomogeneity in the direction transverse to the direction of wave propagation and its polarisation. When considering a two-fluid approach to wave propagation, we isolate the ionised plasma from the neutral gas via two coupled equations of motion. Partial ionisation also appears through the transport mechanisms, whereby each fluid has its own characteristic viscosities. The present study can be considered as a proof of concept analysis to emphasise the importance of neutrals on the damping lengths of phase-mixed Alfvén waves and the associated heating rates.

Analytically obtained governing equations will be solved using a number of numerical techniques such as the finite difference approximations that address spatial derivatives, a fourth-order Runge-Kutta time step to progress simulations forward in time, and sparse matrices to represent the coefficients

of the finite difference approximations, greatly enhancing the efficiency of the calculations performed. Full details of the numerical approach employed by the present thesis can be found in Chapter 3.

1.3 Partially ionised solar plasmas

Plasma is present throughout the entire Universe, existing at various scales. In 1986 Hannes Alfvén introduced the term 'plasma universe' to stress the important role played by plasma across the universe. Plasma, a state of matter distinct from solids, liquids, and gases, is often referred to as the fourth state of matter, consisting of charged particles showing collective dynamics. Plasma is formed by applying considerable amounts of thermal energy to atoms, large enough to overcome the electrostatic force between protons and electrons, a force that ensures the existence of neutral atoms. For decades, scientific investigations operated under the assumption that the plasma in the solar atmosphere exists in a fully ionised state. This assumption allowed for mathematical simplifications, such as ignoring diffusive effects (or at least terms corresponding to products of diffusive quantities), leading to a more manageable set of MHD equations. However, recent advancements in observational technology and numerical modelling has shifted the focus to studying solar structures such as prominences, spicules, and the lower layers of the Sun's atmosphere (photosphere and chromosphere), which consist of partially ionised plasmas. In these regions, the temperature is high enough to cause ionisation, but a significant amount of neutral gas remains, as indicated by the presence of H-α emission. This new focus aims to comprehend the nuanced interplay between ionised and neutral components coexisting in solar structures and aims to refine our understanding of their dynamic behavior.

Reliable atmospheric models predict that the electron-neutral number density ratio of the plasma in the lower solar atmosphere covers several orders of magnitude. For example, the AL C7 atmospheric model (Avrett and Loeser, 2008) of the quiet Sun predicts the electron-neutral ratio to range between 9×10^{-5} and $\sim 10^{6}$. In solar prominences Patsourakos and Vial (2002) predicted that the ratio between the electron density and neutral hydrogen density ranges between 0.1 and 10. For analytical progress, often it is customary to consider strongly or weakly ionised limits that simplify the mathematics. In these cases the ratio of neutral to charged particle number densities (or its inverse) is considered to be a small parameter about which governing equations

are expanded into series with respect to these small parameters (see, e.g., Alharbi et al., 2021). Naturally, these limits are idealisations and relevant to an average quiet Sun scenario. If one wants to bring modelling closer to reality, a whole spectrum of ionisation degrees must be considered and this would imply a comprehensive numerical investigation and parameter study, see Chapter 4 for more details.

The last decade has seen an increased number of studies on the properties of waves in partially ionised plasma. The modeling framework of a partially ionised plasma depends very much on the frequency regime in which a certain physical mechanism is described. When the frequency of waves is much smaller than the collisional frequency of particles, a single-fluid description of MHD is sufficient. In this framework, partial ionisation appears through the generalised Ohm's law and it describes diffusive damping (often called ambipolar diffusion) of currents perpendicular to the ambient magnetic field as well as the viscosity tensor in the equation of motion. The presence of neutrals enhances terms associated with damping in the governing equations since the neutrals increase dissipative coefficients such as Ohmic diffusion and viscosity.

Ambipolar diffusion occurs within a partially ionised plasma when the neutrals are not fully coupled to the charged component. While the charged fluid is subject to the Lorentz force, the decoupled neutral particles undergo a Brownian motion, while still being affected by the close-range collisions with ions. These collisions result in frictional effects between the two components, providing a mechanism for magnetic and mechanical energy to be dissipated, and hence creating a source of localised atmospheric heating (see, e.g., Khomenko et al., 2018; Forteza et al., 2007; Shelyag et al., 2012). We should note here that in a fully ionised plasma we can also have ambipolar diffusion, however, in this case, the extra diffusive effects are due to different mean velocities of positive charges and negative charges. Due to this difference, an electric field (and an electric current) is created that pulls along the heavier species with the aim of restoring the plasma neutrality and prevent any further charge separation. As a result of the "lagging" particles, the motion of those particles that move ahead is impaired. The trailing particles also have a tendency to be pulled to the front but to a lesser extent than the tendency for leading particles to be held back. If the diffusion coefficient for the two species is very different, the total diffusion coefficient will only be half as large as the largest individual coefficient. In this case, the ambipolar diffusion refers to the combined diffusion of oppositely charged particles. For details see, e.g., Scudder (1996, 1997)

The role of ambipolar diffusion in the partially ionised solar atmospheric plasma has received recent special attention due to the specific way it operates and due to its magnitude compared to other dissipative coefficients. Sarp Yalim et al. (2020) investigated the heating effects of the Cowling resistivity in the weakly ionised limit and found the Joule heating profiles corresponding to Cowling resistivity to be as much as six orders of magnitude higher than heating rates associated with Coulomb resistivity. Note that resistivity and diffusivity are closely linked processes both involved in wave damping and heation, but posses very different units. Melis et al. (2023) found the wave heating rate achieved its maximum in the central part of the thread, where the plasma is partially ionised and ambipolar diffusion is responsible for wave dissipation. In the outermost coronal part, wave heating was negligible because of the irrelevance of Ohm's diffusion for fully ionised coronal conditions. This highlights the significance of partial ionisation for effective plasma heating and suggests that the solution to the coronal heating problem may lie in the partially ionised lower solar atmosphere. Khomenko and Collados (2012) investigated the heating of the solar chromosphere under the influence of a non-force-free magnetic field. They discovered a direct relationship between the heating rate and the intensity of the magnetic field, which correlates closely with the ambipolar diffusion coefficient's value. Recent studies by Khomenko et al. (2018) and Popescu Braileanu and Keppens (2021) further explored the role of ambipolar diffusion, revealing its substantial enhancement of wave damping in regions of strong magnetic fields within the photosphere and chromosphere. Careful consideration must be taken when calculating the ambipolar diffusion coefficient, as demonstrated by Nóbrega-Siverio et al. (2020), who revealed the importance of heavy proton donors such as sodium, silicon and potassium. Neutrals, as well as having a strong influence on the dissipation rates of MHD waves, also have the effect of stabilising instabilities (see, e.g., Mather et al., 2018; Ballai et al., 2015, 2017). Khomenko et al. (2021) investigated the influence of ambipolar diffusion on vorticity in three-dimensional simulations of magneto-convection, and found that the ambipolar diffusion produces a strong reduction of vorticity in the upper chromospheric layers and that it dissipates the vortical perturbations converting them into thermal energy, again similar to having a stabilising effect. These investigations collectively imply a strong association between the presence of neutrals and the efficient damping of waves, potentially leading to effective heating within the partially ionised solar atmosphere. The nonlinear propagation of waves in a three-dimensional stratified solar flux tube in the

presence of ambipolar diffusion was considered by Shelyag et al. (2016) and showed that up to 80% of the Poynting flux associated with these waves can be dissipated and converted into heat, providing an order of magnitude larger energy supply to the chromosphere compared to the dissipation of stationary currents modelled by Khomenko and Collados (2012). Using a 2.5 D radiative MHD code, Martinez-Sykora et al. (2015) showed that the ambipolar diffusion effectively dissipates magnetic energy and increases the temperature in the chromosphere.

When the frequency of waves is comparable to the collisional frequency of ions and neutrals, a single-fluid MHD description is no longer sufficient and we must employ a multi-fluid framework of the problem, whereby one fluid consisting of ions and electrons which are strongly bound together interacts with a neutral gas through collisions. Ambipolar diffusion is modelled very differently here since the two fluids have their own equation of motion, ambipolar diffusion does not appear directly in the governing equations but as a consequence of the two fluids in relative motion. Zaqarashvili et al. (2011) and Soler et al. (2013) discussed the solutions of the dispersion relation for Alfvén waves in a two-fluid plasma and found that high-frequency waves (with frequencies higher than the ion-neutral collisional frequency) have vastly different damping rates than the single-fluid model's approach. These studies showed that the efficiency of damping increases for smaller wavelengths.

In order to complete the scientific aim of the present thesis, it is crucial to accurately compute the values of dissipative coefficients within the partially ionised solar atmosphere. While comprehensive formulae are provided in Chapter 2, it is worth noting their dependency on various plasma parameters, including the temperature and number density of ions, electrons, and neutrals. To estimate these values accurately, we rely on the AL C7 atmospheric model (Avrett and Loeser, 2008) which operates under the assumption of non-local thermal equilibrium (NLTE). This assumption implies an imbalance in energy exchange processes locally, where energy gained through collisions is not balanced by energy lost through radiation. Lastly, the AL C7 model (Avrett and Loeser, 2008), employed throughout this thesis, represents the most contemporary atmospheric model available, over those such as the VAL (Vernazza et al., 1981) or FAL (Fontenla et al., 1993) models. This model is derived from observations made by high-resolution spectroscopic instruments (e.g., SOHO/-SUMER and HRTS instruments), marking a significant stride forward in our comprehension of partially ionised plasmas.

While Braginskii (1965) significantly advanced our understanding by exploring transport processes in both partially ionised and fully ionised plasmas, subsequent developments have led to the availability of updated formulae. These newer definitions offer refined predictions, shaping our contemporary approach to research in this area. Vranjes and Krstic (2013) provide detailed height-dependent collisional cross sections and collisional frequencies, Vranjes (2014) provide comprehensive formulae for viscosity in a partially ionised plasma, demonstrating - for example - that the neutral shear viscosity in the photosphere and chromosphere is approximately 5 orders of magnitude larger than the ion viscosity.

1.4 Phase mixing

The proposition of phase mixing as a mechanism to heat the solar corona was initially introduced by Heyvaerts and Priest (1983). However, the theoretical foundation of phase mixing traces back at least as far as 1931, when Maria Goeppert Mayer (Göppert-Mayer, 2009) explored this mechanism in the field of nonlinear optics, a branch of optics describing the behavior of light in nonlinear media. Due to the nature of Alfvén waves and the relative simplicity of their associated governing equations, phase mixing was predominantly investigated in connection to these waves, over any other kind.

The requirement for the phase mixing of Alfvén waves to develop in the solar atmosphere aligns with the same inhomogeneity condition as investigated by Göppert-Mayer (2009). Phase mixing occurs when Alfvén waves, propagating on magnetic surfaces, oscillate out of phase with waves on neighbouring surfaces, resulting in the development of significant cross-field gradients. This out-of-phase oscillatory behavior arises due to the presence of either an inhomogeneous background density or magnetic field profile, or both. Structures with such properties are found in abundance in the solar atmosphere in magnetic bright points, spicules, sunspots, pores, filaments and coronal holes.

Due to magnetic field lines experiencing magnetic tension, waves are strongly influenced by the behavior of other waves in their vicinity, the extent of the distortion of each wave is dictated by the variation in the frequencies of nearby waves as well as other plasma properties such as density and magnetic field strength. Since the plasmas in which Alfvén waves in the lower solar atmosphere propagate are inhomogeneous, phase mixing plays a fundamental role

in the way in which an Alfvén wave damps and subsequently dissipates its energy to heat the surrounding environment.

Observational evidence presented in the studies by Jess et al. (2009*b*) and Jafarzadeh et al. (2017) highlighted the existence of Alfvén waves in the lower solar atmosphere at the base of magnetic bright points, where the surrounding plasma is partially ionised. One important feature of magnetic bright points, similar to spicules (He et al., 2009), is there is a clear transversal inhomogeneity in plasma parameters that influence the Alfvén speed, leading to phase mixing in the presence of partially ionised plasma. Therefore, investigating phase mixed Alfvén waves in partially ionised plasma is crucial for a comprehensive understanding of the associated wave-based heating mechanisms surrounding these plasma structures.

Heyvaerts and Priest (1983) investigated phase mixed Alfvén waves while working in the linear regime, assuming an infinite sinusoidal wave driver and found that the damping length, calculated to be the distance over which the amplitude decays be e times, was proportional to the frequency of the wave, the Ohmic diffusion, shear viscosity and local gradient in the Alfvén speed (more on these dissipative mechanisms in Chapter 2). Increasing any of the dissipative terms subsequently resulted in the damping length reducing. The authors found that short period Alfvén waves contribute more significantly to coronal heating. It is important to note the incomplete account of the transversal gradient in obtaining their solution, by assuming the velocity perturbation to be a *rather regular function of* x. These discrepancies were later investigated by Ireland and Priest (1997), who found increased diffusion of sharp features when proper numerical treatment (of the second-order spatial derivatives) was considered. Wave damping theory proposes that the faster waves damp, the more dramatic the localised heating. Although it is not well understood what proportion of the waves energy is transferred into heating its surrounding environment, it is thought that a mechanism that reduces the damping length of a wave naturally suggests more pronounced heating.

Hood et al. (1997) also investigated the heating of coronal loops by phase mixing of a continuous sinusoidal driver and found that phase mixing can maintain a hot coronal loop for a large Lundquist number given by $S = Lv_{A0}/\eta$, where L is the typical length scale of the system, v_{A0} is the typical Alfvén velocity and η is the Ohmic diffusion coefficient. The Lundquist number is effectively the magnetic Reynolds number (a dimensionless quantity used in MHD to characterise the relative importance of the magnetic effects to fluid

flow) where the typical velocity scale of the system is the Alfvén speed. They found maximal Ohmic heating occurred after a few periods of the wave had propagated, which corresponds to the development of phase mixing.

While assuming an infinite sinusoidal wave driver makes the mathematics more manageable analytically, in reality, we more often observe periodic wave-like structures consisting of only one to a few wave periods (Bate et al., 2022), hence Hood et al. (2002) investigated the damping of propagating phase mixed Alfvén pulses. These authors used cosine profiles to construct various pulses with an effective wavelength of 400 km for a half period (pulse) and a whole period (bipolar pulse). Their numerical investigation revealed that the decay of these pulses followed an algebraic trend, in contrast to the exponential decay observed by Heyvaerts and Priest (1983). This investigation gave the first true insight into the effect phase mixing has on the profile of a pulse. However, the Ohmic diffusion coefficient assumed was orders of magnitude larger than classical formula predict.

The use of enhanced dissipative coefficients is frequently encountered in phase mixing literature. Either authors find themselves invoking dissipative coefficients large enough to demonstrate significant heating or they conclude that unrealistic assumptions have to be made for certain plasma and wave parameters in the model such as the period of the waves. For example, Mocanu et al. (2008) found that phase mixed Alfvén waves are far more likely to energise the solar wind than heating coronal holes, essentially stating that Alfvén waves will not be damped in the corona. Ruderman and Petrukhin (2018) increased the value of the classically defined shear viscosity by 6 orders of magnitude to obtain appreciable damping. This increase was made by invoking the assumption that the plasma is turbulent. Heyvaerts and Priest (1983) state that *a major enhancement in the efficiency of the process* [of phase mixing] *is found when the waves are for some reason trapped and phase-mix in time without propagating away.* Such standing waves are highly likely to be found in coronal loops and are subject to Kelvin-Helmholtz instability (KHI) (see, e.g., Karpen et al., 1994; Ofman et al., 1994; Karampelas et al., 2017; Howson et al., 2017*b*; Guo et al., 2019; Hillier et al., 2024), a hydrodynamic instability that occurs at the interface between two layers of fluid in relative motion, characterised by the formation of rolling vortices, which could result in strong velocity gradients due to consistent wave reflection at loop footpoints. Browning and Priest (1984) found that the KHI plays an active role in

expediting the transition of shear Alfvén waves to a turbulent state. This transition results in the formation of smaller length scales in both the velocity and magnetic fields, significantly enhancing wave dissipation. The development of transverse wave-induced Kelvin Helmholtz vortices has been confirmed by recent numerical investigations, (see, e.g., Antolin et al., 2014; Magyar and Van Doorsselaere, 2016; Howson et al., 2017*a*,*c*; Hillier et al., 2019), which leads to the enhancement of viscosity and the Ohmic diffusion coefficient. More recently, Díaz-Suárez and Soler (2024) investigated the role of phase mixing in triggering the KHI, expediting the transition of the plasma in a prominence thread to a turbulent state. While this mechanism was found to not be sufficient to heat such structures, both the phase mixing and turbulent stages could be seen in high-resolution H-α observations. Similar to Ruderman and Petrukhin (2018), Pagano and De Moortel (2017) found that in the presence of enhanced values of the Ohmic diffusion coefficient and very strong footpoint drivers, sufficient heating to balance radiative losses can be produced only locally in the area of heating, and for these reasons deemed it *unlikely that phase mixing can contribute on a global scale to the heating of the solar corona.* While working in the linear regime, Prokopyszyn and Hood (2019) found that such unrealistically large dissipative coefficients were required due to numerical constraints, and even so predicted damping rates approximately three orders of magnitude too small to heat the corona. Cargill et al. (2016) investigated the evolution of an assumed coronal density structure and found that the assumed density profile is only initially valid as the heating produced by the damping and dissipation of Alfvén waves caused the density profile to smooth out, which would subsequently lead to lower levels of phase mixing as time evolves. However, during numerical simulations of coronal loops, Van Damme et al. (2020) found that chromospheric material evaporated very slowly and while this evaporation causes a mass increase in the loop, the impact on the density gradient was insignificant, hence the assumption of an assumed density profile holds much stronger in the chromosphere. It must be noted that Van Damme et al. (2020) assumed classical values of the various transport mechanisms and concluded that the phase mixing of Alfvén waves resulted in relatively mild heating in the shell regions of coronal loops. One might assume that if the enhanced dissipative coefficients were employed, this result may not hold. Khomenko et al. (2014) provides a fluid description of multi-component solar partially ionised plasma, and showcases the important effect of ambipolar diffusion on the electric current especially at the borders

of intergranular lanes with strong gradients in plasma density and background magnetic field, where phase mixing has the potential to be a dominant damping mechanism. Ebadi and Hosseinpour (2013) investigated phase-mixed standing Alfvén waves in spicules in the presence of shear flows and found that waves dissipated within a few periods, confirming the prediction made by Heyvaerts and Priest (1983) who stated that standing or trapped waves present better candidates for coronal heating.

Of course, we do not dispute that turbulence is present in both the partially ionised lower atmosphere (Oppenheim et al., 2020) as well as the corona (Delaboudinière et al., 1995). While turbulence is not a topic included in this thesis, we clearly have to draw attention to it, due to the implications assumed by previous authors working in the field of phase mixing. Typically, when studying Alfvén waves, turbulence can occur when Alfvén waves are partially reflected due to the density gradient at the transition region, leading to counter propagating waves. These counter propagating Alfvén waves then interact non-linearly resulting in a turbulent cascade of energy to very small spatial scales.

This effect has been studied observationally using the Coronal Multi-Channel Polarimeter (CoMP) by Morton et al. (2015) who studied the Doppler velocity fluctuations confirming the ubiquity of Alfvénic waves in the corona. Another instability present in the solar atmosphere is the Rayleigh Taylor instability (RTI), which occurs when a denser fluid is accelerated into a less dense fluid. This situation is inherently unstable, that leads to the formation of complex structures such as spicules and bubbles. RTI drives upflows and impulsive downflows in Quiescent prominences, leading to turbulent motions. These turbulent prominence motions have been investigated by Hillier et al. (2017) who used observational data from Hinode Solar Optical Telescope (SOT) to show that while the heat from the turbulent energy dissipation was inefficient at heating prominence plasma, the mass diffusion achieved through turbulence driven reconnection was of the order of the expected value of ambipolar diffusion. Numerical investigations have confirmed that MHD theory predicts these observations (see, e.g., van Ballegooijen et al., 2011; Hillier et al., 2011; van der Holst et al., 2014*b*). More recently, Magyar et al. (2017) interpreted a turbulent-like behaviour of unidirectionally propagating phase-mixed MHD waves. Contrasting to the typical view that the generation of turbulence is restricted to counter-propagating Alfvén waves in compressible MHD. The

presence of turbulent motions will increase the efficacy of the various dissipative mechanisms present in the solar atmosphere, however, this is beyond the scope of this present thesis. With that in mind, we do not consider the effects of turbulence in our simulations.

1.5 The aim of the thesis

The present thesis aims to study the effects of partial ionisation and plasma inhomogeneities on Alfvén wave damping, and consequently, the heating associated with this damping. This is achieved by deriving and then solving the governing equation which describes the evolution of propagating Alfvén waves in a partially ionised plasma describing the conditions in the solar photosphere and chromosphere (see Chapter 2 for the derivation of the governing equations employed in the single-fluid and two-fluid approaches). In Chapter 3, we provide details of the numerical model constructed to solve the various governing equations derived in Chapter 2. We solve the governing equation modelling a single-fluid plasma where the effects of partial ionisation are cast in the various dissipative coefficients as well as the inclusion of Cowling diffusion and present the results in Chapter 4. In Chapter 5, we investigate the effects of various wave drivers on the damping of phase mixed Alfvén waves, before finally tackling the two-fluid approach to the problem of phase mixed Alfvén waves, allowing for the study of much higher frequency waves than those permitted in a single-fluid study. In a two-fluid plasma, the effects of partial ionisation are evident in the relative density ratio between ions and neutrals, the ion and neutral shear viscosity coefficients as well as the collisional frequency term, all of which appear in the governing equation. Results of the two-fluid approach are presented in Chapter 6. We conclude our results in Chapter 7 and propose future research directions.

1.6 Significance of research

While solving the chromospheric and/or the coronal heating problem may not have immediate direct consequences back on Earth, future advancements in understanding the mechanisms that heat plasma could potentially allow for efficient energy production on Earth. Also, furthering our fundamental astrophysical knowledge will enhance our understanding of the behavior of plasma in extreme conditions and help us potentially develop the theory of MHD further. In addition, any work done to better understand the Sun is

bound to benefit space weather predictions which is of great importance in assuring the safety of astronauts and also the vast array of satellites ensuring the smooth running of day-to-day life we have all grown so accustomed to back on Earth.

CHAPTER 2

Partially ionised solar plasmas and their quantitative description

2.1 Introduction

Both space and laboratory plasmas are very often only partially ionised. The ionisation degree, defined by the relative population of ions and neutrals, measures the extent of ionisation in a plasma and is usually a spatially dependant function. For example, the Earth's ionospheric plasma is a partially ionised plasma in which the ion density changes over three orders of magnitude between the D and F layers. At the base of the photosphere (lowest part of the solar atmosphere), the ratio of the neutral density to the ion density is $\sim 10^3$; then increases with height to reach a maximum value of $\sim 10^4$ at the top of the photosphere ($\sim$ 500 km) and then decreases to ~ 1 at an altitude of $\sim$ 2000 km, i.e., in the chromosphere (Priest, 2014), before asymptotically approaching zero in the corona, where the plasma is often assumed to be fully ionised.

In a partially ionised plasma, constituent particles can interact through short-range (head-on collisions between neutral particles and between neutrals and other charged species) and long-range (controlled by electrostatic forces between the charged particles) collisions. The processes taking place at the collisions can be categorised into two different regimes: elastic and inelastic processes. The collisions are called elastic if the internal energies and identities of the colliding particles are unchanged after the collision. The particle direction may be changed after the collision, but the total initial momentum and kinetic energy of the particles are both conserved. In the case of inelastic collisions the chemical composition of the plasma is not conserved, particles are created and lost during the collisional processes (e.g., ionisation and recombination). Collisions are the defining characteristics of a dense partially ionised plasma, such as the plasma found in the lower solar atmosphere. Having said

that, it is obvious that a partially ionised plasma can never be classified as an ideal plasma.

The present thesis deals with elastic collisions only, therefore the nature and mass of the system are conserved. Strictly speaking, a partially ionised plasma is an amalgam of six types of particles such as photons, electrons, positive and negative ions, neutral particles in the ground state and neutral particles in an excited state. Photons play a very important role in the process of ionisation and recombination, however, they will not be considered. Throughout the present thesis we will assume a uni-thermal plasma consisting only of Hydrogen, meaning that the only ion that can appear in this system is the positively charged proton. In a recent investigation, Alharbi et al. (2021) has shown that in the presence of collisions, the solar partially ionised plasma reaches a thermal equilibrium in a few collisional times, so it is natural to consider that $T_e = T_i = T_n$. That is, the temperature of any highly energetic particles quickly homogenises within a few collisions, a small fraction of a second when considering collisional frequencies typical of the lower solar atmosphere. For simplicity, we will not consider excited hydrogen atoms, and all neutral particles will be considered to be in the ground state.

The quantitative description of partially ionised plasmas often requires a multi-fluid approach (as opposed to the description of the plasma as a collection of particles in kinetic physics), where all particles of a given type (e.g., neutral Hydrogen) can be considered as a separate fluid. Given the fluid approach of the particle mixture, it is natural to expect that the dynamics of each species will be governed by the mass, the momentum, and the energy conservation laws under the action of various forces. A multi-fluid model enables us to study the consequences of different plasma components often having, at the same spatial point, different velocities, temperatures and pressures.

2.2 General considerations

The partially ionised plasma - considered as a fluid- is going to be characterised by the thermodynamics and dynamical parameters T_α, p_α, n_α and $\mathbf{v}_\alpha$ representing the temperature, pressure, number density and velocity of the species α (electrons $\alpha = e$; ions $\alpha = i$; neutrals $\alpha = n$), respectively. In addition, the mass density of particle type α is defined as $\rho_\alpha = n_\alpha m_\alpha$, with m_α being the mass of the particle. We should note that since we are dealing with a hydrogen plasma, $m_i \approx m_n$, $m_e/m_i \approx 1/1837$ and $n_e = n_i$. These thermodynamical

quantities are connected via the equation of state of the form $p_\alpha = n_\alpha k_B T_\alpha$, where k_B is the Boltzmann constant.

The total density and pressure of the system can be defined as

$$\rho = \sum_\alpha \rho_\alpha \approx \rho_i + \rho_n, \quad p = \sum_\alpha p_\alpha \approx 2p_i + p_n. \tag{2.1}$$

The velocity of the centre of mass is defined as the sum of velocities weighted by the importance of various particles in the system, i.e.

$$\mathbf{v} = \frac{1}{\rho} \sum_\alpha \rho_\alpha \mathbf{v}_\alpha \approx \xi_i \mathbf{v}_i + \xi_n \mathbf{v}_n \tag{2.2}$$

where we took into account $\rho_e |\mathbf{v}_e| \ll (\rho_i |\mathbf{v}_i|, \rho_n |\mathbf{v}_n|)$ (in virtue of the mass difference).

The quantities ξ_i and ξ_n denote the relative densities of ions and neutrals compared to the total density of the plasma and they are defined as

$$\xi_i = \frac{\rho_i}{\rho} \approx \frac{n_i}{n_i + n_n}, \; \xi_n = \frac{\rho_n}{\rho} \approx \frac{n_n}{n_i + n_n}, \tag{2.3}$$

so that $\xi_i + \xi_n = 1$. With these quantities, we can define the ionisation degree of the plasma as

$$\mu = \frac{1}{1 + \xi_i}, \tag{2.4}$$

which means that $\xi_i = (1/\mu) - 1$ and $\xi_n = 2 - 1/\mu$. The quantity μ will play an important role in our investigation when we discuss the efficiency of the phase mixing in terms of the ionisation degree of the plasma. The parameter μ varies between the values of $1/2$ for a fully ionised plasma and 1 for a fully neutral fluid.

The degree of ionisation of the solar atmospheric plasma can be derived from standard solar atmospheric models. Here we employ the AL C7 model (see Avrett and Loeser 2008, for more details) that provides values of neutral hydrogen and electron number densities with height and temperature. The variation of the ionisation degree, together with the variation of temperature with height, is shown in Figure 2.1. This dependence of the ionisation degree with height clearly shows that the photosphere is mostly neutral, the chromosphere has a more balanced population of ions and neutrals, while beyond the transition region, in the corona, the plasma is practically fully ionised.

Understanding the variation in the ionisation degree and how it relates to the magnitudes of the various dissipative coefficients present in a partially ionised plasma is essential when studying the efficiency of phase-mixing on damping Alfvén waves. This is discussed later in this chapter.

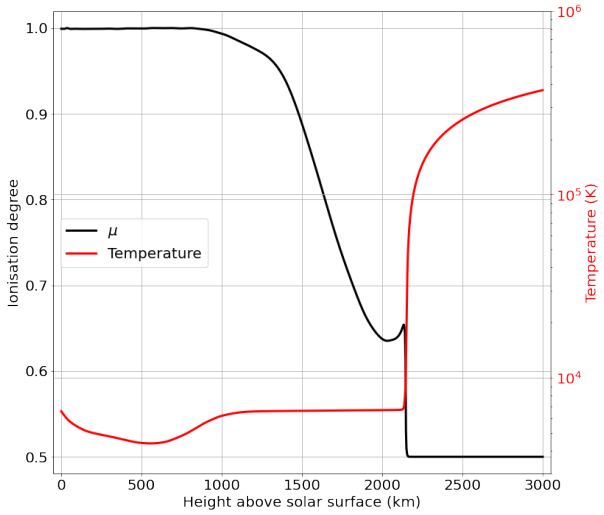

Figure 2.1: The ionisation degree and plasma temperature are plotted with height according to the AL C7 model (Avrett and Loeser, 2008) for heights above the solar surface up to 3000 km.

2.3 Governing equations in partially ionised plasmas

By leveraging our Sun as a plasma laboratory, we can apply insights gained from studying the behavior of partially ionised plasmas, informed by the MHD equations, to investigate how plasmas behave in various environments such as the chromosphere, photosphere, corona, solar wind and astrophysical phenomena far beyond our solar system. Understanding these equations can not only shed light on the inner workings of our Sun but also has the potential to elucidate the dynamics of accretion disks around black holes and the processes inherent in star and galaxy formation. The MHD equations provide insights into the complex behaviour of waves, and understanding these processes is of the utmost importance for numerical modelers aiming to understand atmospheric heating.

When presenting and discussing the MHD equations, we should keep in mind that the set of equations needed to describe the dynamics of plasma depends on the range of frequencies of interest. Based on the strength of the electrostatic coupling between ions and electrons, very often it is customary to consider that the charged particles form a single fluid that interacts through close-range collisions with neutrals. This framework is referred to as the two-fluid approach and is applicable for dynamical changes whose frequencies are close to the collisional frequency of neutrals with the charged particles. Given

the mass difference between electrons and neutrals, the collisions between them do not involve a large momentum exchange, therefore, these collisions are usually neglected when compared with the collisions of ions and neutrals. When the frequencies of interest are much smaller than the collisional frequency between particles, one is able to describe the dynamics of the plasma with a single-fluid description, where physical parameters can be seen as averages of the values of these parameters for each species. The single and two-fluid approaches will be used throughout the present thesis and the following sections will be dedicated to the introduction and discussion of the equations that govern the spatial and temporal variations of the plasma parameters.

2.3.1 Mass conservation equation

As we stated earlier, various fluid equations (mass, momentum, energy conservation) stay at the core of our governing equations. In the presence of elastic collisions, the mass conservation law of each species suggests that for each species we have

$$\frac{\partial \rho_\alpha}{\partial t} + \nabla(\rho_\alpha \mathbf{v}_\alpha) = 0. \tag{2.5}$$

In a two-fluid plasma, the addition of the densities of charged particles as in Equation (2.1), and defining the velocity of the centre of mass as in Equation (2.2), results in the two mass conservation laws

$$\frac{\partial \rho_c}{\partial t} + \nabla(\rho_c \mathbf{v}_c) = 0 \tag{2.6}$$

and

$$\frac{\partial \rho_n}{\partial t} + \nabla(\rho_n \mathbf{v}_n) = 0, \tag{2.7}$$

where the indices c and n stand for the charged and neutral fluids, respectively. Due to the relative mass difference of ions to electrons, the subscript c, in Equation (2.6), can be interchanged with subscript i without loss of generality. Summing all densities and velocities as defined by Equations (2.1)–(2.2) results in the mass conservation law of the plasma in a single-fluid approximation given by

$$\frac{\partial \rho}{\partial t} + \nabla(\rho \mathbf{v}) = 0. \tag{2.8}$$

In this approach, the characteristics of each constituent species are neglected and the ensemble of particles is treated as one single fluid. The law of conservation of mass states that if a physical system is closed to all external transfers of mass, this quantity must remain constant over time, as the system's mass cannot change.

2.3.2 Momentum conservation equation

The momentum equations, often referred to as the Navier-Stokes equations, describe the balance of forces acting on a magnetised plasma in the presence of an electromagnetic field, taking into consideration the effects of pressure, plasma velocity and the magnetic field.

For simplicity we assume that the characteristic length scales involved in the problems we are going to discuss later are shorter than the gravitational scale-height, meaning that the effect of the gravitational force will be neglected. Similarly, we are going to neglect other non-inertial forces, such as the Coriolis force. The forces that can act upon the system depend on the type of particle we are dealing with. While charged particles are affected by electromagnetic forces, the forces that act on neutral particles are similar to the standard forces that can influence the dynamics of a fluid. Therefore, the momentum conservation laws have to be written separately for charged and neutral particles. In the most general form, the momentum conservation equation takes the form (Khomenko et al., 2014)

$$m_\alpha n_\alpha \frac{d_\alpha \mathbf{v}_\alpha}{dt} = -\nabla \hat{\mathbf{p}}_\alpha + n_\alpha Z_\alpha e \left(\mathbf{E} + \mathbf{v}_\alpha \times \mathbf{B}\right) + \sum_{\alpha'} \mathbf{R}_{\alpha'\alpha} \tag{2.9}$$

where $d_\alpha/dt = \partial/\partial t + \mathbf{v}_\alpha \cdot \nabla$ is the convective derivative, $\hat{\mathbf{p}}_\alpha$ is the pressure tensor, Z_α is the electric charge of particles ($Z_e = -1$, $Z_i = 1$, $Z_n = 0$), e is the elementary charge, $\mathbf{E}$ is the electric field and $\mathbf{B}$ is the magnetic field. The term on the left-hand side of this equation is often labelled as the inertial term, the terms on the right-hand side are the pressure force, the electric and magnetic force (Lorentz force) acting upon charged particles, while the very last term is the net frictional drag force due to collisions of species α' with species α (clearly, $R_{\alpha\alpha} = 0$ as a species cannot exert drag on itself). The frictional terms take the form

$$\mathbf{R}_{\alpha'\alpha} = \nu_{\alpha'\alpha} m_{\alpha'} n_{\alpha'} (\mathbf{v}_{\alpha'} - \mathbf{v}_\alpha), \tag{2.10}$$

so that in the frame of reference of particle α, the above expression denotes the drag force on particles α', which have momentum $m_{\alpha'} n_{\alpha'} \mathbf{v}_{\alpha'}$ measured in this frame of reference and is calculated by multiplying by the rate ($\nu_{\alpha\alpha'}$) at which this momentum is lost by collisions. Since the collisions are elastic, $\mathbf{R}_{\alpha\alpha'} + \mathbf{R}_{\alpha'\alpha} = 0$. This friction acts such that the faster species will be slowed down by the slower species and there will be no friction between species if they have the same velocity.

Throughout the present thesis, we are going to consider only elastic collisions. The expressions for the collisional frequencies between various particles are given by (see, e.g., Braginskii, 1965; Vranjes, 2014)

$$\nu_{in} = 4n_n\sigma_{in}\left(\frac{k_BT}{\pi m_i}\right)^{\frac{1}{2}}, \tag{2.11}$$

$$\nu_{en} = n_n\sigma_{en}\left(\frac{8k_BT}{\pi m_e}\right)^{\frac{1}{2}}, \tag{2.12}$$

$$\nu_{nn} = 4n_n\sigma_{nn}\left(\frac{k_BT}{\pi m_n}\right)^{1/2} \tag{2.13}$$

$$\nu_{ei} = \frac{n_e e^4\Lambda}{3m_e^2\epsilon_0^2}\left(\frac{m_e}{2\pi k_BT}\right)^{3/2} = \nu_{ee} = \nu_{ii}\left(\frac{m_i}{m_e}\right)^{1/2}, \tag{2.14}$$

where the number densities of particle α are given by n_α in m^{-3} and the temperature is given in Kelvin (K). We have also used $m_i \approx m_n$ and assume that the drift velocity is small compared to the thermal velocity. In the case where this is not satisfied, the feedback of the drift velocity on the collision frequency can result in a decrease in the diffusion of the magnetic field compared with the standard ambipolar diffusion approximation, see Hillier (2024) for more details. The quantities $\sigma_{\alpha'\alpha}$ denotes the collisional cross-section of particle α' and α. The collisional cross-sections that appear in the above relations are (weakly) height-dependent due to the fact that these values depend on the energy of colliding particles, i.e., their temperature (see, e.g., Vranjes and Krstic, 2013). However, for the sake of the present analysis, we are going to consider them as constant and here these take the values $\sigma_{in} = 3.5 \times 10^{-19}$ m^2, $\sigma_{en} = 10^{-19}$ m^2, $\sigma_{nn} = 2.6 \times 10^{-19}$ m^2. In the above relations, ϵ_0 is the electric permittivity and

$$\Lambda = \ln\left[\frac{8.48\pi}{n_i^{1/2}}\left(\frac{\epsilon_0 k_BT}{e^2}\right)^{3/2}\right] \tag{2.15}$$

is the Coulomb logarithm describing the cumulative effect of many small angle deflective collisions. In the solar atmosphere, this quantity varies weakly, taking values between 10 and 22. It is interesting to note that while all collisional frequencies involving neutrals (head-on collisions) have a $T^{1/2}$ dependence on the temperature, while the collisions between charged species behave as $T^{-3/2}$. That means that, in the multi-million degree corona, the collisional frequency of these particles becomes very small. Diffusivity due to collisions can be thought of as the spreading out of energy often used to describe the rate at

which particles, energy, or other quantities move from regions of higher concentration or intensity to regions of lower concentration or intensity.

The variation of the collisional frequencies with height is based on the AL C7 atmospheric model (Avrett and Loeser, 2008) and are shown in Figure 2.2. It is clear that with the drop in neutral density with height, the collisional frequencies of charged particles with neutrals tend toward zero, and only the collisions between the charged particles remain a coupling mechanism for higher heights. It is also clear that in the chromosphere ($z > 750$ km) the coupling between ions and electrons is much stronger than than any other coupling, which constitutes the basis of the two-fluid approximation, where charged particles are treated as one single fluid.

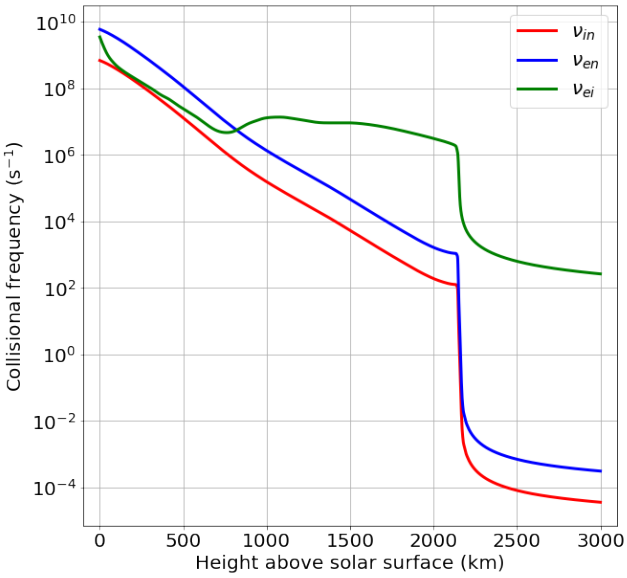

Figure 2.2: The ion-neutral, electron-neutral and electron-ion collisional frequencies are plotted as functions of height above the solar surface based on the AL C7 solar atmospheric model (Avrett and Loeser, 2008).

Following closely the reduction of the momentum conservation equations for the three species as described in detail by Khomenko et al. (2014), it can be shown that when the charged fluids are strongly coupled, the two-fluid form of the momentum conservation equation becomes

$$\rho_i \frac{d\mathbf{v}_i}{dt} = -\nabla p_c + \frac{1}{\mu_0}(\nabla \times \mathbf{B}) \times \mathbf{B} + \rho_i \nu_{in}(\mathbf{v}_n - \mathbf{v}_i) + \nabla \cdot \pi_c, \tag{2.16}$$

$$\rho_n \frac{d\mathbf{v}_n}{dt} = -\nabla p_n - \rho_i \nu_{in}(\mathbf{v}_n - \mathbf{v}_i) + \nabla \cdot \pi_n, \tag{2.17}$$

where π_c and π_n are the non-diagonal components of the pressure tensor describing the viscosity for the charged and neutral fluids, respectively, and μ_0 is the magnetic permeability of free space. We have once again assumed any contribution dependent on collisions with electrons to be small in comparison with collisions between ions and neutrals, given the substantial mass difference between electrons and other particles. The expression of the viscosity coefficients for these plasmas will be discussed later. Note we have used the formula (Vranjes, 2014)

$$\nu_{ab} = \frac{m_b n_b}{m_a n_a} \nu_{ba}, \tag{2.18}$$

to rearrange the neutral-ion collisional frequency for consistency of notation in the above equations. Finally, after defining the total density and the centre of the mass velocity as in Equations (2.1) and (2.2), the momentum conservation equation for a single-fluid plasma becomes (Zaqarashvili et al., 2011; Khomenko et al., 2014)

$$\rho_0 \frac{d\mathbf{v}}{dt} = -\nabla p + \frac{1}{\mu_0}(\nabla \times \mathbf{B}) \times \mathbf{B} + \nabla \cdot \pi - \rho_0 \nabla \cdot (\xi_i \xi_n (\mathbf{v}_c - \mathbf{v}_n)^2). \tag{2.19}$$

The above equation does not contain information about the collisions taking place between particles as the temporal scales involved in this approximation are much longer than the typical collisional times between particles. The off-diagonal terms of the pressure tensor, π, give rise to a viscous force that is obtained after combining the viscous forces of the charged particles and neutrals following the method described above. The last term in Equation (2.19) is due to the inertia of various species and, under solar atmospheric conditions, is very small. In the linear approximation (as used in the present thesis), this term vanishes.

2.3.3 Energy equation and equation of state

The last equations that connect the thermodynamical parameters of the plasma to the dynamic quantities are the energy conservation equation and equation of state. These equations involve the plasma density, pressure and temperature with the particle velocities.

The energy equation for each species α can be written as

$$\frac{\partial p_\alpha}{\partial t} + \mathbf{v}_\alpha \cdot \nabla p_\alpha + \gamma p_\alpha \nabla \cdot \mathbf{v}_\alpha = (\gamma - 1) Q_\alpha, \tag{2.20}$$

where γ is the adiabatic index (taken to be 5/3 throughout the present thesis) and Q_α stands for the heat source associated with the species α and they are defined as $Q_\alpha = \sum_\beta Q_{\alpha\beta}$, with $Q_{\alpha\beta}$ being the heat generated in the fluid made up of particles α as a consequence of collisions with particles of species β. Of course, one could take several dissipative mechanisms that could give a general expression of Q_α as in the study by Khomenko et al. (2014), however, here we are going to restrict ourselves to specific processes that will be discussed in the present study.

Let us introduce the electric current defined as $\mathbf{j} = -en_e(\mathbf{v}_i - \mathbf{v}_e) = -en_e\mathbf{u}$ that appears due to the drift velocity of electrons with respect to positive ions, here denoted by $\mathbf{u}$. In addition we define the drift velocity, $\mathbf{w}$ between ions and neutrals as $\mathbf{w} = \mathbf{v_i} - \mathbf{v_n}$. When charged particles are strongly coupled, the two-fluid energy equations in the most general form are defined as (Zaqarashvili et al., 2011)

$$\frac{\partial p_c}{\partial t} + \mathbf{v}_i \cdot \nabla p_c + \gamma p_c \nabla \cdot \mathbf{v}_i = (\gamma - 1)\frac{\alpha_{ei}}{e^2 n_e^2}|\mathbf{j}|^2 + (\gamma - 1)\alpha_{in}\mathbf{w} \cdot \mathbf{v}_i + \\ + (\gamma - 1)\alpha_{en}(\mathbf{v}_e - \mathbf{v}_n) \cdot \mathbf{v}_e + \frac{(\mathbf{j} \cdot \nabla)p_e}{en_e} + \gamma p_e \nabla \frac{\mathbf{j}}{en_e}, \tag{2.21}$$

and the equivalent energy equation for the neutral fluid is given by

$$\frac{\partial p_n}{\partial t} + \mathbf{v}_n \cdot \nabla p_n + \gamma p_n \nabla \cdot \mathbf{v}_n = -(\gamma - 1)\alpha_{in}\mathbf{w} \cdot \mathbf{v}_n + \\ + (\gamma - 1)\alpha_{en}(\mathbf{v}_n - \mathbf{v}_e) \cdot \mathbf{v}_n. \tag{2.22}$$

where α_{ab} is the coefficient of friction between particle a and b and is given by

$$\alpha_{ab} = n_a m_a \nu'_{ab}, \quad \nu'_{ab} = \frac{m_b}{m_a + m_b}\nu_{ab}. \tag{2.23}$$

These equations show that the heat source terms are all nonlinear and they appear due to the collisions between particles.

When the coupling between particles is very strong and a single-fluid framework is used to describe the evolution of the plasma, the energy conservation law can be written as (Zaqarashvili et al., 2011)

$$\frac{\partial p}{\partial t} + (\mathbf{v} \cdot \nabla)p + \gamma p \nabla \cdot \mathbf{v} - \xi_i(\mathbf{w} \cdot \nabla)p - \gamma p \cdot (\xi_i \mathbf{w}) + (\mathbf{w} \cdot \nabla)p_c + \gamma p_c \nabla \cdot \mathbf{w} = \\ = (\gamma - 1)\frac{\alpha_{ei} + \alpha_{en}}{e^2 n_e^2}|\mathbf{j}|^2 + (\gamma - 1)\alpha_n|\mathbf{w}|^2 - (\gamma - 1)\frac{2\alpha_{en}}{en_e}\mathbf{j} \cdot \mathbf{w} + \frac{\mathbf{j} \cdot \nabla p_e}{en_e} + \\ + \gamma p_e \nabla \cdot \left(\frac{\mathbf{j}}{en_e}\right), \tag{2.24}$$

where α_n is a weighted collisional term given by

$$\alpha_n = \alpha_{in} + \alpha_{en} \tag{2.25}$$

and all the other quantities have been defined earlier. The first term on the right-hand side of Equation (2.24) describes the Joule heating that appears due to the resistance experienced by electrons when colliding with ions and neutrals, the second term is the heating due to the loss of kinetic energy of particles due to collisions, the third term is due to the misalignment between the electric currents and the relative motion of ions, the fourth term appears due to the gradients of electron pressure, and finally the last term is due to the divergence of electric currents. In practice, under solar atmospheric conditions, some of these terms are too small to be worth considering (for details see, e.g., Khomenko et al., 2014; Ballester et al., 2018).

The relationship that connects the thermodynamical quantities (density, pressure and temperature) is the equation of state. For a thermalised plasma (i.e., when the temperature of constituent species are equal) the equation of state for each species becomes $p_\alpha = n_\alpha k_B T$. We assume a quasi-neutral hydrogen plasma, such that $n_e = n_i$, therefore for a two-fluid plasma the equations of state for a charged and neutral species become

$$p_c = (n_i + n_e)k_B T = 2n_i k_B T, \quad p_n = n_n k_B T, \tag{2.26}$$

where the quantity, p, denotes the pressure of the mixture and the subscript c and n refer to the charged and neutral species, respectively. Finally, when the coupling between all particles is high, a single-fluid approximation describes the state and dynamics of the plasma. Then, the equation of state can be written as

$$p = (2n_i + n_e)k_B T. \tag{2.27}$$

2.3.4 Ohm's law and the induction equation

In addition to the fluid equations presented earlier, the plasma is also subject to the Maxwell equations that connect the spatial and temporal evolution of the electric and magnetic fields. In order to derive Ohm's law for a two-fluid plasma, we would need to go back to the equation of motion of electrons (Equation 2.9, with $\alpha = e$). Given their small mass, the electron inertia term can be neglected, therefore the momentum equation for electrons can be rearranged as

$$\mathbf{E} + \mathbf{v}_e \times \mathbf{B} = -\frac{\nabla p_e}{e n_e} + \frac{1}{e n_e}(\alpha_{ei}(\mathbf{v}_i - \mathbf{v}_e) + \alpha_{en}(\mathbf{v}_n - \mathbf{v}_e)). \tag{2.28}$$

Next, we use the expression of electric current

$$\mathbf{j} = -en_e(\mathbf{v}_e - \mathbf{v}_i) \tag{2.29}$$

to express the electron velocity in terms of the ion velocity. As a result, the Ohm's law becomes

$$\mathbf{E} + \mathbf{v}_i \times \mathbf{B} + \frac{1}{en_e}\nabla p_e = \frac{\alpha_e}{e^2 n_e^2}\mathbf{j} - \frac{\alpha_{en}}{en_e}(\mathbf{v}_i - \mathbf{v}_n) + \frac{1}{en_e}\mathbf{j} \times \mathbf{B}. \tag{2.30}$$

Using Faraday's law of induction (one of Maxwell's laws), $\partial\mathbf{B}/\partial t = -\nabla \times \mathbf{E}$, Equation (2.30) can be written as

$$\frac{\partial \mathbf{B}}{\partial t} = \nabla \times (\mathbf{v}_i \times \mathbf{B}) + \nabla \times \left(\frac{\nabla p_e}{en_e}\right) - \nabla \times (\eta \nabla \times \mathbf{B}) -$$
$$-\nabla \times \left(\frac{\mathbf{j} \times \mathbf{B}}{en_e}\right) + \nabla \times \left(\frac{\alpha_{en}(\mathbf{v}_i - \mathbf{v}_n)}{en_e}\right) \tag{2.31}$$

where η is the coefficient of Ohmic diffusion connected to electrons. As the above relation shows, in a partially ionised plasma the electron resistivity is due to the collisions of electrons with both ions and neutrals, more details are given in Section 2.4.3.

In the above equation, the first term on the right-hand side describes the effect of ions being coupled to the magnetic field (often called the advective term), the second term is the Biermann battery term, which occurs due to the electron pressure (in general this term is neglected due to its smallness), the third term is the diffusive term, the next term is the Hall term that gives rise to dispersion over ion inertial lengths, and finally, the last term describes the induced magnetic field due to the relative motion of ions and neutrals.

In order to determine Ohm's law in a single-fluid plasma (and the associated induction equation) when particles are strongly coupled via collisions, we should keep in mind that the equations of motion for species should be written in terms of the center of mass velocity. Following the derivation of Ohm's law in a single-fluid plasma as presented by Khomenko et al. (2014), we add the electron and ion momentum equations multiplied by ξ_n with the momentum equation for neutrals, multiplied by $-\xi_i$. As a result, the relative velocity of ions compared to neutrals can be written as

$$\mathbf{w} = -\frac{\mathbf{G}}{\alpha_n} + \frac{\xi_n}{\alpha_n}\mathbf{j} \times \mathbf{B} + \epsilon\frac{\mathbf{j}}{en_e}, \tag{2.32}$$

where $\epsilon = \alpha_{en}/\alpha_n \ll 1$ and we considered that the electric currents are stationary, meaning that all inertial terms are neglected. The pressure function, $\mathbf{G}$ in the above equation is defined as

$$\mathbf{G} = \xi_n \nabla(p_e + p_i) - \xi_i \nabla p_n.$$

The pressure of the species can be written in terms of the total pressure of the mixture

$$p_e = p_i = \frac{\xi_i}{\xi_i + 1} p, \quad p_n = \frac{\xi_n}{\xi_i + 1} p.$$

As a result, the pressure function, $\mathbf{G}$ can be written as

$$\mathbf{G} = 2\xi_n \nabla \left(\frac{\xi_i p}{\xi_i + 1} \right) - \xi_i \nabla \left(\frac{\xi_n p}{\xi_i + 1} \right) \tag{2.33}$$

Using the expression of electric current, the electron velocity can be expressed in terms of the velocity of the centre of mass and the relative velocity of ions with respect to neutrals as

$$\mathbf{v}_e = \mathbf{v} + \xi_n \mathbf{w} - \frac{\mathbf{j}}{e n_e}. \tag{2.34}$$

As a result, Ohm's law in a single-fluid partially ionised plasma can be written as

$$\begin{aligned} \mathbf{E} + \mathbf{v} \times \mathbf{B} = \frac{\epsilon \mathbf{G} - \nabla p_e}{e n_e} + \mathbf{j}\sigma + \frac{1 - 2\epsilon\xi_n}{e n_e} \mathbf{j} \times \mathbf{B} + \\ + \frac{\xi_n}{\alpha_n} \left[\mathbf{G} \times \mathbf{B} - \xi_n (\mathbf{j} \times \mathbf{B}) \times \mathbf{B} \right], \end{aligned} \tag{2.35}$$

where the quantity σ is the conductivity of electrons and it is defined as

$$\sigma = \frac{n_e e^2}{m_e \nu_e}, \tag{2.36}$$

where ν_e is the collisional frequency of electrons. We can eliminate the electric field from the above equation by means of Faraday's law of induction which leads to the induction equation in a single-fluid plasma

$$\begin{aligned} \frac{\partial \mathbf{B}}{\partial t} = \nabla \times (\mathbf{v} \times \mathbf{B}) - \nabla \times \left(\frac{\epsilon \mathbf{G} - \nabla p_e}{e n_e} \right) - \nabla \times (\eta \nabla \times \mathbf{B}) - \nabla \times \left(\frac{\xi_n}{\alpha_n} \mathbf{G} \times \mathbf{B} \right) - \\ - \nabla \times \left[\frac{1 - 2\epsilon\xi_n}{e n_e \mu_0} (\nabla \times \mathbf{B}) \times \mathbf{B} \right] + \nabla \times \left\{ \frac{\xi_n^2}{\mu_0 \alpha_n} [(\nabla \times \mathbf{B}) \times \mathbf{B}] \times \mathbf{B} \right\}. \end{aligned} \tag{2.37}$$

The terms that appear on the right-hand side of Equation (2.37) are the convective term, Biermann's battery term, Ohm's diffusion, the diamagnetic current

term, Hall's diffusion and ambipolar diffusion, respectively. Under solar atmospheric conditions the battery term is less important (relevant in the presence of large electron pressure), however, it provides a means for magnetic field generation due to electron pressure. The Ohmic diffusion term is due to the collision of electrons with ions and neutrals and describes the dissipation of field-aligned currents. The ambipolar diffusion (that appears mainly due to the collisions of ions with neutrals) describes the dissipation of currents that are perpendicular to the ambient magnetic field. The Hall effect arises in a plasma when, unlike ions, electrons are able to move together with the magnetic field. The drift of electrons generates perpendicular currents (also known as Hall currents), however, this term is responsible for the introduction of additional length scales in the problem of the order of the ion inertial length. That is why, the Hall term describes dispersion, rather than dissipation. Although the Hall term can be, in principle, present even in fully ionised plasmas (at frequencies between the electron and ion cyclotron frequencies), in a partially ionsed plasma the collisions between ions and neutrals are capable of enhancing the magnitude of this term as collisions with neutral particles decouple ions from the magnetic field.

Under the single-fluid MHD approximation, and when disregarding inertial and Hall terms, a cutoff wavenumber emerges for Alfvén waves travelling within a partially ionised plasma (Zaqarashvili et al., 2012). This arises when the real part of the Alfvén frequency reaches zero, resulting in a non-oscillatory mode. However, this phenomenon is purely a methodological artefact stemming from the necessary approximations to derive the conventional single-fluid description from the more comprehensive three-fluid equations (Khomenko et al., 2014). In contrast, a physical cutoff wavenumber exists for standing waves under the two-fluid approach. This occurs when the density ratio of neutrals to ions (ρ_n/ρ_i) surpasses a threshold of 8, indicating a plasma dominated by neutrals. Notably, this condition manifests for ionisation degrees ($\mu > 0.9$). Conversely, when examining propagating waves using a two-fluid approximation, no cutoff frequency is apparent. This absence is due to the presence of static evanescent perturbations, a characteristic solely observed when the parallel wavenumber (k_z) is real and the wave frequency (ω) is purely imaginary—a scenario incompatible with propagating waves (Soler et al., 2013).

Finally, the diamagnetic current term (proportional to $\nabla p_e \times \mathbf{B}$) couples the magnetic field evolution with pressure gradients and its effect is larger for

intermediate values of the ionisation fraction since $\mathbf{G}$ vanishes when we consider a fully ionised or fully neutral plasma. Focusing only on the leading order terms in the induction equation (diffusion term, Hall term and the ambipolar diffusion term), we present the variation of the coefficients that describe the magnitude of these terms in the solar atmosphere in Figure 2.3. While in the photosphere the Ohmic diffusion and Hall coefficient are much larger than the ambipolar diffusion coefficient, in the solar chromosphere the ambipolar diffusion coefficient becomes dominant, and this discrepancy in the values of dissipative coefficients stays at the core of our investigation.

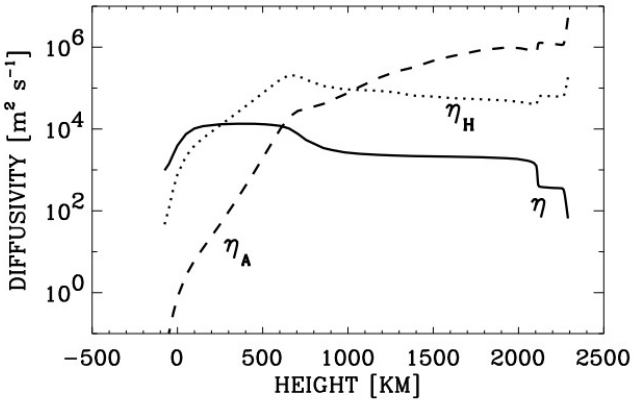

Figure 2.3: The variation of the coefficients that describe the magnitude of the Ohmic diffusion term, Hall term and the ambipolar diffusion term as a function of height above the solar surface, based on the VAL C solar atmospheric model Vernazza et al. (1981). This plot has been adapted from Khomenko et al. (2014).

Finally, the equations must be complemented by the solenoidal condition (or Gauss' law for magnetism) given by

$$\nabla \cdot \mathbf{B} = 0, \tag{2.38}$$

which requires that the magnetic field must consist of closed loops with no sources or sinks, ensuring the conservation of magnetic flux. In other words, this condition requires that any magnetic field line that enters a given volume must exit that volume. This condition remains unchanged when working with non-ideal (resistive) MHD.

2.4 Dissipative processes in partially ionised plasmas

A realistic description of plasma contains terms that describe transport mechanisms that owe their existence to, in the classical picture, collisions, small-scale turbulences or wave-particle interactions. In the present thesis, we are going to concentrate on collisional processes only. The problem of dissipation (also known as transport) in partially ionised plasmas was discussed in detail in pioneering studies such as Braginskii (1965) and Vranjes (2014). Dissipative processes (e.g., viscosity, diffusion, thermal conduction and collisional damping) are mechanisms through which momentum is lost and leads to an attenuation of the amplitudes of physical variables.

On a microscopic level, all dissipative processes considered by us can be attributed to the collision of particles, resulting in the conversion of kinetic and magnetic energy into thermal energy. That is why it is natural to expect that all the dissipative coefficients we are going to consider depend on the collisional frequency between particles. It is evident that the first requirement that needs to be fulfilled in order to consider dissipative processes is that the mean free path of particles (the average distance between two collisions) has to be smaller than the spatial scales of the problem we are investigating and larger than the cyclotron radius of the charged particles. As a consequence of this requirement, particles are tied to magnetic field lines and travel long distances along them between each collision. This leads to heat and momentum transport, which is primarily directed along the local magnetic field direction. As a consequence transport mechanisms become anisotropic, with different heat and momentum transfer along and across the magnetic field. Secondly, we only consider cases when the collisional frequency of particles is much less than the cyclotron frequency of charged particles, $\omega_{c\alpha} = eB/m_\alpha$. The transfer of momentum via collisions between particles has been discussed at length in Section 2.3.2. In this section, we are going to concentrate on the other dissipative mechanisms that are relevant to our research, in particular viscosity, Ohmic diffusion and Ambipolar diffusion. In the partially ionised chromosphere, the dissipative mechanisms are greatly enhanced by the presence of neutrals.

In order to make the treatment of waves as simple as possible, it is commonly assumed that the role of dissipative mechanisms in solar plasmas, such as diffusion and viscosity, are negligible which simplifies the governing equations. In the absence of dissipative processes, the MHD equations are referred

to as the ideal MHD equations, which have been studied extensively. However, the consideration of dissipation in the governing equation can introduce completely new physics and a new framework in which dynamical processes can be described. Phenomena such as shock waves, dissipative instabilities, plasma energisation and solar wind acceleration, cannot be described accurately in an ideal plasma. As dissipation is an essential ingredient for our analysis, we are going to introduce the details of each of these mechanisms separately.

2.4.1 Viscosity in partially ionised plasmas

As mentioned earlier in Section 2.3.2, viscous forces in the momentum equations of various species appear as a consequence of the divergence of the off-diagonal terms of the pressure tensor. When the diagonal terms from this tensor are removed, the remaining tensor is known as the viscosity tensor. Assuming that flow speeds are comparable with the particles' thermal speed, viscosity can be understood as the flux of momentum and represents the various frictional forces at play between two layers of adjacent fluids in relative motion, i.e., the resistance of a fluid to motion or deformation. The anisotropic viscosity in a partially ionised plasma was described in great detail in the pioneering study by Braginskii (1965). In a plasma, where the direction of the magnetic field defines a preferential direction, the viscosity tensor is more complicated, as the transport of momentum occurs at different rates in different directions. In the most general case, the viscosity tensor has five terms, among which the first term is called the kinematic or compressional viscosity, and the second and third terms represent the shear viscosity (for details see, e.g., Braginskii, 1965; Vranjes, 2014).

By their very nature, Alfvén waves do not experience compressional viscosity. In a magnetically dominated plasma, such as the chromosphere, Alfvén waves are affected by shear viscosity that originates from a random walk transport of momentum with a step size equal to the Larmor radius. In a partially ionised plasma, the viscosity of the fluid contains contributions from each species. However, in uni-thermal plasmas, the electron shear viscosity can be negligibly small (proportional to m_e/m_i). Therefore the contribution towards the shear viscosity (ζ) can be considered as the sum of the ion and the neutral shear viscosity coefficients given by

$$\zeta_i = \frac{n_i k_B T \tau_i}{2} \frac{\Delta\gamma_i}{\Delta^2 + (\omega_{ci}\tau_i)^2}, \tag{2.39}$$

and

$$\zeta_n = \frac{n_n k_B T \tau_n}{2} \frac{\Delta\gamma_n + (\omega_{ci}\tau_i)^2}{\Delta^2 + (\omega_{ci}\tau_i)^2}, \tag{2.40}$$

where $\omega_{ci} = eB_0/m_i$ is the ion cyclotron frequency, B_0 is the background magnetic field intensity and τ_i and τ_n are the ion and neutral collision times, respectively. The inverse of these quantities (i.e., the collisional frequencies) are given by

$$\tau_i^{-1} = 0.3\tau_{ii}^{-1} + 0.4\tau_{in}^{-1} + \delta_i\tau_{ie}^{-1} \tag{2.41}$$

and

$$\tau_n^{-1} = 0.3\tau_{nn}^{-1} + 0.4\tau_{ni}^{-1} + \delta_n\tau_{ne}^{-1} \tag{2.42}$$

where $\delta_\alpha = m_e/m_\alpha$ for particle α with $\alpha \neq e$, τ_{ab} being the collisional times between particles a and b that can be calculated using the expressions of the collisional frequencies given by Equations (2.11)–(2.14). The collisional times defined above contain contributions from the collisions between ions and neutrals with other species and also self-interaction. In addition, the quantities Δ, γ_i and γ_n are given in terms of the ionisation degree of the plasma and ratios of various collisional frequencies as

$$\Delta = 1 - \frac{1}{(3\nu_{ii}/\nu_{in} + 4)(3\nu_{nn}/\sigma_d\nu_{in} + 4)} \tag{2.43}$$

where $\sigma_d = (1-\mu)/(2\mu-1) = \xi_i/\xi_n$ is the relative number density of ions with respect to the number density of neutrals and γ_i and γ_n are given as

$$\gamma_i = 1 + \frac{\sigma_d}{3\nu_{nn}/\nu_{in} + 4\sigma_d}, \quad \gamma_n = 1 + \frac{\sigma_d}{3\nu_{ii}/\nu_{in} + 4}. \tag{2.44}$$

The quantities ζ_i and ζ_n are converted to the appropriate units by dividing by the typical density associated with the ionisation degree used to calculate the other quantities. Under chromospheric conditions the neutral shear viscosity is many orders of magnitude larger than the corresponding value for ions (see Figure 2.4), therefore, when considering the total shear viscosity in a single-fluid plasma, the ion shear viscosity can also be neglected. Figure 2.4 displays the variation of the neutral and shear viscosity coefficients as a function of height above the solar surface, where the relative plasma parameters required to calculate these coefficients are taken from the AL C7 atmospheric model (Avrett and Loeser, 2008), assuming a constant magnetic field of 100 Gauss. As a result, the shear viscosity coefficient used in the single-fluid study is given by Equation (2.40).

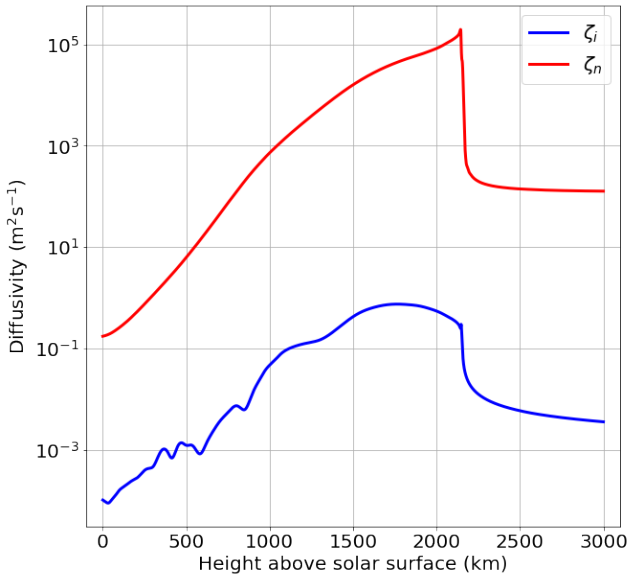

Figure 2.4: The variation of the neutral and ion shear viscosity coefficients with height assuming a constant magnetic field of 100 G. The plasma parameters are taken from the AL C7 atmospheric model (Avrett and Loeser, 2008).

2.4.2 Ambipolar diffusion

The ambipolar diffusion term arises in the induction equation when accounting for the influence of neutrals in a single-fluid partially ionised plasma. Due to their lack of interaction with magnetic forces, and therefore the Lorentz force, neutrals undergo partial decoupling from the magnetic field, and hence, the magnetic field diffuses through the neutral gas. The charged component of the plasma, i.e., ions and electrons, gyrate around the magnetic field lines, while neutrals, devoid of such gyroscopic motion, engage in random collisions with charged particles, contributing to the dissipation of wave energy. Working under the frequency regime of a single-fluid plasma, the effects of ambipolar diffusion are cast in the generalised Ohms law. Equation (2.35) can be rewritten in the form

$$\mathbf{E}+(\mathbf{v}\times\mathbf{B})=\frac{1}{\sigma}\frac{\nabla\times\mathbf{B}}{\mu_0}-\frac{\xi_n^2}{\alpha_n}\left[\frac{((\nabla\times\mathbf{B})\times\mathbf{B})\times\mathbf{B}}{\mu_0}\right]=\frac{1}{\sigma}\mathbf{j}+\frac{\xi_n^2B_0^2}{\alpha_n}\mathbf{j}_\perp, \quad (2.45)$$

where σ is the conductivity due to electrons (defined earlier in Equation 2.36).

Equation (2.45) states that ambipolar diffusion corresponds to the diffusion of currents perpendicular to the magnetic surfaces, while Ohmic diffusion is connected to the diffusion of both parallel and perpendicular currents to the

magnetic field. For a hydrogen plasma, the coefficient of ambipolar diffusion is given by

$$\eta_A = \frac{\xi_n^2 v_A^2}{\nu_{in} + \nu_{en}}. \tag{2.46}$$

It is clear then, that for a fully ionised plasma, $\eta_A = 0$. Ambipolar diffusion in a two-fluid plasma also refers to the process where ions and neutrals drift relative to each other due to the influence of magnetic fields. However, this effect is captured by the differences in fluid velocities rather than a coefficient.

2.4.3 Ohmic diffusion

The Ohmic diffusion coefficient, also known as magnetic diffusion, in a partially ionised plasma is dependent on the collisional frequencies of electrons with ions and neutrals. Its value is given by

$$\eta = \frac{m_e(\nu_{ei} + \nu_{en})}{e^2 n_e \mu_0}. \tag{2.47}$$

Ohmic diffusion is a measure of how easily the magnetic field lines can penetrate and propagate within the plasma, this can also be thought of as the resistance to motion due to the magnetic field. The expression of this coefficient clearly shows that in a partially ionised plasma, the diffusion is enhanced by the presence of neutral particles since the magnetic diffusion is caused not only by the collisions between electrons and ions but also by the collisions between electrons and neutral particles. Under the typical conditions of the quiet Sun, magnetic diffusion is determined mostly by the electron-neutral collisions in the photosphere, and mostly by the electron-ion collisions in the upper chromosphere. Typical values for each of the dissipative coefficients discussed are presented below in Figure 2.5 considering a constant magnetic field of 100 G assuming a standard AL C7 solar atmospheric model (Avrett and Loeser, 2008). Clearly, in the photosphere (the first 500 km above the solar surface) Ohmic diffusion is the dominant dissipative effect due to the high concentration of neutrals. In the solar chromosphere the ambipolar diffusion becomes dominant (by several orders of magnitude), due to the decrease in the number of neutrals and relative increase in the number of charged particles. For the physical problem discussed in the present thesis dissipation is a key ingredient, as in the absence of these processes damping of waves cannot occur.

The focus of this thesis is on Alfvén waves, which propagate in an incompressible plasma and do not perturb the plasma density, hence, we may neglect

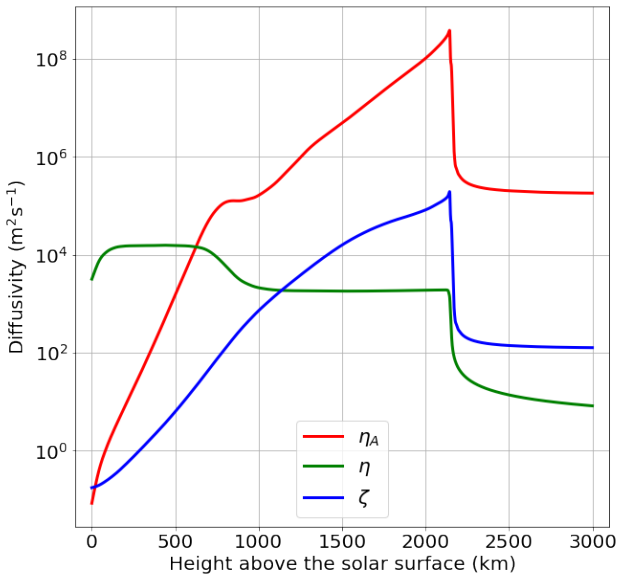

Figure 2.5: The ambipolar diffusion coefficient, Ohmic diffusion coefficient and total shear viscosity coefficient are plotted as functions of height above the solar surface for a constant magnetic field of 100 G. The calculations were carried out considering an AL C7 standard atmospheric model (Avrett and Loeser, 2008).

the pressure gradient. Equally, we assume Alfvén waves do not perturb thermodynamical quantities, so, the equations of continuity and energy together with the equation of state will be redundant. These facts will greatly simplify the modelling challenge. As we specified earlier, for simplicity, we also neglect the effects due to gravity, which plays a second-order role in the investigation of damping phase mixed Alfvén waves in partially ionised plasmas. Note that the gravitational scale height in the fully ionised coronal plasma is usually orders of magnitude larger than the length scales of interest (tens of Mm for $T = 10^6$ K) and hence plays a very minor role, however, in a chromospheric plasma, this is not the case, since the gravitational scale height is much smaller (a few hundred km for $T = 10^4$ K). Gravity stratification works to produce a vertical density gradient in the plasma resulting in a growth in the amplitude of Alfvén waves due to the reduced interaction of the wave with the medium, meaning there are fewer particles to cause resistance to motion. The inclusion of vertical stratification is beyond the scope of this present thesis and is presented in Chapter 7 as a direction for future research.

As a result, the relevant equations that will be used to study the problem of phase mixed Alfvén waves in partially ionised plasmas will be

$$\rho_0 \left(\frac{\partial \mathbf{v}}{\partial t} + \mathbf{v} \cdot \nabla \mathbf{v} \right) = \mathbf{j} \times \mathbf{B} + \zeta \nabla^2 \mathbf{v}, \tag{2.48}$$

and

$$\frac{\partial \mathbf{B}}{\partial t} = \nabla \times (\mathbf{v} \times \mathbf{B}) + \eta \nabla^2 \mathbf{B} + \nabla \times \left\{ \frac{\eta_A}{|\mathbf{B}|^2} \left[(\nabla \times \mathbf{B}) \times \mathbf{B} \right] \times \mathbf{B} \right\}, \tag{2.49}$$

in a single-fluid plasma, while in a two-fluid framework, the governing equations will be written as

$$\rho_i \left(\frac{\partial \mathbf{v}_i}{\partial t} + \mathbf{v}_i \cdot \nabla \mathbf{v}_i \right) = \mathbf{j} \times \mathbf{B} + \rho_i \nu_{in} (\mathbf{v}_n - \mathbf{v}_i) + \rho_i \zeta_i \nabla^2 \mathbf{v}_i, \tag{2.50}$$

$$\rho_n \left(\frac{\partial \mathbf{v}_n}{\partial t} + \mathbf{v}_n \cdot \nabla \mathbf{v}_n \right) = -\rho_i \nu_{in} (\mathbf{v}_n - \mathbf{v}_i) + \rho_n \zeta_n \nabla^2 \mathbf{v}_n, \tag{2.51}$$

and

$$\frac{\partial \mathbf{B}}{\partial t} = \nabla \times (\mathbf{v}_i \times \mathbf{B}), \tag{2.52}$$

where ζ_i and ζ_n are the shear viscosity coefficients given by Equations (2.39) and (2.40), respectively.

2.5 Linearised MHD equations

The MHD equations presented in the previous section pose a great challenge as these contain quadratic and cubic nonlinear terms, making their mathematical handling rather difficult. One way to circumvent this difficulty is to consider only small amplitude changes in the variables. The physical system consists of two stages: (i) the equilibrium state where all forces are balanced, and plasma elements can be static, stationary and homogeneous, and (ii) a perturbed state, when all physical quantities are perturbed so that they can be written as $g = g_0 + g_1$ where g_0 denotes an equilibrium value and g_1 denotes a small perturbation. Given the "smallness" of perturbations, any product of perturbed quantities can be neglected. These considerations form the so-called linearisation technique. Since the research summarised in the present thesis deals with the study of waves, we will assume that perturbations are oscillatory in space and time.

Throughout this thesis, we will assume a homogeneous magnetic field along the z axis and we consider Alfvén waves that propagate along the magnetic field and are linearly polarised along the y direction. Therefore, we write

$$\mathbf{v} = 0 + v(x, z, t)\hat{\mathbf{y}}$$

$$\mathbf{B} = B_0\hat{\mathbf{z}} + b(x, z, t)\hat{\mathbf{y}}$$

in a single-fluid plasma and

$$\mathbf{v}_i = 0 + v_i(x, z, t)\hat{\mathbf{y}},$$

$$\mathbf{v}_n = 0 + v_n(x, z, t)\hat{\mathbf{y}},$$

and

$$\mathbf{B} = B_0\hat{\mathbf{z}} + b(x, z, t)\hat{\mathbf{y}},$$

in a two-fluid plasma. Here $\hat{\mathbf{y}}$ and $\hat{\mathbf{z}}$ are the unit vectors in the y and z directions, respectively. In order to ensure non-linear effects are not important, we require that the ratio of the velocity perturbation to the local Alfvén speed does not considerably exceed ≈ 0.1 (Prokopyszyn et al., 2019).

Phase mixing will occur if either the equilibrium magnetic field or density (or both) are functions that depend on a transversal coordinate, e.g., x. Throughout this thesis, an inhomogeneous density profile and a constant magnetic field is always chosen deliberately. We include comprehensive details for deriving the governing equation to follow in Appendix A.

With the inclusion of constant (height-independent) diffusion, viscosity, and ambipolar diffusion, the linearised incompressible induction and momentum equations in a single-fluid plasma reduce to

$$\frac{\partial b}{\partial t} = B_0 \frac{\partial v}{\partial z} + \eta \left(\frac{\partial^2 b}{\partial x^2} + \frac{\partial^2 b}{\partial z^2} \right) + \eta_A \frac{\partial^2 b}{\partial z^2}. \tag{2.53}$$

and

$$\frac{\partial v}{\partial t} = \frac{B_0}{\mu_0 \rho_0(x)} \frac{\partial b}{\partial z} + \zeta \left(\frac{\partial^2 v}{\partial x^2} + \frac{\partial^2 v}{\partial z^2} \right), \tag{2.54}$$

respectively. We can combine these two equations and eliminate the velocity perturbation, v, to obtain a single governing equation describing the evolution of a magnetic field perturbation given by

$$\begin{aligned} \frac{\partial^2 b}{\partial t^2} = v_A^2(x) \frac{\partial^2 b}{\partial z^2} + \left[(\eta + \zeta) \frac{\partial^2}{\partial x^2} + (\eta_C + \zeta) \frac{\partial^2}{\partial z^2} \right] \frac{\partial b}{\partial t} \\ - \zeta \left[\eta \frac{\partial^2}{\partial x^2} + \eta_C \frac{\partial^2}{\partial z^2} \right] \nabla^2 b. \end{aligned} \tag{2.55}$$

In a two-fluid plasma, the length scales involved in the problem are much shorter than the length scales characteristic of a single-fluid plasma. In this case, the dynamics of the plasma are mainly controlled by the collisions between particles. Due to the decrease in the number density of particles with height, the frequency of collisions will also decrease (despite an increase in the temperature). As a result of this, the magnetic field begins to dominate the dynamics of the plasma. In a partially ionised plasma, the neutral species do not directly experience the magnetic field and hence undergo a partial decoupling from the ionised plasma when the collisional timescales between the ionised plasma and neutral gas become equal to or larger than the MHD timescales. The classical MHD framework becomes inadequate when investigating perturbations with frequencies higher (or of equal order) than those of the collisional frequencies between particles. Current observational resolution does not reach scales where ion-neutral effects can be detected directly in solar atmospheric plasma. However, the presence of neutrals is proven by observations in various wavelengths (e.g., H_α) and spectroscopic measurements.

Similar to the single-fluid treatment, our initial step involves defining the equations that govern the magnetic field and velocity perturbations in a two-component plasma. This enables us to derive a governing equation that we look to solve in order to examine the impact of phase mixing on the damping of Alfvén waves in a partially ionised plasma.

We begin by linearising the equations of motion for the two species and the induction equation assuming a static equilibrium and constant background magnetic field. We satisfy the condition for phase mixing by assuming an inhomogeneous background density profile. The linearised equations of motion are now given by

$$\frac{\partial v_i}{\partial t} = \frac{B_0}{\mu_0 \rho_i(x)} \frac{\partial b}{\partial z} + \tilde{\nu}_{in}(x) \left(v_n - v_i\right) + \zeta_i \nabla^2 v_i, \tag{2.56}$$

and

$$\frac{\partial v_n}{\partial t} = -\frac{\rho_i(x)}{\rho_n(x)} \tilde{\nu}_{in}(x) \left(v_n - v_i\right) + \zeta_n \nabla^2 v_n. \tag{2.57}$$

Note that throughout this investigation, we assume that both charge and neutral densities are functions of x in such a way that their ratio is constant. This leads to $\tilde{\nu}_{in}(x)$ also being required to be a function of x given the linear dependence of density on the collisional frequency. For simplicity, the spatial dependence of the viscosity is neglected. With these considerations, the linearised induction equation is given by

$$\frac{\partial b}{\partial t} = B_0 \frac{\partial v_i}{\partial z}. \tag{2.58}$$

We note that no v_n term appears here since the neutral particles do not directly experience the magnetic field, rather, their presence in the system is maintained through collisions with ions. In order to solve this system of equations we eliminate the dependence of the magnetic field perturbation and the neutral velocity perturbation in favour of modelling the evolution of the charged fluid velocity perturbation. As a result, the spatial and temporal evolution of the velocity perturbation of the charged species is given by

$$\begin{aligned}\frac{\partial^3 v_i}{\partial t^3} = {} & v_A^2(x) \frac{\partial^3 v_i}{\partial z^2 \partial t} - \tilde{\nu}_{in}(x) \frac{\partial^2 v_i}{\partial t^2}(\chi + 1) + \tilde{\nu}_{in}(x) v_A^2(x) \chi \frac{\partial^2 v_i}{\partial z^2} + \\ & + \tilde{\nu}_{in}(x) \zeta_n \nabla^2 \left(\frac{1}{\tilde{\nu}_{in}(x)} \left\{ \frac{\partial^2 v_i}{\partial t^2} - v_A^2(x) \frac{\partial^2 v_i}{\partial z^2} - \zeta_i \nabla^2 \frac{\partial v_i}{\partial t} + \tilde{\nu}_{in}(x) \frac{\partial v_i}{\partial t} \right\} \right) \\ & + \zeta_i \nabla^2 \frac{\partial^2 v_i}{\partial t^2} + \tilde{\nu}_{in}(x) \zeta_i \chi \nabla^2 \frac{\partial v_i}{\partial t}.\end{aligned} \tag{2.59}$$

For full details of the derivation of Equation (2.59), please see Appendix B. In the above equation, the constant density ratio between charges and neutrals is denoted by χ.

2.6 Dispersion relations

Dispersion relations describe how the phase velocity of waves depends on their frequency and wavenumber and solutions to these relations can provide insights into their propagation dynamics in physical environments. Given the dispersion relation, one can calculate the frequency-dependent phase velocity and group velocity of a wave in a medium such as a magnetised plasma as a function of frequency. In the present thesis we discuss propagating waves only. For this reason we assume a purely real frequency (ω) throughout, and solve the dispersion relation to find a complex wavenumber, k.

2.6.1 Single-fluid approximation

In a single fluid plasma, we obtain our dispersion relation by assuming the magnetic field perturbation, $b \propto \exp\{-i(\omega t - kz)\}$, representing a forward propagating wave. Inserting this into Equation (2.55) and assuming homogeneity, we obtain the following dispersion relation

$$\omega^2 + i(\eta_C + \zeta)k^2\omega - v_A^2 k^2 - \eta_C \zeta k^4 = 0, \tag{2.60}$$

which can be written in terms of k as

$$\eta_C \zeta k^4 + k^2\left(v_A^2 - i\omega(\eta_C + \zeta)\right) - \omega^2 = 0. \tag{2.61}$$

In the absence of viscosity, Equation (2.61) reduces to

$$k^2\left(v_A^2 - i\omega(\eta_C + \zeta)\right) - \omega^2 = 0, \tag{2.62}$$

which has solutions

$$k = \pm\frac{\omega}{\sqrt{v_A^2 - i\omega\eta_C}}, \tag{2.63}$$

where k can be separated into real (k_R) and imaginary (k_I) components that take the form

$$k_R = \pm\frac{\omega}{\sqrt{\sqrt{v_A^4 + \omega^2\eta_C^2}}}\cos\left(\frac{\arctan\left(\frac{-\omega\eta_C}{v_A^2}\right)}{2}\right) \tag{2.64}$$

and

$$k_I = \mp\frac{\omega}{\sqrt{\sqrt{v_A^4 + \omega^2\eta_C^2}}}\sin\left(\frac{\arctan\left(\frac{-\omega\eta_C}{v_A^2}\right)}{2}\right), \tag{2.65}$$

such that $k = k_R + ik_I$, which states that with an increased Cowling diffusion, wave frequency or reduced Alfvén speed, a larger (absolute) value of k_I is obtained resulting in more effective damping (since the damping length is proportional to $1/k_I$). For the case where Cowling diffusion is neglected in favour of viscosity, then Equations (2.64) and (2.65), take the same form, replacing η_C with ζ. In the absence of both viscosity and Cowling diffusion, k_I tends to zero and k_R tends to $\pm\omega/v_A$, the typical dispersion relation for Alfvén waves propagating in an ideal homogeneous plasma, without attenuation.

Equation (2.61) requires us to solve a quartic in k, which posses solutions which are non trivial to interpret and this is left for future work.

2.6.2 Two-fluid approximation

In a two-fluid plasma, we obtain our dispersion relation by assuming our ion velocity perturbation, $v_i \propto \exp\{-i(\omega t - kz)\}$. Inserting this into Equation (2.59) and assuming homogeneity, we obtain the following dispersion relation

$$\begin{aligned}\omega^3 + ik^2(\zeta_i + \zeta_n)\omega^2 + i\tilde{\nu}_{in}(\chi + 1)\omega^2 - k^2\tilde{\nu}_{in}(\zeta_n + \chi\zeta_i)\omega - \\ - k^4\zeta_i\zeta_n\omega - k^2v_A^2\omega - ik^2\tilde{\nu}_{in}\chi v_A^2 - ik^4v_A^2\zeta_n = 0.\end{aligned} \tag{2.66}$$

In the absence of viscosity, this relation matches Equation (14) from Soler et al. (2013), who presented results for propagating and standing Alfvén waves in partially ionised plasmas. Figure 2.6 represents the results of propagating Alfvén waves adapted from their paper.

These results show that in the case of propagating Alfvén waves, the damping lengths (proportional to $1/k_I$) and wavelengths (proportional to $1/k_R$) are dependent on the collisional frequency of neutrals with ions. Optimum damping is achieved when the ratio of the collisional frequency between neutrals and ions and the frequency of the waves is close to unity, while an increased collisional frequency between neutrals and ions results in an increased real wavenumber suggesting that collisions reduce the phase speed (and subsequently reduce the wavelength) of the wave (this result is also observed in our simulations in Chapter 6).

Assuming an ideal plasma, Equation (2.66) simplifies to

$$\omega\left(\omega^2 - k^2v_A^2\right), \tag{2.67}$$

which possesses solutions $\omega = \pm kv_A$ and $\omega = 0$. The first two solutions represent the standard Alfvén wave dispersion relation with no damping, while the second represents a non-propagating (entropy) mode.

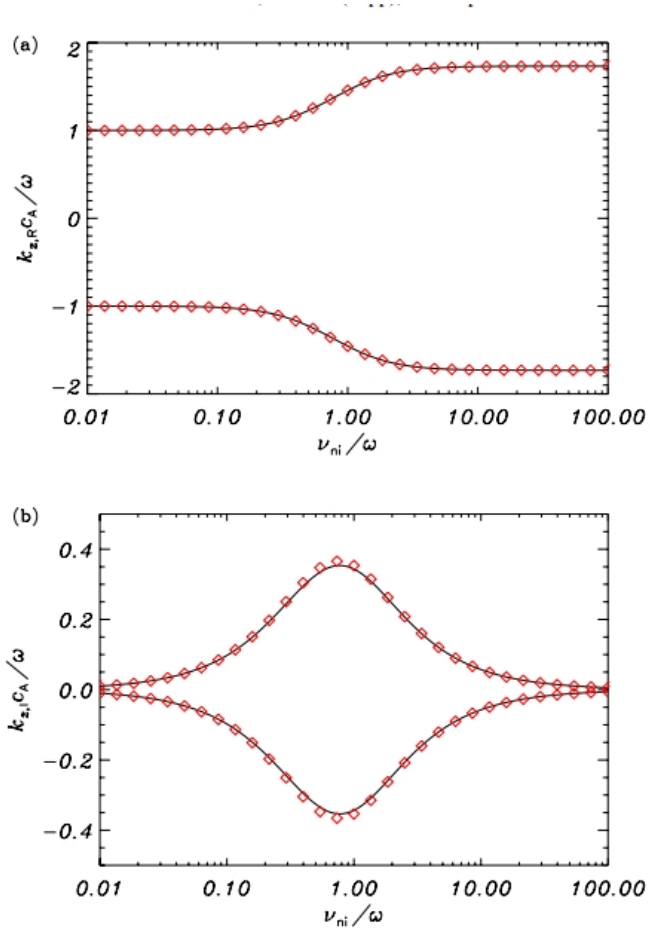

Figure 2.6: Figure 4 from Soler et al. (2013). Results for propagating waves. (a) $k_{z,R}c_A/\omega$ and (b) $k_{z,I}c_A/\omega$ as functions of ν_{ni}/ω, where c_A represents the Alfvén speed. Solid lines correspond to the numerical results, while symbols correspond to the analytic approximations (their Equations (37) and (38)). $\chi = 2$ has been used, note that their use of χ differs from the present thesis.

Equation (2.66) can be rewritten as a quartic equation in k as

$$\begin{aligned}&\zeta_n \left(\zeta_i \omega + v_A^2\right) k^4 + \omega \left(v_A^2 + \nu_{in}(\zeta_n + \chi\zeta_i)\right) k^2 \\ &+ i \left(\nu_{in} v_A^2 \chi - \omega^2(\zeta_n + \zeta_i)\right) k^2 - \omega^3 - i\nu_{in}(\chi + 1)\omega^2 = 0.\end{aligned} \tag{2.68}$$

Equation (2.68) presents significant challenges both in solving and in interpreting its solutions, therefore, we do not provide solutions here and leave this as a topic for future work. However, it is important to note, as highlighted by Soler et al. (2013), that the damping length and wavelength of Alfvén waves in partially ionised plasmas are highly sensitive to variations in the ion-neutral collisional frequency. We anticipate that these two quantities will vary substantially with the ionisation degree, that influences not only the collisional frequency but also the effects of shear viscosity.

While a comprehensive discussion on the numerical solutions to Equation (2.59) is deferred to Chapter 6, certain characteristic behaviours deserve attention. When exploring the impact of varying ionisation degrees, it becomes evident that the collisional frequency, shear viscosityies, and the ratio between charge and neutral densities also undergo variation. Several terms within Equation (2.59) involve the (square of the) Alfvén speed multiplying these ionisation degree-dependent quantities. Consequently, an alteration in the ionisation degree will lead to variations in the propagation speed as the number density of charged particles attached to magnetic field lines changes. This effect is analogous to that presented in Figure 2.6, where the collisional frequency, an ionisation degree dependent quantity, affects the real part of the complex wavenumber. Such variations are anticipated in the lower solar atmosphere, where the Alfvén speed is expected to undergo significant changes over a height range of approximately 2.5 Mm above the solar surface. In a single-fluid plasma, variation of the Alfvén speed with ionisation degree, and therefore height, is seen typically when vertical stratification of the magnetic field and/or density is assumed.

We now present the structure of the numerical programs designed to solve Equations (2.55) and (2.59).

CHAPTER 3
Numerical modelling

While analytical solutions, such as D'Alembert's solution, are able to capture the behaviour of Alfvén waves propagating in a homogeneous ideal plasma, as we endeavor to simulate the propagation of waves within more realistic solar structures characterised by unique density inhomogeneities, we find that analytical methods become insufficient. That is why it becomes essential to employ numerical models to find approximate solutions and forego the pursuit of analytical solutions. Under realistic solar conditions, it is normal to expect that the Alfvén speed depends on longitudinal and transversal coordinates, making the governing equation of Alfvén waves a differential equation with inhomogeneous coefficients. While a dependence on the longitudinal coordinate of the propagation speed can be relatively easily resolved by means of the WKB approximation, a dependence on the transversal coordinate is something that needs special attention. In this case, waves on neighbouring magnetic field lines can oscillate out of phase. This behaviour cannot be accurately captured by D'Alembert's solutions or any other analytical equations, hence to model waves in these inhomogeneous structures necessitates the use of numerical methods to find approximate solutions.

The concept underlying numerical modelling uniquely contrasts with analytical solutions. For an equation that has an analytical solution, we may explicitly write down a formula to determine a solution's value for any desired input, i.e., for any value of the spatial or temporal variables. In contrast, numerical modelling requires us to divide the domain of interest into discrete points before solving the equation for these specific points. The numerical domain we work in then allows us to describe the collective behaviour of the plasma as a weighted average of a discrete domain consisting of individual interacting field lines. Through this approach, we are able to solve far more complex systems of equations with remarkable precision. After satisfying simulation tests to ensure a suitable resolution is obtained, we believe that our

simulations are able to offer accurate insight into the problems we seek to address.

The objective of this chapter is to provide a detailed account of my efforts in constructing a numerical solver designed specifically to investigate the attenuation of phase-mixed Alfvén waves in a partially ionised plasma and estimate the resultant heat generated. We will discuss the various numerical methods employed by this numerical model, we discuss how we can reduce an equation to a system of equations that can be represented in matrix form. We explore initial conditions and boundary conditions, and how these are implemented. We will also present some of the validation and testing steps carried out before using this model to solve Equation (2.55). We will also discuss a second numerical model that we have constructed to study higher frequency Alfvén waves (of the order of the collisional frequency of ions and neutrals), which solves the governing equation of Alfvén waves (Equation 2.59) in a two-fluid framework.

3.1 Numerical techniques

Numerical techniques allow us to forgo the constraints of analytical solutions, opting for an approximate solution in place of an equation without a known solution. Equation (2.55) is a partial differential equation meaning it has both spatial and temporal derivatives. Using finite difference approximations allows us to remove spatial derivatives from Equation (2.55) in favour of algebraic expressions, which allows us to use the Runge-Kutta fourth-order (RK4) method to solve the time-dependent part of our equation. The Runge-Kutta method is perhaps the most widely used time-stepping algorithms in modern numerical codes (see, e.g., Stone et al., 2020; Mignone et al., 2007). It can be thought of as an extension of Euler's method, one of the earliest and most powerful numerical methods developed in the 18^{th} century (Euler, 1768). To understand the concept behind these time-stepping algorithms and the decision to use the RK4 method, let us start by introducing Euler's method.

3.1.1 Euler's method

Euler's method is a simple algorithm that proceeds in small steps to approximate the solution of an initial value problem for a first-order ordinary differential equation (ODE) of the form

$$\frac{dy}{dt} = f(t, y), \tag{3.1}$$

where $f(t, y)$ is a given function representing the rate of change of the function y with respect to the variable t. Since we are dealing with a first-order ODE, a particular solution can be found provided an initial condition is specified, i.e., $y(t_0) = y_0$. Rather than working in continuous time or space domain, we split up the domain we wish to work over into small steps of constant size h. The smaller the step size, the more accurate the approximate solution will be, albeit more time (or more computing resources) consuming. We then iterate a calculating scheme over many time steps starting from our initial condition $y(t_0) = y_0$.

The algorithm works using the following steps

- Step 1: Start with the initial condition (t_0, y_0)
- Step 2: At each step, i, compute the slope of the tangent line at the current point (t_i, y_i) using the function $f(t_i, y_i)$.
- Step 3: Approximate the next point (t_{i+1}, y_{i+1}) by moving a distance h along the tangent line by $t_{i+1} = t_i + h$ and $y_{i+1} = y_i + hf(t_i, y_i)$
- Step 4: Repeat this process until the desired endpoint or number of steps is reached.

Euler's method is a first-order method, meaning that the error in the approximation typically decreases linearly with the step size h, i.e., smaller step sizes lead to more accurate solutions. While Euler's method is straightforward to implement, it may not always provide highly accurate results, especially for stiff ODEs or when the step size is too large. Since phase mixing works by creating large transversal gradients, Euler's method is likely insufficient for our study.

3.1.2 Runge-Kutta fourth-order method (RK4)

The RK4 method is a numerical technique employed when solving ODEs that can be represented by Equation (3.1). Similar to Euler's method, RK4 operates by approximating the solution of an ODE at discrete time points only now the solution is advanced in time through a weighted average of multiple slope estimates at different points within the interval rather than one single approximation. This allows RK4 to accommodate larger time steps compared to Euler's method, enhancing its efficiency in numerical approximation and also dealing with steep gradients more accurately.

For our purposes implementing the RK4 method involves initialising the perturbation that can be done by establishing an unperturbed straight magnetic field line, achieved by setting the values of the initial condition to zero. To introduce wave-like perturbations, a time-dependent driver can then be utilised. Additionally, the initial gradient of the solution domain is required by the RK4 method. This gradient can be determined using the ODE itself; for instance, assigning an initial profile to the perturbation allows for the initial gradient to be calculated constituting the second initial condition. For the case of the magnetic field line initially unperturbed, the second initial condition is also set to zero. The time-dependency of the driver then influences the magnetic field line at each point, i.e., as the wave is excited, the initial conditions reflect the perturbed field line.

Given an equation of the form given by Equation (3.1), we may progress forward in time by summing together the four Runge-Kutta coefficients as follows

$$y_{t+1} = y_t + \frac{1}{6}(k_1 + 2k_2 + 2k_3 + k_4), \tag{3.2}$$

where t is denotes the current time step. The various k_i values are calculated at each point in our domain, and their expressions are given by

$$\begin{aligned} k_1 &= hf(t_n, y_n), \\ k_2 &= hf\left(t_n + \frac{h}{2}, y_n + h\frac{k_1}{2}\right), \\ k_3 &= hf\left(t_n + \frac{h}{2}, y_n + h\frac{k_2}{2}\right), \\ k_4 &= hf(t_n + h, y_n + hk_3). \end{aligned} \tag{3.3}$$

Before we can implement the RK4 method, we must find a way to eliminate the spatial derivatives from our governing equation. Finite difference approximations provide us with a means to achieve this.

3.1.3 Finite difference approximations

Finite difference approximations are a class of numerical methods used to solve differential equations. They work by subdividing the domain of the differential equation into a grid of discrete points and approximating the derivatives using the differences between values at these discrete points. The formulae for the relevant finite difference approximations of spatial derivatives required to solve Equation (2.55) are given as

$$\frac{\partial^2 b}{\partial z^2} = \frac{1}{(\Delta z)^2}(b_{i,j+1} - 2b_{i,j} + b_{i,j-1}), \tag{3.4}$$

$$\frac{\partial^2 b}{\partial x^2} = \frac{1}{(\Delta x^2)}(b_{i+1,j} - 2b_{i,j} + b_{i-1,j}), \tag{3.5}$$

$$\frac{\partial^4 b}{\partial x^4} = \frac{1}{(\Delta x)^4}(b_{i+2,j} - 4b_{i+1,j} + 6b_{i,j} - 4b_{i-1,j} + b_{i-2,j}), \tag{3.6}$$

$$\frac{\partial^4 b}{\partial z^4} = \frac{1}{(\Delta z)^4}(b_{i,j+2} - 4b_{i,j+1} + 6b_{i,j} - 4b_{i,j-1} + b_{i,j-2}), \tag{3.7}$$

$$\begin{aligned}\frac{\partial^4 b}{\partial x^2 \partial z^2} =& \frac{1}{(\Delta x)^2(\Delta z)^2}(b_{i+1,j+1} - 2b_{i,j+1} + b_{i-1,j+1} - 2b_{i+1,j} + 4b_{i,j} \\ & - 2b_{i-1,j} + b_{i+1,j-1} + 2b_{i,j-1} + b_{i-1,j-1}),\end{aligned} \tag{3.8}$$

where i represents the x coordinate, j represents the z coordinate and Δx and Δz represents the spatial step size in the x and z directions, respectively, which is the distance between adjacent points on the spatial grid. These approximations convert Equation (2.55) from second-order and Equation (2.59) from a third-order PDE into a second-order and third-order ODE, respectively. In order to employ the RK4 method, we need to further reduce these equations to a system of coupled first-order equations.

3.1.4 Rewriting the governing equation in a single-fluid approximation

Equation (2.55) can be reformulated as a system of two first-order PDEs by introducing a new variable U. The system of equations can then be written as

$$\frac{\partial b}{\partial t} = U, \tag{3.9}$$

$$\frac{\partial U}{\partial t} = v_A^2(x)\frac{\partial^2 b}{\partial z^2} + \left[(\eta + \zeta)\frac{\partial^2}{\partial x^2} + (\eta_C + \zeta)\frac{\partial^2}{\partial z^2}\right] U - \zeta\left[\eta\frac{\partial^2}{\partial x^2} + \eta_C\frac{\partial^2}{\partial z^2}\right]\nabla^2 b. \tag{3.10}$$

Reducing Equation (2.55) to a system of first-order equations removes direct time derivatives from the right-hand side of Equation (2.55), in place of our new variable U. The spatial derivatives remain unchanged and hence we continue to use Equations (3.4)–(3.8), to approximate them.

In a partially ionised plasma, the dissipative coefficients, as presented in Chapter 2, are often very large, too large for a numerical code to handle. For

this reason, (among others such as the magnitude of the Alfvén speed), we must first reduce Equation (2.55) to a non-dimensional form. Following Hood et al. (2002), we write all quantities in dimensionless form by

$$\begin{aligned} \bar{x} &= \frac{x}{L}, \quad \bar{z} = \frac{z}{L}, \quad \bar{v}_A = \frac{v_A}{v_{A0}}, \quad \bar{t} = \frac{t v_{A0}}{L}, \\ \bar{\eta} &= \frac{\eta}{L v_{A0}}, \quad \bar{\zeta} = \frac{\zeta}{L v_{A0}}, \quad \bar{\eta_C} = \frac{\eta_C}{L v_{A0}}, \quad \bar{\rho} = \frac{\rho}{\rho_0}, \end{aligned} \tag{3.11}$$

where L is the length scale of the problem and $v_{A0} = B_0/\sqrt{\mu_0 \rho_0}$ is the typical Alfvén speed. Bars are subsequently dropped for convenience and the form of Equation (2.55) remains unaltered by this process.

3.1.5 Matrix method

Having established the numerical methods necessary to transform a second and third-order PDE into a solvable system of first-order ODEs, we now focus on performing efficient calculations of the RK4 coefficients discussed in Section 3.1.2. The coefficients of the finite difference approximations can be organised into a matrix structure. Calculating the coefficients of the RK4 method given by Equation (3.3) is achieved by matrix-column vector calculations. However, the presence of an inhomogeneous density profile, essential to modelling phase mixing, implies varying behaviour of each magnetic field line in the domain. This complexity cannot be adequately captured by considering the evolution of an Alfvén wave along a single magnetic field line, as is feasible in a homogeneous plasma. Instead, we must address the MHD equations across all field lines within our domain simultaneously. As a result, the domains of b and U are not currently represented by single column vectors, but instead, constitute two-dimensional matrices of points, where each column signifies a magnetic field line. This can be seen by the need for a separate index for each spatial coordinate in Equations (3.4)–(3.8). This complicates the calculations required to take the next time step using matrix-vector multiplication at this stage, given that our domain is also a matrix.

To address this, we collapse the dimensions of b and U from two-dimensional domains, into a single dimension. Initially, we considered b and U to have square domains of $(n+1) \times (n+1)$ points, where i and j vary from zero to n in the finite difference approximations given by Equations (3.4)–(3.8). We introduce a new variable, l, to index these points, where $l = i(n+1) + j$, such that now l varies between zero and $(n+1)^2 - 1$, effectively stacking each magnetic field line represented by the matrix of points in b on top of one other

to form one large column vector. This alteration of dimensions was necessary to capture the effects of phase mixing and include cross-field gradients as well as longitudinal gradients. Taking into consideration the change of variable, the finite difference formulae are now given by

$$\frac{\partial^2 b}{\partial z^2} = \frac{1}{(\Delta z)^2}(b_{l+1} - 2b_l + b_{l-1}), \tag{3.12}$$

$$\frac{\partial^2 b}{\partial x^2} = \frac{1}{(\Delta x^2)}(b_{l+(n+1)} - 2b_l + b_{l-(n+1)}), \tag{3.13}$$

$$\frac{\partial^4 b}{\partial x^4} = \frac{1}{(\Delta x)^4}(b_{l+2(n+1)} - 4b_{l+(n+1)} + 6b_l - 4b_{l-(n+1)} + b_{l-2(n+1)}), \tag{3.14}$$

$$\frac{\partial^4 b}{\partial z^4} = \frac{1}{(\Delta z)^4}(b_{l+2} - 4b_{l+1} + 6b_l - 4b_{l-1} + b_{l-2}), \tag{3.15}$$

$$\begin{aligned}\frac{\partial^4 b}{\partial x^2 \partial z^2} = \frac{1}{(\Delta x)^2(\Delta z)^2}(&b_{l+(n+1)+1} - 2b_{l+1} + b_{l-(n+1)+1} - 2b_{l+(n+1)} + 4b_l - \\ &- 2b_{l-(n+1)} + b_{l+(n+1)-1} + 2b_{l-1} + b_{l-(n+1)-1}),\end{aligned} \tag{3.16}$$

$$\frac{\partial b}{\partial z} = \frac{1}{2\Delta z}\left(b_{l+1} - b_{l-1}\right), \tag{3.17}$$

where $n+1$ still represents the dimension of the domain. By transforming the spatial derivatives in Equation (2.55) using the above finite difference approximations, we can represent Equations (3.9)–(3.10) in matrix-vector form as

$$\frac{\partial}{\partial t}\begin{bmatrix} b \\ U \end{bmatrix} = A \begin{bmatrix} b \\ U \end{bmatrix}, \tag{3.18}$$

where the matrix A contains the coefficients of the finite difference approximations and the vector containing b and U contains the values of the solution at each grid point. Now we can use matrix algebra to update the solution. The next time step is calculated by multiplying the matrix A by the column vector according to Equation (3.3), before summing together the coefficients as given by Equation (3.2).

We consider the matrix A to be made up of four sub-matrices each further made up of many smaller block matrices of dimension $(n+1) \times (n+1)$. Each

smaller block matrix multiplies an $(n+1) \times 1$ section of the larger column vector representing either a single magnetic field line, b, or its time derivative, U.

All z-derivatives can be contained within a single block matrix, as seen by the new finite difference approximations. However, due to the definition of l, the finite difference approximations that represent x-derivatives exceed the dimensions of each smaller sub-matrix, hence, these coefficients are found in fringe blocks off the main diagonal block structure, allowing for the variation across the field. These calculations produce the effects caused by phase mixing in our simulation.

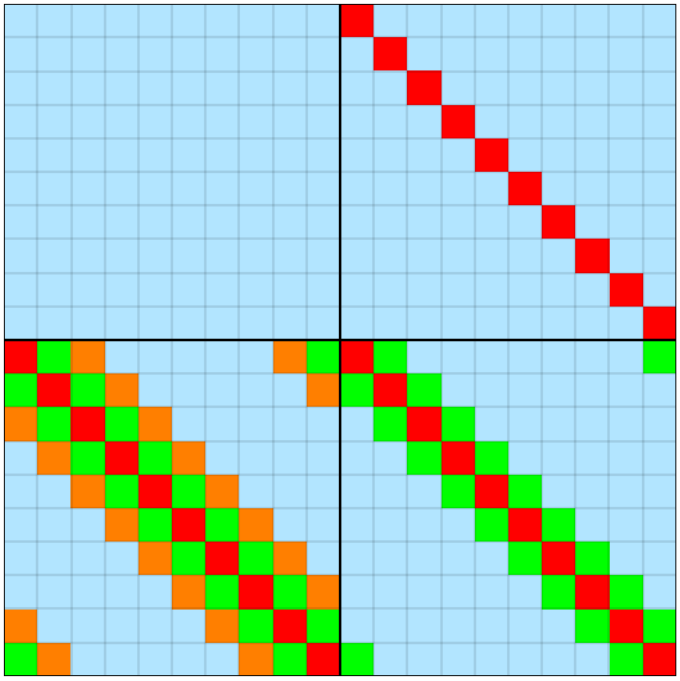

Figure 3.1: Matrix A with dimensions $2(n+1)^2 \times 2(n+1)^2$ consisting of the smaller matrices (denoted by top-left, top-right, bottom-left and bottom-right) populated by sub-matrix blocks with dimensions $(n+1) \times (n+1)$. The blue-coloured blocks consist entirely of zeros, while the other coloured blocks are populated by the coefficients of finite difference approximations. Note that here we used periodic boundary conditions in the x direction exemplified by the matrix blocks in the top right and bottom left of the bottom-left and bottom-right matrices.

In order to visualise the structure of matrix A more clearly, let us consider Figure 3.1. Each small block of which there are $2(n+1) \times 2(n+1)$, represents an $(n+1) \times (n+1)$ matrix. The different colours correspond to positions where the coefficients of different finite difference approximations are located. For example, all terms representing z-derivatives are included in the

red boxes. While terms containing second-order derivatives with respect to x will be contained in the green fringe blocks as well as the main diagonal red blocks. Fourth-order x-derivatives have entries in the fringe blocks (green and orange) as well as the main diagonal red blocks. Note that the coefficients related to mixed derivatives are located in the fringe blocks as well as the main diagonal blocks. Each light blue block matrix represents an empty matrix. The entire top-left matrix is zero since $\partial b/\partial t$ has no dependence on b itself in Equation (3.9).

3.1.6 Sparse matrices

The calculations performed when multiplying the matrix A by the column vector consists of performing many trivial calculations, i.e., multiplying by zero many times. Multiplying by zero is as trivial for human beings as it is for computers. The time it takes to perform this calculation, however, is non-zero. In the absence of an efficient method to handle multiplication by zero, we find our simulation can spend an inordinate amount of time on trivial calculations. For example, if we take 100 points in both the x and z directions, our large matrix A contains 20000×20000 entries. We process by multiplying this matrix by a column vector with 20000 entries. For each time step this matrix multiplication occurs 4 times, a total of $4 \times 20000^3 = 3.2 \times 10^{13}$ calculations per time step. When considering second-order finite difference approximations, the approximate number of calculations involved in calculating a single time step that is non-zero is $4 \times 380000 = 1.52 \times 10^6$, meaning approximately 4.75×10^{-6} % of all calculations are non-trivial. Moreover, with increasing resolution, a greater proportion of the elements in the matrix A become zero, leading to a reduced percentage of all computations being non-trivial.

At this point, we can leverage the sparsity of matrix A to our advantage. We adopt the inbuilt routine for constructing sparse matrices in Python which represents non-zero entries in a coordinate system. Rather than assigning every entry to a matrix including all zero entries, we assign only the non-zero elements and their corresponding coordinates, i.e., its row and column position within the matrix.

In order to construct a matrix corresponding to the term $\partial^2 b/\partial z^2$ we need to employ the finite difference approximation given by Equation (3.12). It is evident that the associated matrix corresponds to the red blocks of the bottom-left sub-matrix in Figure 3.1. It prescribes a tridiagonal system where every other entry is zero. The coefficients of this tridiagonal matrix will be

$\frac{1}{(\Delta z)^2}(1,-2,1)$ assuming we move left to right within the matrix. A non-sparse representation of this matrix using periodic boundary conditions in z looks like

$$\frac{1}{(\Delta z)^2}\begin{bmatrix} -2 & 1 & 0 & 0 & \dots & 1 \\ 1 & -2 & 1 & 0 & 0 & \dots \\ 0 & 1 & -2 & 1 & 0 & \dots \\ \vdots & & & & & \ddots \\ 0 & \dots & 0 & 1 & -2 & 1 \\ 1 & \dots & 0 & 0 & 1 & -2 \end{bmatrix} \tag{3.19}$$

To build a sparse matrix we only have to specify the data at each point where there is a non-zero entry. We can do this in the following way in Python

```
# Import relevant modules
import numpy as np
import scipy.sparse as sps
from scipy.sparse import csc_matrix

def dz(n,zmax):
    # Set dz to be the spatial resolution in the z-direction
    return zmax/(n+1)

def matrix_contructor_d2bdz2(n,zmax):
    # Set the column and row coordinates for the diagonal entries
    col_Diag = np.linspace(0,n,n+1)
    row_Diag = np.linspace(0,n,n+1)

    # Set the data for these entries to correspond to the coefficients used in the finite difference approximation
    data_Diag =
     -2*(1/dz(n,zmax)**2)*np.linspace(1,1,n+1)
    matrix_inter_Diag =
    csc_matrix((data_Diag, (row_Diag, col_Diag)),
                shape = (n+1, n+1))

    # Set the column and row coordinates for the off-diagonal entries to the left
    col_Left = np.linspace(0,n,n+1)
    row_Left = np.linspace(1,n+1,n+1)%(n+1) # To remove periodic boundary conditions in z, replace 'np.linspace(1,n+1,n+1)%(n+1)' in favour of 'np.linspace(1,n,n)' noting that col_Left must change to reflect this also
    data_Left = (1/dz(n,zmax)**2)*np.linspace(1,1,n+1)
    matrix_inter_Left =
    csc_matrix((data_Left, (row_Left, col_Left)),
                shape = (n+1, n+1))

    # Set the column and row coordinates for the off diagonal entries to the right
    col_Right = np.linspace(1,n+1,n+1)%(n+1)
```

```
32      row_Right = np.linspace(0,n,n+1)
33      data_Right = (1/dz(n,zmax)**2)*np.linspace(1,1,n+1)
34      matrix_inter_Right =
35      csc_matrix((data_Right,(row_Right,col_Right)),
36                 shape=(n+1,n+1))
37
38      # Sum these three matrices together to make the tridiagonal
        matrix
39      matrix = matrix_inter_Diag + matrix_inter_Left
40               + matrix_inter_Right
41
42      return matrix
```

Listing 3.1: Example section of the code used to construct an individual sparse matrix representing a second-order derivative with respect to z.

Calling this function returns a sparse tridiagonal matrix that uses periodic boundary conditions in z. As far as the computer memory is concerned, the size of the sparse matrix also remains the same no matter the dimension, whereas the memory requirements scale with resolution for a non-sparse representation of a matrix. For example for $n = 100$, a sparse matrix takes up 48 bytes of memory while a non-sparse matrix takes up approximately 81728 bytes. To calculate the total memory requirement of matrix A, we simply multiply the memory by the dimensions of the matrix (since zeros require the same memory as any other value). The total memory is $81728 \times 200 \times 200 = 3269120000$ bytes or approximately 3 Gigabytes, whereas the total memory required for matrix A constructed in sparse form is approximately $1800 \times 48 = 86400$ or 86.4 Kilobytes. All of these steps considered result in an enormous improvement in performance.

It is difficult to compare the exact difference in efficiency of simulations run using the sparse matrix representation versus the non-sparse representation. Large scale comparisons are not feasible due to the size of the non-sparse matrix A. An enhanced resolution increases the ratio of the number of calculations for sparse matrices compared to non-sparse matrices increases. This leads to a notable underestimation of performance enhancement when evaluating comparisons at low resolutions. However, one could estimate that it is proportional to the reduction in the number of calculations which is over seven orders of magnitude difference.

3.2 Initial conditions

To solve our system of differential equations, we need to establish a starting point defined as a set of initial conditions. Initial conditions serve as the

anchor from which the dynamical evolution of the system unfolds. We begin our investigation by exciting Alfvén waves at the base of our domain in a sinusoidal fashion. In this case, we consider an initially unperturbed system of magnetic field lines. That is, we consider

$$\begin{aligned} b(x,z,0) &= 0, \\ U(x,z,0) &= 0. \end{aligned} \tag{3.20}$$

We then excite Alfvén waves at the base of our domain through a boundary condition at $z = 0$. In the case of Hood et al. (2002), the authors considered a pulse driver, which was not time dependent. In their case they prescribed the shape of the pulse as their initial condition, more details are provided in Section 3.5.2.

3.3 Boundary conditions

The perturbations of our magnetic field lines generate sinusoidal Alfvén waves. Mathematical details of the sinusoidal driver and the second boundary condition (based on D'Alembert's solution) are shown below

$$\begin{aligned} b(x,0,t) &= Csin(\omega t), \\ U(x,z,t) &= \frac{\partial b}{\partial t} = -v_A(x)\frac{\partial b}{\partial z}, \end{aligned} \tag{3.21}$$

where C represents the amplitude of the driver. These conditions ensure that the wave is driven at the base of the domain (at $z = 0$) and propagates at its local Alfvén speed, varying from field line to field line for an inhomogeneous plasma. Clearly, the perturbation given by b is invariant of x, meaning that the frequency of the driver is constant in our simulation. The wavelength varies due to the inhomogeneous Alfvén speed. The driver is also invariant of z, since waves are excited only at $z = 0$. As the wave propagates along the magnetic field line, the column vectors representing the solution of our problem are updated and hence the perturbation varies in x and z for all $t > 0$, as the simulation evolves. It is perfectly feasible to allow the frequency to vary as a function of x, however, for the present study, this aspect is not considered.

In later chapters, we discuss the effects of a broadband driver. Numerically, this is achieved by summing together multiple harmonic drivers of varying frequencies. The boundary conditions in the case of N harmonic drivers appear as

$$
\begin{aligned}
b(x,0,t) &= \sum_{i=1}^{N} A_i sin(\omega_i t), \\
U(x,z,t) &= \frac{\partial b}{\partial t} = -v_A(x)\frac{\partial b}{\partial z}.
\end{aligned}
\tag{3.22}
$$

It is possible to vary the amplitude of the components of the broadband driver as required by multiplying each $b(x,0,t)$ by some user-defined constant, A_i.

When perturbing an equilibrium, the wave equation inherently allows for the existence of two waves propagating in opposite directions. For precise modelling of the phase mixed Alfvén waves, particularly in an open field geometry, it is imperative to prevent interference between these counter-propagating waves. This ensures that the solution remains consistent across different numerical configurations, including domain size and variations in boundary conditions.

Depending on the chosen driver, certain boundary conditions may become more suitable or applicable. Consider the case of a finite lifetime driven pulse, as considered by Hood et al. (2002). In a static background, one can employ periodic boundary conditions in the z direction to allow for a larger effective domain. The wave may propagate *around* the domain while allowing for higher resolution numerically by having a smaller domain in z. In contrast, in the case of the continuously excited wave driver, this is not applicable. As soon as the perturbation reaches the end of the domain, it begins to interfere with the base driver.

One also has to consider the interference of the two waves propagating antiparallel to one another, naturally emitted by a second-order wave equation. When using periodic boundary conditions, this effectively halves the usable domain, since each wave propagates towards one another with a relative speed of twice the Alfvén speed. Instead, adopting a fixed boundary condition at the base of the domain, removes the backward propagating wave usually permitted by the wave equation, resulting in all wave energy travelling unidirectionally. In order to investigate whether this affects the behaviour of our waves, we conducted simulations for both periodic boundary conditions and fixed boundary conditions. We terminated the simulation before the counter-propagating waves (in the case of periodic boundary conditions) interfered with one another. We found that the initial perturbation (leading wavefront) differs depending on the boundary condition, however, the wave propagating in its

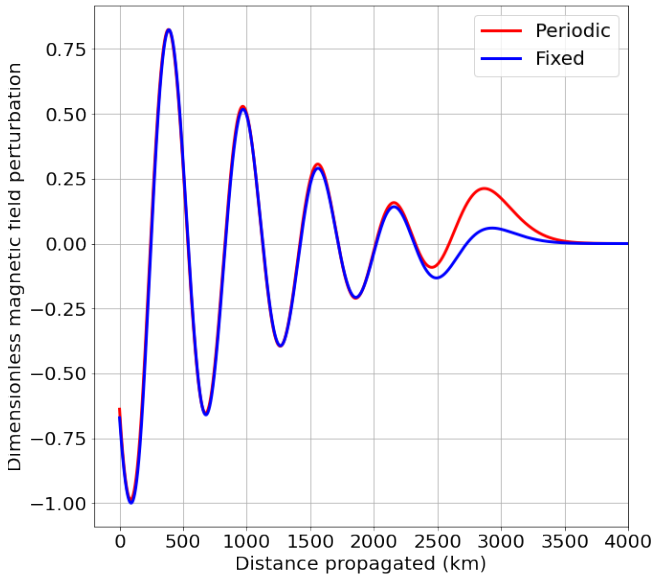

Figure 3.2: Two profiles of phase mixed Alfvén waves excited under identical plasma configurations are plotted employing either periodic or fixed boundary conditions at the base of the numerical domain.

wake displays consistent behaviour. This conclusion is displayed in Figure 3.2 considering a single simulation representative of our various tests.

We consider the behavior of the waves to be sufficiently invariant on the boundary conditions once our simulations reach a steady state or when the wave has propagated far enough for the initial perturbation effects to become negligible. Hence, we adopt a fixed boundary condition at the base of the domain to allow for a smaller domain resulting in higher relative resolution and code efficiency. Simulations modelling continuously driven waves must still be terminated before the perturbation reaches the end of the z-domain, due to wave reflection occurring (for a fixed boundary) or interference at the base of the domain (for a periodic boundary). This means that the boundary conditions for a continuous driver at $z = z_{max}$, where z_{max} denotes the end of the domain, do not matter, since the perturbation never achieves this distance.

We employ periodic boundary conditions in x. This was chosen to ensure that magnetic field lines at either end of the domain were not undergoing significantly different behaviour due to a numerical phase mixing effect occurring. The only condition this imposes is on the density profile and is given by

$$\rho(x = x_{min} = 0) = \rho(x = x_{max} = 1). \tag{3.23}$$

Figure 3.1 represents the larger matrix structure when periodic boundary conditions are considered in x. To implement periodic boundary conditions in z, we must vary the way we construct the individual block matrices, hence Figure 3.1 does not display the boundary conditions used for the z domain. An example of a matrix with periodic boundary conditions in z can be seen earlier in Equation (3.19), and the concept applies to other derivatives.

3.4 Courant–Friedrichs–Lewy condition

When employing the RK4 time-stepping algorithm, it is crucial to choose an appropriate time step. A time step that is too large can lead to instabilities in the solution, while a time step that is too small can result in excessively long simulation times. The convergence condition, first proposed by Courant et al. (1928), commonly known as the CFL condition, provides an upper limit for the time step to ensure stable solutions. The CFL condition states that our time step, denoted by h in Equation 3.3, must satisfy the following condition

$$h \leq \Delta z / max(v_A). \tag{3.24}$$

For time-dependent drivers, we define the period of the wave in terms of the number of time steps it takes to produce one full period. We wish to conduct a parameter study where we control the wavelength and since the speed of the wave and time it takes for one complete period dictate the wavelength, it is useful to pick this value to be a rounded decimal, such as 0.005 rather than 0.0052162..., and hence, we select a value close to, but below, this upper limit. This approach allows for direct control over the wavelength of the generated Alfvén waves.

For time-dependent drivers, we express the wave period in terms of the number of time steps required to produce one full cycle. To conduct a parameter study where we control the wavelength, it is useful to choose a rounded decimal value, such as 0.005, rather than a number like 0.0052162. This is because the combination of the wave speed and the period determine the wavelength. Therefore selecting a rounded value close to, but below, the upper limit ensures direct control over the wavelength of the generated Alfvén waves.

In addition, we take the largest value of our Alfvén speed (for the inhomogeneous cases, this is always 1.5, and this value is also chosen in the case of the homogeneous simulations for consistency) so that our chosen time step

provides a stable solution across all field lines, irrespective of their relative speed.

3.5 Validation and testing

Whenever a numerical code is constructed, the first question we must ask is *how can we validate our results?* To gain insight into the efficacy of our code it is instructive to numerically solve equations for which analytic solutions are available. For that reason, we begin this process by solving the undamped wave equation numerically, which can be compared with the analytical solution given by D'Alembert. This is an important step in solving Equation (2.55) as it allows us to define a suitable resolution that does not result in large numerical dissipation which occurs as a result of compounding truncation errors arising from the finite spacing between grid points and the finite time step size. As the equation we are solving does not include any dissipation, D'Alembert's solution of the homogeneous wave equation tells us that the amplitude of a wave should remain constant. The undamped wave equation is defined as

$$\frac{\partial^2 b}{\partial t^2} = v_A^2 \frac{\partial^2 b}{\partial z^2}, \tag{3.25}$$

where v_A is the speed of propagation, In this case, we choose this notation to align with the Alfvén speed, however, it is common to see this value replaced with c. In this case, chosen to be constant. Equation (3.25) has analytic solutions $f(z - v_A t) + g(z + v_A t)$, i.e., two waves traveling anti-parallel to one another at a speed v_A.

After carrying out multiple simulations of varying resolution, the observed numerical dissipation led to a reduction in amplitude of much less than 1% of the initial amplitude for a resolution of 100 points in the x and z directions. We allowed for 10 periods of the wave to propagate before terminating the resolution tests. We anticipate that when modelling Alfvén waves in the presence of the dissipative mechanisms discussed in Chapter 2, the amplitude will damp by a factor of e times (approximately 70 %) over a distance comparable to the height of the chromosphere, or approximately 6 wavelengths (for a wavelength of 400 km), making this level of numerical dissipation entirely acceptable. The challenge with numerical dissipation when addressing damped wave equations is its resemblance to physical diffusion, it is impossible to reverse engineer the solution to explain what proportion of dissipation occurs due to numerical dissipation or physical dissipation. Therefore, it is crucial to introduce each

dissipative term with care, as each new term inherently increases the numerical diffusion.

3.5.1 Numerical solution of the damped wave equation

Introducing damping terms into Equation (3.25) allows, to some extent, a comparison between the damping due to a physical dissipative process and the numerical dissipation. A typical wave equation with a damping term takes the form

$$\frac{\partial^2 b}{\partial t^2} = v_A^2 \frac{\partial^2 b}{\partial z^2} + \eta \frac{\partial^2}{\partial z^2} \frac{\partial b}{\partial t}, \tag{3.26}$$

where all coefficients are constant. A direct comparison cannot be wholly made, since introducing a new term, inherently introduces additional numerical dissipation due to additional truncation errors involved in the damping term. However, carrying out simulations, varying the value of η, enables quantification of these errors.

Slowly increasing the value of η, allows us to calculate certain parameter ranges in which dissipation due to the considered dissipation is dominant over numerical dissipation. If the constant η is identified with the coefficients of Ohmic diffusion, the lower bound of these ranges falls many orders of magnitude lower than the typical values of the various diffusive quantities found in the lower solar atmosphere, hence we can be sure that the dissipation observed in our simulations occurs due to the physical properties of the simulated plasma.

3.5.2 Validation by reproducing known results

We were also partially able to validate the part of our code that corresponds to phase mixing by investigating solutions of Equation (3.27) given by

$$\frac{\partial^2 b}{\partial t^2} = v_A^2(x) \frac{\partial^2 b}{\partial z^2} + \eta \frac{\partial^2}{\partial x^2} \frac{\partial b}{\partial t}, \tag{3.27}$$

the equation solved by Hood et al. (2002) in their investigation into phase mixed Alfvén pulses. By reproducing the results obtained by Hood et al. (2002) for the phase mixing of Alfvén waves generated by individual and bipolar pulses, we were able to gain further confidence in our numerical model. The resolutions of the two simulations may differ, leading to increased or reduced numerical damping, however, we assume this effect to be negligible, based on the previous test concerning the undamped wave equation. The study by Hood et al. (2002) considers a dimensionless Ohmic diffusion coefficient of 5×10^{-4}. In

the context of coronal holes (the subject of investigation of Hood et al., 2002) one might expect a typical Alfvén speed of 500 kms^{-1} and a typical length scale of 100 Mm, implying a dimensional value of $\eta = 2.5 \times 10^{10}$ m^2s^{-1}, which is clearly many orders of magnitude larger than established formulae predict ($\eta \approx 1$ m^2s^{-1}). As previously mentioned, very often turbulence is invoked to inflate the values of this dissipative coefficient. Turbulence could potentially produce length scales small enough such that a dimensionless diffusion value given by Hood et al. (2002) is achieved, however, it is not clear if this was done here. It was rather unclear what values for L and v_{A0} were used in the simulations in their paper, which is a requirement in order to convert back to a dimensional result. However, irrespective of these values we were able to produce similar behaviour, and were able to highlight the effects of phase mixing on damping Alfvén pulses while validating our codes' ability to solve Equation (3.27). In order to solve this equation, we are required to prescribe initial conditions, and these profiles take the form

$$b(x, z, t = 0) = \begin{cases} 1 + \cos\left(10\pi(z - \frac{1}{10})\right), & \text{if } 0 < z < \frac{2}{10}, \\ 0, & \text{elsewhere,} \end{cases} \tag{3.28}$$

with the second initial condition for $U = \partial b/\partial t$ given by

$$U(x, z, t = 0) = \begin{cases} 10\pi v_A(x) \sin\left(10\pi(z - \frac{1}{10})\right), & \text{if } 0 < z < \frac{2}{10}, \\ 0, & \text{elsewhere,} \end{cases} \tag{3.29}$$

which is based on D'Alembert's solution. The last user-defined input required is an Alfvén speed profile, which is given by

$$v_A(x) = 1 + 0.5\cos(2\pi x). \tag{3.30}$$

To simulate the evolution of this pulse-generated Alfvén wave, subject to phase mixing, we follow the steps detailed previously in this chapter. We begin by non-dimensionalising each of the terms in Equation (3.27) using Equation (3.11), omitting bars for convenience. The dimensionless form of Equation (3.27) remains unchanged. Next, we rewrite the dimensionless governing equation as a system of two coupled first-order PDEs. Implementing the finite difference formulae given by Equations (3.12)–(3.13) to replace the spatial derivatives, allows us to construct a large matrix whose entries are populated by the coefficients of the finite difference approximations. We then construct the column vectors consisting of the initial conditions given by Equations (3.28)–(3.29). The coefficients for the RK4 time-stepping scheme are computed by

matrix-vector multiplication, with subsequent summation and averaging yielding the solution of the governing equation at the next time step. Iterative computation of subsequent time steps proceeds for a predetermined duration, allowing for the exploration of phase-mixed pulse behavior in time. An illustrative result from a simulation depicting an individual pulse at distinct time intervals is presented in Figure 3.3. We consider the Alfvén pulse propagating along the magnetic field line that corresponds to the location of the steepest gradient in Alfvén speed. Notably, we refrain from imposing any specific physical length scale to avoid speculation regarding the chosen parameterisation for η. This prohibits the conversion to dimensional form, however, this is not strictly necessary for code validation.

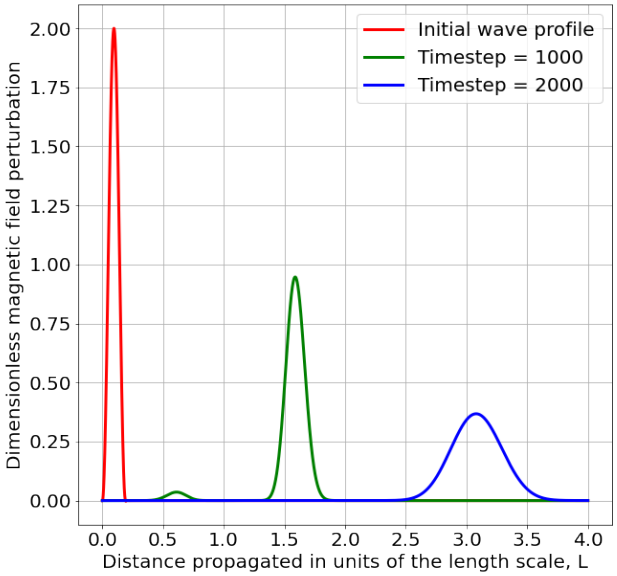

Figure 3.3: Evolution of a phase-mixed pulse at simulation time steps $t = 0$, $t = 1000$, and $t = 2000$. Each profile is represented by a distinct color line, illustrating the attenuation of the pulse over time.

It is clear that phase mixing causes a longitudinal stretching of the pulses profile due to the inhomogeneous Alfvén speed. For the wave propagating along the magnetic field line presented above, neighbouring waves are propagating both faster and slower than this wave. Due to the magnetic tension forces acting between neighbouring field lines, this varying behaviour causes the leading edge of the pulse to be pulled along and the trailing edge to be pulled back, subsequently leading to this stretching behaviour of the profile with propagation. Due to the nature of the initial condition given by Equation (3.29),

not all of the pulse propagates in the positive z direction. A small component proportional to the magnitude of the dissipative coefficient, η, propagates in the negative z direction. This is evident in the small bump in the green line for time step $t = 1000$. Due to the relative amplitudes of this counter-propagating wave, we consider the effects of these additional interactions to be negligible compared the the dissipation due to phase mixing. Note that periodic boundary conditions have been used in the x and z directions, where the z domain has been 'flattened out' and presented in Figure 3.3 as if it were a domain that ended at $z = 4$. This causes the position of the counter-propagating (small amplitude) wave in the solution for $t = 1000$ to be closer to the base of the domain than it should theoretically be, had we not used periodic boundary conditions in z.

A second profile was also investigated by Hood et al. (2002), termed as the bipolar pulse, whose form is given by

$$b(x, z, t = 0) = \begin{cases} 1 + \cos(10\pi(z - \frac{1}{10})), & \text{if } , 0 < z < \frac{2}{10} \\ -1 - \cos(10\pi(z - \frac{1}{10})), & \text{if } \frac{2}{10} < z < \frac{4}{10}, \\ 0, & \text{elsewhere,} \end{cases} \tag{3.31}$$

with a required initial condition for $U = \partial b/\partial t$ given by

$$U(x, z, t = 0) = \begin{cases} 10\pi v_A(x) \sin(10\pi(z - \frac{1}{10})), & \text{if } , 0 < z < \frac{2}{10} \\ -10\pi v_A(x) \sin(10\pi(z - \frac{1}{10})) & \text{if } \frac{2}{10} < z < \frac{4}{10}, \\ 0, & \text{elsewhere.} \end{cases} \tag{3.32}$$

Simulations were carried out in a similar manner as the individual pulse and Figure 3.4 presents a result obtained from a simulation modelling a bipolar pulse at multiple simulation time steps, given the same Alfvén speed profile and value for η as for the individual pulse and that of Hood et al. (2002).

Similar to the findings by Hood et al. (2002), we found that the amplitude of the bipolar pulse is reduced more effectively, since the positive and negative components of the pulse profile propagate into one another, effectively cancelling one another out, resulting in a greater reduction in amplitude evident at $t = 2000$. The amplitude of the backward propagating wave in the case of Hood et al. (2002) is relatively small since the dimensionless dissipative coefficient remained small. However, given typical length and velocity scales relevant to the chromosphere, the dimensionless ambipolar diffusive coefficient results in a backward propagating wave that is comparable to the amplitude of the forward propagating perturbation, hence destroying any assumed initial profile.

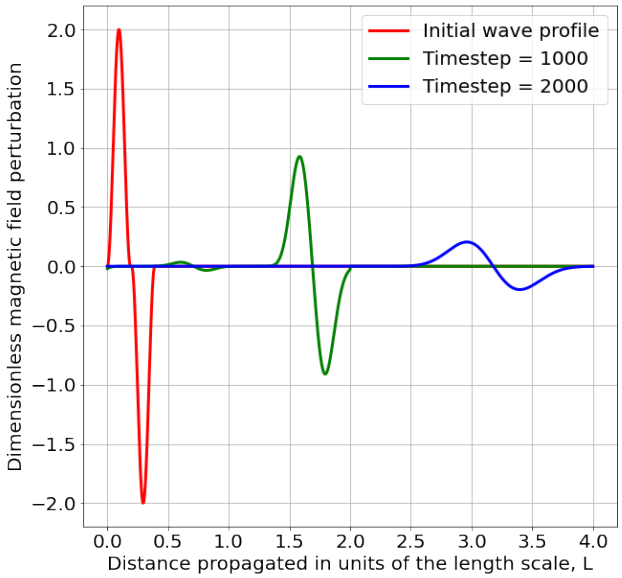

Figure 3.4: Evolution of a phase-mixed bipolar pulse at simulation time steps $t = 0$, $t = 1000$, and $t = 2000$. Each profile is represented by a distinct color line, illustrating the attenuation of the pulse over time.

3.6 Numerical background for the problem of Alfvén wave phase mixing in a two-fluid approximation

Many of the numerical methods previously described in this chapter are applicable to a two-fluid approach. In this section, we discuss the various subtleties and variations required in considering a two-fluid approach to investigate the effects of phase mixing on the damping of Alfvén waves in partially ionised plasmas.

When solving a second-order PDE, our numerical solver performed many large matrix-vector multiplications. The matrix had a substructure of 2×2 large matrices consisting of many smaller sub-matrices each representing operations on a single magnetic field line or the change of this magnetic field line in time, U. The off-diagonal block matrices captured the cross-field interactions occurring due to phase mixing.

When solving a governing equation modelling propagating Alfvén waves in a partially ionised two-fluid plasma, we are required to solve a third-order

PDE. Once again, we write all quantities in dimensionless form as

$$\begin{gathered}\bar{x}=\frac{x}{L}, \quad \bar{z}=\frac{z}{L}, \quad \bar{v}_A=\frac{v_A}{v_{A0}}, \quad \bar{t}=\frac{t v_{A0}}{L}, \\ \bar{\zeta}_i=\frac{\zeta_i}{L v_{A0}}, \quad \bar{\zeta}_n=\frac{\zeta_n}{L v_{A0}}, \quad \text{and} \quad \bar{\tilde{\nu}}_{in}=\frac{\tilde{\nu}_{in} L}{v_{A0}}.\end{gathered} \tag{3.33}$$

where, as before, L is the length scale of the problem (significantly smaller than that of the single-fluid model), $v_{A0} = B_0/\sqrt{\mu_0 \rho_{0i}}$ is the typical Alfvén speed (with only ions being attached to the magnetic field lines), where ρ_{i0} is the typical ion density. The form of the equation remains unchanged and bars are subsequently dropped for convenience. We then reduce the governing equation to a system of three first-order differential equations as

$$\frac{\partial v_i}{\partial t} = U, \tag{3.34}$$

$$\frac{\partial U}{\partial t} = W, \tag{3.35}$$

$$\begin{aligned}\frac{\partial W}{\partial t} = {} & v_A^2(x)\frac{\partial^2 U}{\partial z^2} - \tilde{\nu}_{in}(x) W(\chi+1) + \tilde{\nu}_{in}(x) v_A^2(x)\chi\frac{\partial^2 v_i}{\partial z^2} + \tilde{\nu}_{in}(x)\zeta_i\chi\nabla^2 U + \\ & \tilde{\nu}_{in}(x)\zeta_n\nabla^2\left(\frac{1}{\tilde{\nu}_{in}(x)}\left\{W - v_A^2(x)\frac{\partial^2 v_i}{\partial z^2} - \zeta_i\nabla^2 U + \tilde{\nu}_{in}(x) U\right\}\right) \\ & + \zeta_i\nabla^2 W.\end{aligned} \tag{3.36}$$

Next, the spatial derivatives are rewritten using finite difference approximations, enabling our system of equations to be represented as a single matrix multiplied by a column vector of the form

$$\frac{\partial}{\partial t}\begin{bmatrix} v_i \\ U \\ W \end{bmatrix} = A \begin{bmatrix} v_i \\ U \\ W \end{bmatrix}. \tag{3.37}$$

As discussed earlier, the matrix representation is sparse. For this reason, sparse matrices are once again employed where the general structure of the matrix is shown in Figure 3.5, with all blue boxes representing a matrix consisting entirely of zeros.

When considering a sinusoidal wave driver at the base of the domain, the boundary conditions are given by

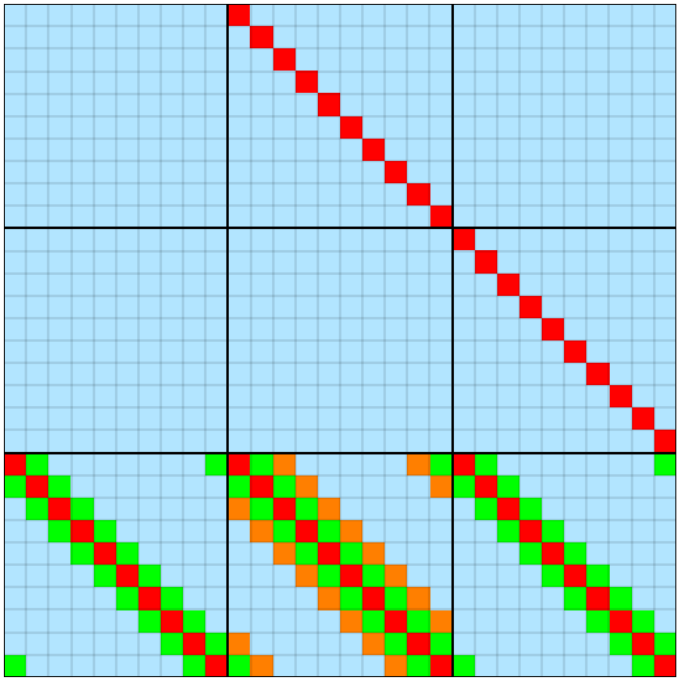

Figure 3.5: Matrix A with dimensions $3(n+1)^2 \times 3(n+1)^2$ consisting of nine large matrices (denoted by top-left, top-middle, top-right, middle-left, middle-middle, middle-right bottom-left, bottom-middle and bottom-right) populated by small matrix blocks with dimensions $(n+1) \times (n+1)$. The blue-coloured blocks consist entirely of zeros, while the other coloured blocks are populated by the coefficients of finite difference approximations. Note that here we use periodic boundary conditions in x, exemplified by the matrix blocks in the top right and bottom left of the bottom row of the larger matrices.

$$
\begin{aligned}
v_i(x,0,t) &= sin(\omega t),\\
U(x,0,t) &= \omega cos(\omega t),\\
W(x,0,t) &= -\omega^2 sin(\omega t),
\end{aligned}
\tag{3.38}
$$

where the potential for a broadband driver is feasible in a manner akin to the approach taken in Equation (3.22). We initially consider our field lines to be unperturbed and hence the initial conditions for v, U and W are all set to zero. While the physics we investigate by studying waves from a two-fluid perspective differs considerably from the assumptions made when modelling in the single-fluid MHD framework, numerically the primary distinction lies in the length scales and wave frequency. The code's utilisation of dimensionless parameters accommodates these differences seamlessly. In the next chapters, we present the results obtained from implementing the solvers detailed above.

CHAPTER 4

Phase mixing of Alfvén waves in single-fluid plasmas

[1]The key distinction between phase mixing in a fully and partially ionised plasma resides in the nature and magnitude of dissipative processes that are involved in the description of wave damping. As presented in the previous chapters, one particular dissipative process that is relevant to the mixture of charged and neutral plasma is ambipolar diffusion which owes its existence to the presence of neutrals and the collisions of charged particles with neutrals. Secondly, the presence of neutrals modifies the magnitude of the "traditional" dissipative effects, such as viscosity and Ohmic diffusion. Compared to the case of a fully ionised plasma, these coefficients are enhanced by several orders of magnitude thanks to the increased rate of collisions in a partially ionised plasma. That is why, it is natural to expect that the efficiency of phase mixing (although the physical process is the same) with regard to the damping of waves will also be enhanced in a partially ionised plasma. The variation of height of the dissipative coefficients that are relevant for partially ionised plasma over the height of 3 Mm above the solar surface is shown in Figure 4.1, where now the magnetic field was taken to vary with height according to $B_0 = 1000e^{-H/660}$, expressed in Gauss, where H represents the height above the solar surface in kilometers (Vranjes and Krstic, 2013). The values of the physical parameters (temperature, and number densities of species) needed to calculate these coefficients were taken from the AL C7 solar atmospheric model (Avrett and Loeser, 2008)

In this chapter we are going to review parts of the current state-of-the-art in phase mixing in fully ionised plasma, discussing some of the simplifying assumptions made by the original investigation by Heyvaerts and Priest (1983). When applying the same simplifications to a partially ionised plasma, the

[1]The content of this chapter is based on the publication McMurdo et al. (2023).

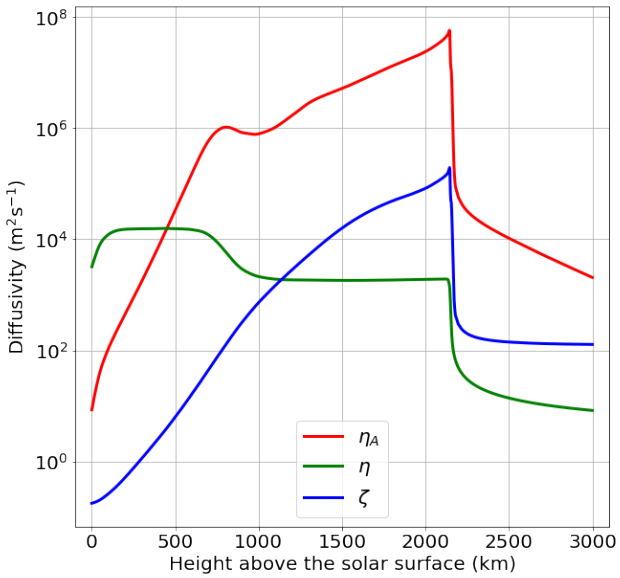

Figure 4.1: The variation of the ionisation degree with height (black line) together with the variation of the Ohmic diffusion (green line), Ambipolar diffusion (red line) and shear viscosity (blue line). These transport coefficients were calculated taking into account the values of the physical parameters given by the AL C7 model (Avrett and Loeser, 2008).

obtained solutions will be classified as the "weak" solution, while the consideration of all aspects related to the chromospheric partially ionised plasma environment will constitute the "strong" solution.

Before we continue, there are certain assumptions needed to be satisfied in order for the fluid to be appropriately defined as a fluid. In the single fluid regime, all collisional frequencies of particles with one another and with themselves must be larger than the frequencies of the waves we choose to model. That is, all collisional frequencies, ν_{ab} for all $a, b \in \{e, i, n\}$ with a and b allowed to be equal, must exceed the frequency of the wave. Studying figure 2.2, and calculating values for the ion-ion, electron-electron and neutral-neutral collisional frequencies, we find that neutral-neutral collisions are the most infrequent, closely followed by ion-neutral collisions. For a quasi neutral plasma, electron-electron collisions, electron-ion and ion-ion collisions differ only by a constant factor coming from the definitions of each collisional frequency. The neutral-neutral collisional frequency closely aligns with the ion-neutral collisional frequency, differing only by the ratio between the collisional cross section values. For the ionisation degrees we study, the collisional frequencies all far exceed those of the simulated wave frequencies (taking a maximum value of 133 mHz), hence a single fluid regime is perfectly valid. Further details of the implications of this result on the two-fluid simulations will be provided in Chapter 6.

4.1 Phase mixing in a fully ionised plasma

Before we investigate the damping of Alfvén waves in a partially ionised plasma, it is instructive to begin by setting a base marker to compare the damping lengths of Alfvén waves due to phase mixing in a fully ionised plasma with those of a partially ionised plasma. Although there are similarities in governing equations, upon close inspection, there are stark differences. Firstly, η_C is now replaced with η since the Cowling diffusion coefficient is now set to zero. Retaining all terms including products of dissipative coefficients the governing equation for phase mixed Alfvén waves in a fully ionised plasma is given by

$$\begin{aligned}\frac{\partial^2 b}{\partial t^2} = v_A^2(x)\frac{\partial^2 b}{\partial z^2} + \left[(\eta+\zeta)\frac{\partial^2}{\partial x^2} + (\eta+\zeta)\frac{\partial^2}{\partial z^2}\right]\frac{\partial b}{\partial t} \\ - \zeta\left[\eta\frac{\partial^2}{\partial x^2} + \eta\frac{\partial^2}{\partial z^2}\right]\nabla^2 b.\end{aligned} \tag{4.1}$$

Note that the form has been given to allow direct comparison between Equation (2.55), factorisation of the derivatives would usually be used.

Since dissipative coefficients are very small in a fully ionised plasma, due to the high temperature and high Reynolds number i.e., low density and hence low collisional frequencies, the terms corresponding to products of dissipative coefficients are typically neglected. Furthermore, due to the presence of an inhomogeneous Alfvén speed, phase mixing creates large transversal gradients, much larger than the longitudinal gradients corresponding to the wavelength of the wave, so, it is assumed that $\partial/\partial x \gg \partial/\partial z$. This can be represented as the strong phase mixing limit given by

$$\frac{z}{k_\parallel}\frac{dk_\parallel}{dx} \gg 1, \tag{4.2}$$

which assumes that the cross-field variation in wavelengths is large compared to the ratio of wavelength over the longitudinal scale length of the problem. This allows for steep gradients in the Alfvén speed to be taken when calculating the damping lengths of phase mixed Alfvén waves.

Since the dissipative coefficients that multiply the x and z derivatives take the same value for Equation (4.1), Equation (4.2) allows us to neglect the z derivative in favour of the x derivative. Equation (4.1) therefore reduces to

$$\frac{\partial^2 b}{\partial t^2} = v_A^2(x)\frac{\partial^2 b}{\partial z^2} + (\eta+\zeta)\frac{\partial^2}{\partial x^2}\frac{\partial b}{\partial t}, \tag{4.3}$$

which resembles the typical form (seen in literature) of the governing equation used to model phase mixed Alfvén waves in a fully ionised solar plasma. Following the methodology employed by Heyvaerts and Priest (1983), we assume that b can be written as $b(x,z,t) = \hat{b}(x,z)\exp\{i(\omega t - k_\parallel(x)z)\}$, where $\hat{b}(x,z)$ represents the amplitude of the wave and $k_\parallel$ is the parallel wavenumber along the magnetic field. This allows us to find an equation for $\hat{b}(x,z)$ given by

$$\begin{aligned}(\omega^2 - k_\parallel^2(x)v_A^2(x))\hat{b} = v_A^2(x)\left[\frac{\partial^2\hat{b}}{\partial z^2} - 2ik_\parallel(x)\frac{\partial\hat{b}}{\partial z}\right] + \\ + i\omega(\eta+\zeta)\left[\frac{\partial^2\hat{b}}{\partial x^2} - i\frac{d^2k_\parallel}{dx^2}\hat{b} - 2iz\frac{dk_\parallel}{dx}\frac{\partial\hat{b}}{\partial x} - z^2\left(\frac{dk_\parallel}{dx}\right)^2\hat{b}\right],\end{aligned} \tag{4.4}$$

where $k_\parallel(x) = \omega/v_A(x)$, hence the left-hand side of the above equation vanishes. Equation (4.4) can be simplified further under the weak damping approximation and the strong phase mixing limit. The weak damping approximation is given by

$$\frac{1}{k_\parallel}\frac{\partial \hat{b}}{\partial z} \ll 1, \tag{4.5}$$

and it implies that the amplitude of the magnetic field perturbation varies weakly with height compared to the wavelength, i.e., the wave takes at least a few wavelengths to damp. This assumption is valid so long as the dissipative coefficients ζ and η are small. Assuming that since $\hat{b}$ is complex and hence a rather regular function of x (we are unsure of the exact details of this assumption made in the study by Heyvaerts and Priest (1983), but choose to follow the same assumption in order to have a direct comparison between the fully ionised case studied and the partially ionised case studied later), Equation (4.4) reduces to

$$\frac{\partial \hat{b}}{\partial z} = -\frac{1}{2}\frac{k_\parallel(x)}{\omega} z^2 \left(\frac{dk_\parallel}{dx}\right)^2 (\eta + \zeta)\hat{b}, \tag{4.6}$$

which can be easily integrated with respect to z to give

$$\hat{b}(x,z) = \hat{b}(x,0)\exp\left\{-\left(\frac{z}{\Lambda_1}\right)^3\right\}, \tag{4.7}$$

where $\hat{b}(x,0)$ is the amplitude of the perturbation at $z = 0$ and the quantity Λ_1 is the damping length of Alfvén waves, given by

$$\Lambda_1 = k_\parallel^{-1}\left(\frac{6\omega}{(\eta+\zeta)\left(d\log k_\parallel/dx\right)^2}\right)^{\frac{1}{3}}. \tag{4.8}$$

This relation shows that the damping length for phase mixed Alfvén waves varies with the $R^{1/3}$, where R is the total (viscous and diffusive) Reynolds number. This result also highlights the major implication of transversal gradients in the damping of Alfvén waves, as in a homogeneous plasma the damping length of waves would be proportional to R.

In order to evidence the changes in the damping length of phase-mixed Alfvén waves in a fully ionised plasma we perform a simple investigation. For that purpose, we prescribe that the inhomogeneous Alfvén speed is given by one of the following three profiles

$$\begin{aligned}
P_2 &: v_A(x) = v_{A1}\left(1 + \frac{1}{2}\cos\left[\frac{2\pi}{l_{inh}}(x - 0.5l_{inh})\right]\right), \\
P_3 &: v_A(x) = v_{A1}\left(1 + \frac{1}{2}\tanh\left[\frac{x - 0.25l_{inh}}{0.1l_{inh}}\right]\right), \\
P_4 &: v_A(x) = v_{A1}\left(1 + \frac{1}{2}\tanh\left[\frac{x - 0.25l_{inh}}{0.03l_{inh}}\right]\right),
\end{aligned} \tag{4.9}$$

where l_{inh} is the length scale of the transversal inhomogeneity. Note that the notation P_1 has been reserved for later on in the investigation, used to describe the homogeneous Alfvén speed profile, this choice has been made for consistency of notation throughout this thesis. For illustration, we chose $v_{A1} = 500$ km s^{-1}, $l_{inh} = 300$ km, and the factor of one half in the above Alfvén speed profiles is chosen in such a way that the Alfvén speed varies by a factor of 3 across the inhomogeneity, ranging from $250 - 750$ km s^{-1}, typical of the fully ionised corona (McIntosh et al., 2011). The last two tanh profiles are reflected about the midpoint of the inhomogeneity to make them symmetric. The choice of these profiles was made to model the effectiveness of an increased local gradient in the Alfvén speed. The damping lengths are calculated by considering the wave propagating along the field line that corresponds to the location of the intersection of the three Alfvén speed profiles, which aligns with the location of the maximum gradient in Alfvén speed. Figure 4.2 shows these profiles in dimensionless form.

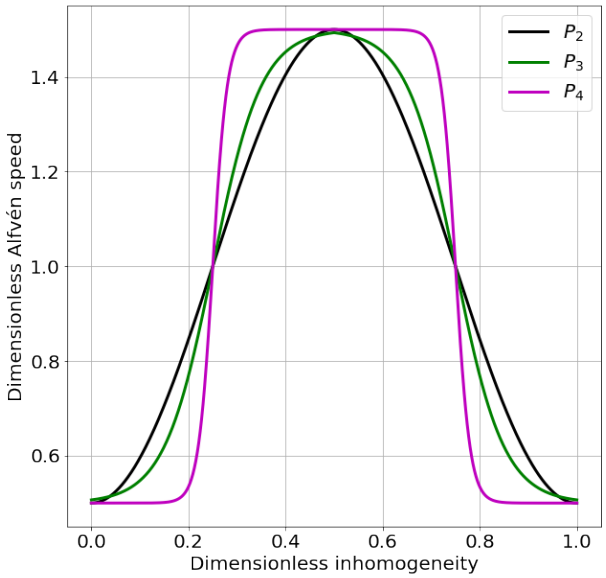

Figure 4.2: The different profiles of the Alfvén speeds used in the analysis of phase mixed Alfvén waves in a fully ionised plasma are shown by curves of different colors. Speeds and lengths are given in dimensionless units. The two tanh profiles are symmetric about the midpoint of the inhomogeneity in order to apply periodic boundary conditions to our numerical solver.

In order to gain an understanding of the damping lengths this model results in, let us assign some realistic quantities for coronal plasma. For temperatures

of the order of a million Kelvin, typical values for Ohmic diffusion and shear viscosity are of the order of 1 m^2s^{-1} (Ruderman and Petrukhin, 2018; Hood et al., 2002). Assuming that waves are driven at a typical frequency of 3 mHz, a dominant observed frequency in the corona (Aschwanden et al., 1999*b*), the calculations result in damping lengths that range from $2.4 \times 10^4 - 7.2 \times 10^4$ Mm (about 30% of the Sun-Earth distance), depending on the Alfvén speed profile considered. The steeper the profile, the shorter the damping length. This result clearly indicates the reason why earlier studies questioned the efficiency of phase mixing in the solar corona. In order to achieve the required heating in the solar corona, enhanced dissipative coefficients were assumed, with many orders of magnitude larger than predicted. If we were to enhance these dissipative coefficients by 7 orders of magnitude assumed in the previously discussed literature, the damping lengths reduce to $110 - 336$ Mm (for the same Alfvén speed profiles given by $P_4 - P_2$ respectively), of equal order to the typical length of a coronal loop.

We should note that the gradient in the Alfvén speed is not properly resolved here, due to an assumption made by Heyvaerts and Priest (1983) on the regularity of the amplitude of the wave. The damping rates are, therefore, underestimated, as was shown by Ireland and Priest (1997), who found that the energy initially at smaller length scales decays faster than the rate given by Heyvaerts and Priest (1983). This occurs since the plasma is more strongly dissipative at smaller length scales. The inclusion of the second-order derivative of the amplitude of the magnetic field perturbation also leads to smoother Alfvén wavefronts.

4.2 Phase-mixed Alfvén waves propagating in a partially ionised plasma: Weak solution

In order to define a proof of concept for the problem of phase-mixed Alfvén waves in a partially ionised plasma and investigate how the damping lengths are modified, we follow many of the same assumptions made in the study by Heyvaerts and Priest (1983). To distinguish these results from the ones found in the most general case (where these assumptions are neglected), we label these results as the "weak" solutions. While some of our assumptions may not be suitable for a partially ionised plasma, this will act as a rough guide to whether a full numerical investigation is warranted. In that respect, we are going to neglect products of dissipative coefficients, effectively assuming high

temperatures and hence a high Reynolds number, allowing analytical progress. Subsequently, Equation (2.55) reduces to

$$\frac{\partial^2 b}{\partial t^2} = v_A^2(x)\frac{\partial^2 b}{\partial z^2} + \left[(\eta+\zeta)\frac{\partial^2}{\partial x^2} + (\eta_C+\zeta)\frac{\partial^2}{\partial z^2}\right]\frac{\partial b}{\partial t}. \tag{4.10}$$

Let us now carry out Fourier analysis and assume that the magnetic field perturbation, b, can be written in the form $b(x,z,t) = \hat{b}(x,z)\exp\{i(\omega t - k_\parallel(x)z)\}$, where $\hat{b}(x,z)$ represents the amplitude of the wave and $k_\parallel$ is the parallel wavenumber along the magnetic field. This allows us to rewrite Equation (4.10) as

$$\begin{aligned} -\omega^2\hat{b} = v_A^2(x)&\left[\frac{\partial^2\hat{b}}{\partial z^2} - 2ik_\parallel(x)\frac{\partial\hat{b}}{\partial z} - k_\parallel^2(x)\hat{b}\right] + \\ &+ i\omega(\eta+\zeta)\left[\frac{\partial^2\hat{b}}{\partial x^2} - 2iz\frac{dk_\parallel}{dx}\frac{\partial\hat{b}}{\partial x} - iz\frac{d^2k_\parallel}{dx^2}\hat{b} - z^2\left(\frac{dk_\parallel}{dx}\right)^2\hat{b}\right] + \\ &+ i\omega(\eta_C+\zeta)\left[\frac{\partial^2\hat{b}}{\partial z^2} - 2ik_\parallel(x)\frac{\partial\hat{b}}{\partial z} - k_\parallel^2(x)\hat{b}\right]. \end{aligned} \tag{4.11}$$

Investigating the damping effects of phase mixing, we focus exclusively on solutions to the imaginary component of the Equation (4.11) given by

$$2\frac{\omega}{k_\parallel}\frac{\partial\hat{b}}{\partial z} = (\eta+\zeta)\left[\frac{\partial^2\hat{b}}{\partial x^2} + z^2\left(\frac{dk_\parallel}{dx}\right)^2\hat{b}\right] + (\eta_C+\zeta)\left[\frac{\partial^2\hat{b}}{\partial z^2} - k_\parallel^2\hat{b}\right]. \tag{4.12}$$

Following the method suggested by Heyvaerts and Priest (1983), we impose the condition that $\hat{b}(x,z)$ is a regular function such that we may neglect the second-order derivatives of $\hat{b}(x,z)$. We apply the weak damping approximation and the strong phase mixing limit and, as a result, the equation takes the form

$$\frac{\partial\hat{b}}{\partial z} = -\frac{1}{2}\left\{\frac{z^2k_\parallel}{\omega}(\eta+\zeta)\left(\frac{dk_\parallel}{dx}\right)^2 + \frac{k_\parallel^2}{\omega}(\eta_C+\zeta)\right\}\hat{b}. \tag{4.13}$$

After some straightforward calculations, it follows that the amplitude of the magnetic field perturbation can be written as

$$\hat{b}(x,z) = \hat{b}(x,0)\exp\left\{-\left(\frac{z}{\Lambda_1}\right)^3 - \left(\frac{z}{\Lambda_2}\right)\right\}, \tag{4.14}$$

where $\hat{b}(x,0)$ is the amplitude of the perturbation at $z=0$ and the quantities Λ_1 and Λ_2 are related to the waves' damping length. In the above expression the first term in the exponent recovers the results obtained by Heyvaerts and

Priest (1983), while the second term is attributed solely to the fact that the plasma is partially ionised. The expression of Λ_1 is given by Equation (4.8) and Λ_2 is given by

$$\Lambda_2 = \frac{2\omega}{k_\parallel^3(\eta_C + \zeta)}. \tag{4.15}$$

Hence, Alfvén waves will damp due to phase mixing such that the damping length is a superposition of the solution that has the same definition as the expression for the fully ionised case given by Heyvaerts and Priest (1983) (Λ_1), and a term that is due to the ambipolar diffusion (Λ_2). One very important aspect of these quantities is that only Λ_1 depends on the gradient of the Alfvén speed and the ionisation degree, while Λ_2 depends only on the ionisation degree, which then dictates the value of η_C. This qualitatively different behavior is due to the spatial derivatives associated with the dissipative coefficients. While the shear viscosity and the Ohmic diffusion coefficent are associated with the spatial derivative that are perpendicular to the direction of propagation, the Cowling diffusion is associated with derivatives parallel to the propagation of waves.

In order to evidence the changes in the damping length of phase-mixed Alfvén waves in a partially ionised plasma, we perform a simple numerical investigation. For that purpose, we prescribe the following four profiles for the Alfvén speed

$$\begin{aligned}
&P_1 : v_A(x) = v_{A1}, \\
&P_2 : v_A(x) = v_{A1}\left(1 + \frac{1}{2}\cos\left[\frac{2\pi}{l_{inh}}(x - 0.5l_{inh})\right]\right), \\
&P_3 : v_A(x) = v_{A1}\left(1 + \frac{1}{2}\tanh\left[\frac{x - 0.25l_{inh}}{0.1l_{inh}}\right]\right), \\
&P_4 : v_A(x) = v_{A1}\left(1 + \frac{1}{2}\tanh\left[\frac{x - 0.25l_{inh}}{0.03l_{inh}}\right]\right),
\end{aligned} \tag{4.16}$$

where l_{inh} is the length scale of the inhomogeneity. For illustration, we chose $v_{A1} = 20$ km s^{-1}, $l_{inh} = 300$ km, and the factor of one half is chosen in such a way that the Alfvén speed varies by a factor of 3 across the inhomogeneity, ranging from $10 - 30$ km s^{-1}. These values were taken from previous studies involving propagating Alfvén waves in an inhomogeneous partially ionised plasma in spicules and fibrils (see, e.g., He et al., 2009; Okamoto and De Pontieu, 2011; Bate et al., 2022; Gafeira et al., 2017; Jafarzadeh et al., 2017).

The choice of these profiles was made to model the effectiveness of an increased local gradient in the Alfvén speed. These four profiles are converted to dimensionless form before use in the numerical study in Section 4.3, where the reasoning is further discussed relevant to the numerical modeling carried out. Note that the profile P_1 denotes the homogeneous case and it will be used to evidence the effect of transversal inhomogeneity on the damping of waves. This was not possible for the case of a fully ionised plasma due to the form of Equation (4.8). Figure 4.3 shows these profiles in dimensionless form.

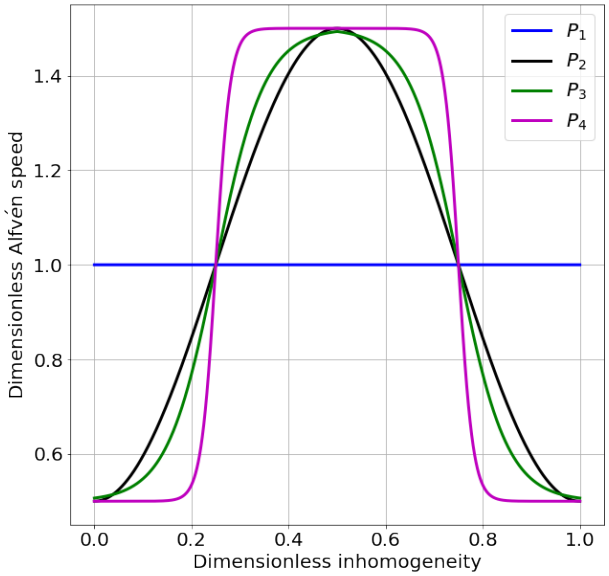

Figure 4.3: The different profiles of the Alfvén speeds used in the analysis are shown by curves of different colors. The constant Alfvén speed profile (shown here by the blue horizontal line) will serve as a comparison basis. Speeds and lengths are given in dimensionless units. The two tanh profiles are symmetric about the midpoint of the inhomogeneity in order to apply periodic boundary conditions to our numerical solver.

Since Equation (4.14) is not a simple exponential function, we cannot define a standard e-folding distance. However, we are still going to define the damping length as the length over which the initial amplitude of the wave decays by e-times, and this distance will be determined numerically. This is done by solving the equation

$$\left(\frac{z}{\Lambda_1}\right)^3 + \frac{z}{\Lambda_2} = 1, \tag{4.17}$$

and, this distance will be referred to as L_d^P. Similarly, to calculate the damping

length of Alfvén waves propagating in a fully ionised plasma, we solve the equation

$$\left(\frac{z}{\Lambda_1}\right)^3 = 1, \tag{4.18}$$

which can be solved exactly by $z = \Lambda_1$. This distance will be referred to as L_d^F, and will serve as a comparison to measure the reduction in damping length due to the presence of neutrals.

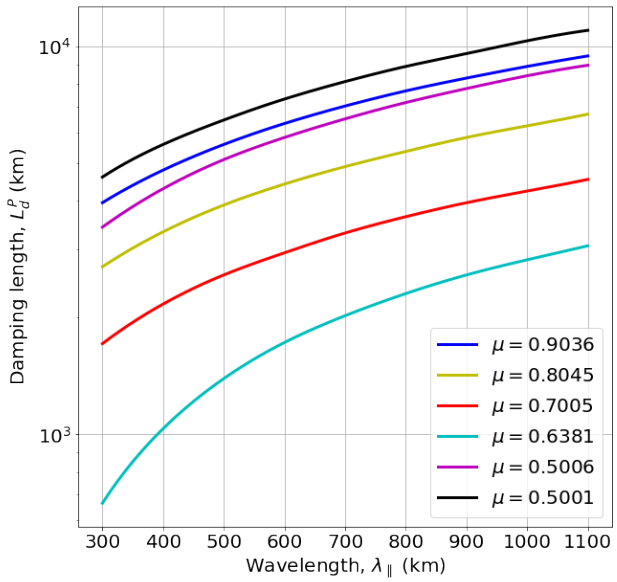

Figure 4.4: The variation of the damping length of phase-mixed Alfvén waves in a partially ionised plasma, L_d^P, in terms of the wavelength of the Alfvén waves. Here different ionisation degrees are shown by different colors.

The dependence of the damping length of phase mixed Alfvén waves propagating in a partially ionised plasma on the wavelength of Alfvén waves is shown in Figure 4.4 for different ionisation degrees (shown by different colors) for an Alfvén speed profile given by P_2. The values of the ionisation degree were chosen so that these cover the whole spectrum between a strongly ionised and weakly ionised plasma. Our results show that considering either very weakly ionised or very strongly ionised plasma results in weak damping and, therefore large damping lengths, too large to contribute to heating the solar chromosphere. This behavior can be attributed to the variation of the Cowling diffusion coefficient with the ionisation degree. In both of these cases (weakly and strongly ionised), the perpendicular currents are very small, thanks to the

very small number of neutrals in the case of the strongly ionised plasma, and a very small number of ions in the case of the almost neutral plasma.

Clearly, the damping lengths are shortest for shorter wavelengths across all ionisation degrees, the most effective damping occurs at ionisation degrees close to $\mu = 0.6$, where the combined effects of diffusion, viscosity, and ambipolar diffusion reach their maximum. According to the AL C7 model, this ionisation degree occurs at about 7,000 K and the ratio of ions to neutrals is approximately 1.31. The size of the damping lengths obtained in the "weak" limit highlights the efficiency of the phase mixing in partially ionised plasmas, here damping lengths can be as small as a few hundred kilometers (as opposed to the damping length of phase mixed Alfvén waves in a fully ionised plasma that is several thousand Mm). Inspired by these results we have investigated the number of wavelengths an Alfvén wave must propagate in order for its amplitude to decay by e-times as shown by Figure 4.5.

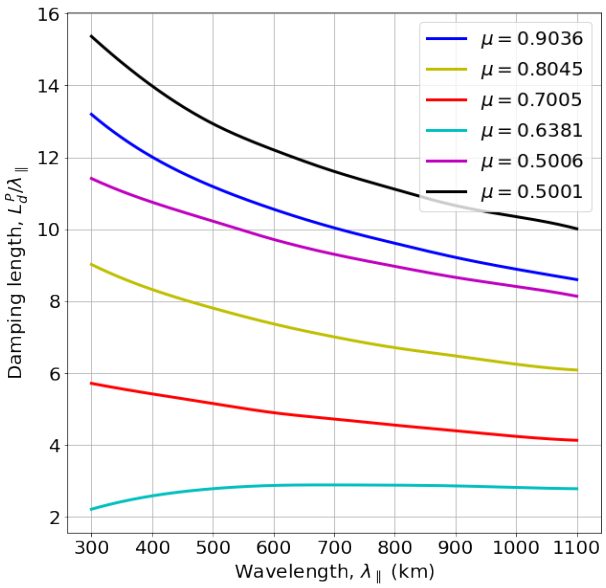

Figure 4.5: The number of wavelengths required for a wave to propagate before the wave is deemed t be damped. This is simply calculated by dividing the damping length of each simulation by the wavelength used to calculate the damping length. The curves obtained for different ionisation degrees are shown by different colors.

The results show that for ionisation degrees away from our optimum value of approximately 0.6, the number of wavelengths required to have propagated before damping is achieved reduces with an increased wavelength, while for

ionisation degrees close to 0.6 the ratio remains fairly constant, suggesting that the relationship between the damping length and the wavelength is rather linear.

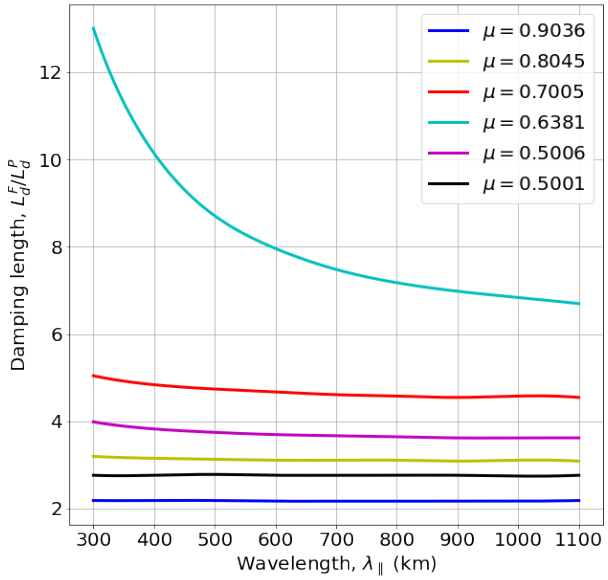

Figure 4.6: The ratio of the damping length of phase mixed Alfvén waves in fully ionised, L_d^F, and partially ionised, L_d^P, plasmas with respect to the wavelength of waves. The curves obtained for different ionisation degrees are shown by different colors.

The efficiency of phase-mixing on the damping of Alfvén waves in a partially ionised plasma becomes visible when we investigate the role of neutrals in this process. For this purpose we consider that by removing entirely the neutral species from the plasma, we have a fully ionised plasma for which the dissipative coefficients will be different and they are given by Heyvaerts and Priest (1983), however, the remaining plasma parameters (primarily temperature) remain relevant to the photosphere-chromosphere region. Figure 4.6 shows the ratio of the damping lengths obtained in fully ionised and partially ionised plasmas in terms of the wavelength of waves. The different ionisation degrees are shown by different colors. Our results show that the ratio in damping lengths is marginally larger for shorter wavelengths meaning the neutrals play a much more important role in wave damping, approximately an order of magnitude reduction in damping lengths when considering the effects of neutrals for ionisation degrees close to $\mu = 0.6$. This behavior is due to

the Cowling diffusion found in Equations (4.14) and (4.15). For short wavelengths (large $k_\parallel$), Λ_2 is small and hence is the dominant damping mechanism. For large wavelengths (small $k_\parallel$), Λ_2 plays a smaller role and hence for larger wavelengths we find our solutions to tend to a saturated ratio, this is a result of a superposition of solutions coming from the enhanced Ohmic diffusion and shear viscosity coefficients in a partially ionised plasma versus the fully ionised chromospheric plasma, i.e., the damping due to ambipolar diffusion plays a negligible role for large wavelength Alfvén waves, at least in the weak solution.

The regime in which each dissipative mechanism is dominant can be studied analytically by calculating the relative magnitudes of Λ_1 and Λ_2. After some algebra, we can see that the dominant damping mechanism of Alfvén waves in a partially ionised inhomogeneous plasma is dependent on the direction of the inequality of the equation below. If

$$2\pi^2\sqrt{\frac{3\eta_C^3}{\eta+\zeta}} \gg \frac{dv_A}{dx}\lambda_\parallel^2 \quad \text{or} \quad 2\pi^2\sqrt{\frac{3\eta_C^3}{\eta+\zeta}} \ll \frac{dv_A}{dx}\lambda_\parallel^2, \tag{4.19}$$

then the damping of the wave is predominantly due to the presence of neutrals or phase mixing respectively. If the two terms are of equal magnitude, both the presence of neutrals and phase mixing play equally important roles.

The damping length ratio pictured in Figure 4.6 corresponding to a nearly fully ionised case ($\mu = 0.5001$, shown by the black line) is independent of the wavelength of waves. In this limit, the contribution towards the overall damping length is due mainly to Λ_1, and the fact that this ratio is not one can be attributed to the 0.1% of neutrals still in the system. Furthermore, a similar trend for the weakly ionised cases can be recovered (blue line), that is due to the low values of the Cowling diffusion. These conclusions highlight the need for a balanced population of neutrals and ions in the process of phase mixing.

Before moving on to the full numerical study, we would like to evidence the effects of varying the Alfvén speed profile on the damping lengths of phase-mixed Alfvén waves in the case of the "weak" solution. We choose to showcase a single wavelength chosen to be $\lambda_\parallel = 400$ km and we plot the damping length against all heights associated with ionisation degrees in our range of study. The effect of the multi-valued ionisation degree is displayed here in Figure 4.7. The variation of the damping length in Figure 4.7 shows a clear trend of drastically decreasing the damping lengths when the presence of an inhomogeneous Alfvén speed is introduced, highlighting the efficiency of phase mixing as a mechanism

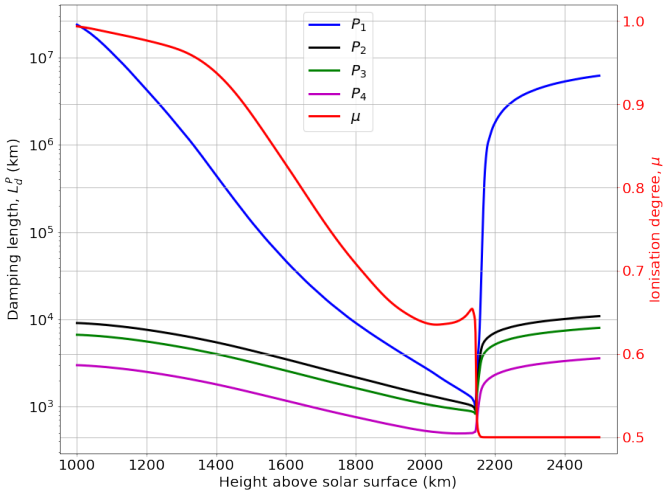

Figure 4.7: The variation of the damping length with height above the solar surface ranging from $1000 - 2500$ km in the case of the four Alfvén speed profiles ($P_1 - P_4$) given by Equation (4.16). The particular wavelength used here corresponds to $\lambda_\parallel = 400$ km. The overplotted red line shows the ionisation degree based on the AL C7 model (Avrett and Loeser, 2008).

to damp Alfvén waves effectively in the solar chromosphere. The shortest damping lengths are attained for the steepest profile (P_4) and for ionisation degrees for which an equal population of neutrals and ions are present.

Clearly, the inclusion of neutrals in the investigation of phase mixing of Alfvén waves results in significantly reduced damping lengths, in contrast to the fully ionised conditions. Perhaps most notably, the enhancement of dissipative coefficients via turbulence is unnecessary to achieve this damping effect. While certain assumptions necessary for analytical progress may not strictly apply to a partially ionised plasma, this outcome serves as a proof-of-concept, warranting further exploration through numerical modeling that permits the retention of all terms in the governing equation. The numerical solution derived from this approach is herein referred to as the "strong" solution.

4.3 Phase-mixed Alfvén waves propagating in a partially ionised plasma: Strong solution

The solution for propagating phase mixed Alfvén waves in an unbounded plasma given by Equation (4.14) and (4.15) can be considered as a "weak" solution, as it was obtained applying the same simplifications as in the study by Heyvaerts and Priest (1983) and they are connected to the small values

of dissipative coefficients (or very high Reynolds numbers). While these assumptions are obvious in fully ionised coronal plasmas, in a partially ionised chromospheric plasma, the transport coefficients are large and, therefore, terms containing products of dissipative coefficients have the potential to be not only important but dominant.

Under these circumstances, the governing equation describing the temporal and spatial evolution of the magnetic field perturbation in a single-fluid partially ionised plasma reduces to Equation (2.55). In Equation (2.55), simplifications were made regarding the order of magnitude difference between characteristic scales in the transversal and longitudinal direction, the second and third terms contain a derivative in the z direction because the Cowling diffusion is much larger in the chromosphere than the Ohmic diffusion and/or viscosity. Given the complexity of the above partial differential equation, the solutions are determined using a numerical method analogous to that used by Hood et al. (2002). We employ a 4th-order Runge-Kutta-based time step and a 2nd-order centered difference approximation for the spatial derivatives. In order to proceed with finding a numerical solution, we must first rewrite Equation (2.55) as a system of first-order dimensionless equations given by Equations (3.9)–(3.10).

Following Hood et al. (2002), we write all quantities in dimensionless form. Using finite difference approximations for the spatial derivatives to tackle the system of first-order Equations (3.9) and (3.10) inevitably leads to solving a large system of linear algebraic equations, which can be written in the form given by Equation (3.18) where A denotes a tridiagonal matrix with fringes, the coefficients of which correspond to the finite difference approximations. We then use a RK4 time-stepping algorithm to progress forward in time. The evolution of waves is followed until they reach a steady state or the perturbation reaches the end of the domain. The peaks of the damped wave are tracked and an envelope is fitted. We then calculate the percentage reduction in the amplitude after a given distance that the wave has propagated.

4.3.1 Sinusoidal wave driver

When studying the damping of an irregular signal such as a pulse it is informative to study how its constituent components damp. All signals can be approximated by a finite number of differently weighted *sine* waves represented by the Fourier decomposition of the signal. We could then construct

various other drivers from a finite collection of *sine* waves, each with a definitive damping length. In this study, we consider a continuous sinusoidal wave driver situated at the base of our domain. Understanding what are the main characteristics of waves and how they damp, we can generalise the idea to any driver and quantitatively predict the damping length of waves. That is why extending any of our work to more complicated drivers such as a pulse, broadband or random driver is a feasible task without major modification of our numerical program.

The damping of waves is followed for the four different Alfvén speed profiles specified by Equation (4.16). A constant Alfvén speed profile is chosen as a comparison basis to evidence the direct effects phase mixing has on the damping lengths of the waves. The Alfvén speed profiles used in our analysis are shown in Figure 4.3. Introducing an inhomogeneous Alfvén speed profile in the transversal direction results in the presence of varying wavelengths in our system. The range of the wavelengths present in our simulation is dictated by the maximum and minimum values of the Alfvén speed profile. In our analysis, we are going to follow approximately like-for-like wavelengths along the same field line and isolate the effects of a steeper local gradient rather than the effects of a broader range of wavelengths in the simulation. In order to concentrate only on the effect of inhomogeneity we chose the three inhomogeneous profiles such that their extreme values range between the same dimensionless values of 0.5 and 1.5.

For simplicity, throughout our analysis, we will follow the modification of the amplitude of Alfvén waves on the magnetic field line that corresponds to the intersection of all four profiles displayed in Figure 4.3 occurring at $x = 0.25$. This particular choice removes from the problem the discussion on the effectiveness of damping in terms of the wavelength of waves, however, this will be similar to the findings shown in the case of weak solutions. The profiles shown in Figure 4.3 are chosen such that the maximum gradient of the Alfvén speed profile occurs at the particular value of x.

4.3.2 Results

Our aim is to study the damping of phase-mixed Alfvén waves generated by a sinusoidal wave driver for varying ionisation degrees that are given by Equation (2.4). As the ionisation degree varies between the limits of fully ionised ($\mu = 0.5$) and fully neutral ($\mu = 1$) plasmas, an increase of the ionisation degree is somewhat equivalent to the case of a plasma whose temperature is decreasing

(assuming that the ionisation degree of the plasma is temperature-dependent only, i.e., the effect of radiation is removed).

Figure 4.8 shows the normalised value of the envelope in the case of an Alfvén wave generated by the four different Alfvén wave profiles considered in the present study. The waves have identical periods and the solutions are presented for the same ionisation degree ($\mu = 0.7852$). The variation in the envelope is caused by different levels of phase mixing due to the variation of the Alfvén speed profiles. The envelope is plotted by fitting a curve to the peaks of the generated Alfvén waves. The damping length is measured from the first peak, rather than from $z = 0$ to avoid any extrapolation errors. The horizontal red line marks the value of the normalised amplitude that corresponds to a e-fold decrease of the original value and the vertical lines mark the points where the envelopes of the waves intersect with the horizontal line. The damping length can then be calculated to be the distance between the first peak and the vertical line. The results show clearly that any inhomogeneous profile results in a shorter damping length, i.e., phase mixing indeed reduces the damping length of waves. Comparing these results with the profiles of the Alfvén waves shown in Figure 4.3, it is evident that the wave that corresponds to the steepest gradient undergoes the heaviest damping. The steep gradients enhance the contribution of the viscosity and diffusion in the Navier-Stokes and induction equation.

The percentage reduction in amplitude of Alfvén waves over the particular distance of 1 Mm from their first peak is displayed in Figure 4.9. This value was chosen to replace the damping length due to constraints on the size of the domain used in our numerical solver. Specifically, when waves propagate within a plasma of a certain ionisation degree, they may not reduce in amplitude by a factor of e upon reaching the end of the domain, hence it becoming impossible to accurately calculate the damping length. The percentage reduction of the amplitude is a quantity that is defined as

$$\mathrm{P}(\%) = \frac{A[0] - A[1]}{A[0]} \times 100, \tag{4.20}$$

where $A[0]$ is the initial amplitude of the Alfvén wave and $A[1]$ is the amplitude after the wave propagated a distance of 1 Mm. The results displayed in Figure 4.9 show the same trend as obtained in the case of weak damping, i.e., a plasma with an ionisation degree in the region of $\mu = 0.6$ produces the most effective damping, where for all the considered Alfvén speed profiles nearly all of the wave energy has been dissipated. For larger ionisation degrees (higher relative

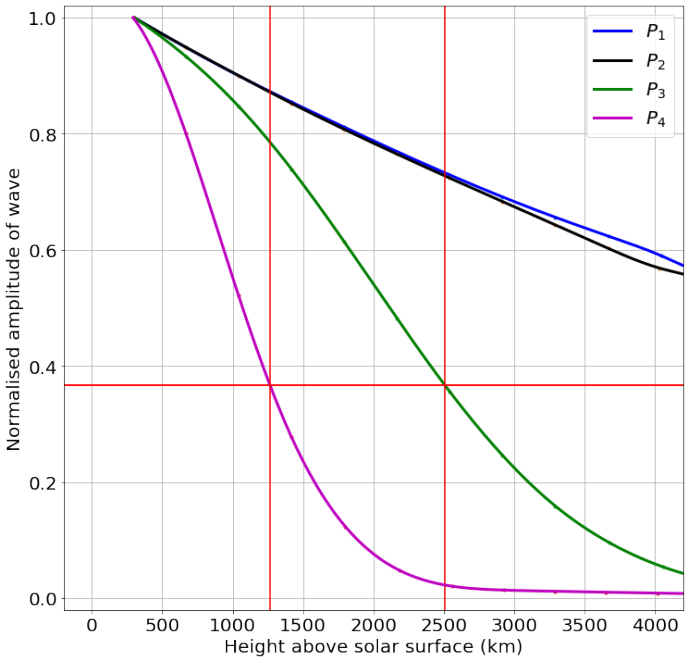

Figure 4.8: An envelope is fitted to the normalised maxima of Alfvén waves in the case of the four Alfvén speed profiles. The particular wavelength used in this figure corresponds to $\lambda_{\parallel} \approx 400$ km and the ionisation degree is set to $\mu = 0.7852$.

neutral densities) we recover a similar result as shown in Figure 4.8, i.e., the percentage change in the amplitude of the wave increases with the steepness of the Alfvén wave profile.

Now that we have established that phase mixing in partially ionised solar plasmas has the potential to damp waves very effectively within the chromosphere, let us estimate the amount of heat produced by the damping of phase-mixed Alfvén waves that are subject to damping due to Ohmic dissipation of parallel and perpendicular currents, as well as the conversion of waves' kinetic energy into heat due to viscous damping. In this case, the heating rate, Q, is calculated as the sum of the heating due to Ohmic heating, Q_{res} and viscous heating, Q_{ζ} (Priest, 2014; Melis et al., 2021)

$$Q = Q_{res} + Q_{\zeta} = \frac{1}{\mu_0}\left[\eta\left(\frac{\partial b}{\partial x}\right)^2 + \eta_C\left(\frac{\partial b}{\partial z}\right)^2\right] + \frac{\rho\zeta}{2}\left(\frac{\partial v}{\partial x}\right)^2, \tag{4.21}$$

where we retained only the dominant term in the expression of viscous heating. The variation of the heating rate with respect to the ionisation degree of the plasma for a given wavelength of Alfvén waves (400 km) propagating along the magnetic field line associated with the maximum gradient of the Alfvén speed profile P_4, shown by purple in Figure 4.3 is displayed in Figure 4.10. The

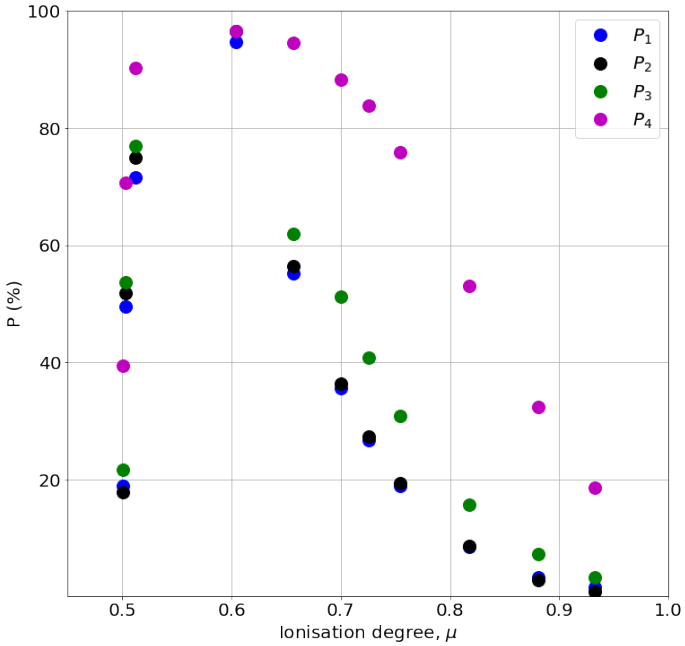

Figure 4.9: The percentage reduction in the wave amplitude after a propagating length of 1 Mm is plotted for various ionisation degrees, the Alfvén speed profiles are labeled in the legend. The steepest of the four profiles gives rise to the most effective wave damping, while all waves are damped effectively for ionisation degrees close to $\mu = 0.6$, where the values of viscosity, Ohmic diffusion, and ambipolar diffusion are at their effective combined maximum. For this figure we study waves with wavelength $\lambda_{\parallel} \approx 400$ km.

amplitude of the velocity perturbation was taken to be 2.5 kms^{-1} (Grant et al., 2018). For the sake of simplicity, we neglected the back reaction of the heating process on the values of dissipative coefficients and also the ionisation degree of the plasma. Given the particular dependence of dissipative coefficients, the values we determine constitute an upper limit.

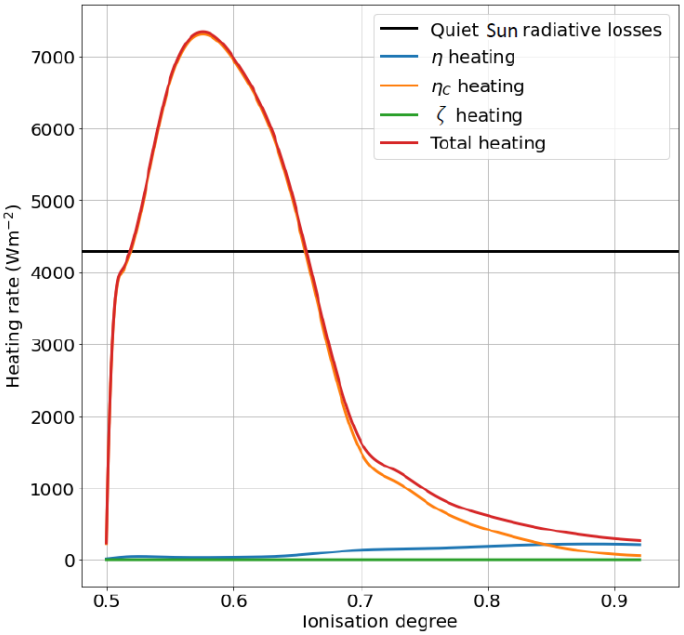

Figure 4.10: The variation of the heating rate with the ionisation degree of the plasma for the phase-mixed Alfvén waves with a wavelength of 400 km described by the P_4 profile. Heating rates associated with particular dissipative coefficients are shown in different colours. The horizontal black line shows the value of the heating rate of the quiet Sun equal to the average radiative losses of the chromosphere.

In order to estimate the efficiency of the phase-mixed Alfvén waves to heat the plasma, we use, for comparison, the estimated average heating rate of the quiet chromosphere. The radiative losses estimated from commonly used semi-empirical models of the quiet-Sun chromosphere are 4.3 kWm^{-2}, while in active regions, this value reaches 20 kWm^{-2} (see, e.g., Withbroe and Noyes, 1977; Vernazza et al., 1981; Yadav et al., 2022). The required heating rate to compensate for the radiative losses in the quiet chromosphere is shown by the horizontal black line in Figure 4.10. Our analysis reveals that the maximum heating rate produced by Alfvén waves varies considerably with the ionisation degree of the plasma, in the full spectrum of the ionisation the heating rate varies by more than one order of magnitude and it attains its maximum value for an ionisation degree of $\mu = 0.5761$. The results show that waves

propagating in a partially ionised plasma with ionisation degrees in the range $\mu = 0.5181 - 0.6570$ provide sufficient heating rates to balance chromospheric radiative losses. In the AL C7 atmospheric model, these values correspond to a ratio of neutrals to ions, $n_n/n_i = 0.0567 - 0.9171$, respectively. These values of

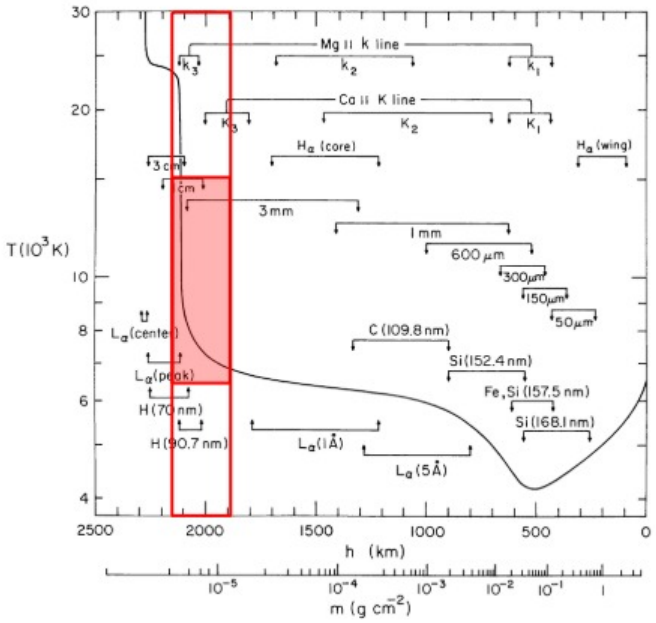

Figure 4.11: A composite figure showing the formation height and temperature of various continua and spectral lines taken from Vernazza et al. (1981) over which we plot the height and temperature range (shaded box) for which the heating rate produced by phase mixing of Alfvén waves is larger than the radiative loses in the quiet chromosphere.

the ionisation degree in the AL C7 model occur at the heights of 1916 and 2150 km above the solar atmosphere. It is instructive to compare our findings with the variation of the temperature with height in the VAL atmospheric model (Vernazza et al., 1981, their Figure 1) together with the approximate depths where various continua and spectral lines are formed (see Figure 4.11). The heights in between which the heating rate obtained by us is larger than the required heating rate are shown by vertical red lines, while the temperature at which the specific ionisation degrees occur is shown by red horizontal segments. In this way, we can define a region in the height-temperature diagram where phase-mixed Alfvén waves can provide the required heating. This domain corresponds to the region where the temperature increases dramatically and it is the location where the Lymanα and the 3 mm continuum intensity due mostly to free-free transitions of hydrogen is generated. These results show

that the increases in the temperature at the transition region level could be easily attributed to the phase mixing of Alfvén waves.

4.4 Conclusions

Ever since the seminal paper by Heyvaerts and Priest (1983), the damping of phase-mixed Alfvén waves propagating along magnetic field lines was suggested as a possible mechanism to explain the heating of upper solar atmospheric layers. One key drawback of the theory of phase mixing of Alfvén waves, when applied to the solar corona, was that the dissipative coefficients are very small, leading to damping lengths that are often as large as the solar radius. This was attributed to the very small value of transport coefficients in the solar corona.

Our study aimed to address this major shortcoming by investigating the problem in the chromospheric plasma, where transport coefficients are far larger, however, the plasma is partially ionised. Effective Alfvén wave damping due to phase mixing was achieved by imposing a density profile that varied in the transversal direction to the wave propagation. The main result of our research is that using realistic dissipative coefficients for the partially ionised chromospheric plasma results in an enormous reduction in the damping lengths compared to those for the fully ionised coronal case given by Heyvaerts and Priest (1983). Consequently, our estimations do not rely on turbulence to enhance transport mechanisms to bring the damping lengths to values that are important for heating. Small-scale mixing of magnetic field lines will create turbulence that can, even more, enhance transport coefficients (Magyar et al., 2017; Oppenheim et al., 2020).

Our results show that short wavelength Alfvén waves damp much faster than longer wavelength waves and the maximum attenuation of Alfvén waves occurs for ionisation degrees close to $\mu = 0.6$. For steep gradients and for dissipative coefficients corresponding to our optimum ionisation degree (or close to this), significant damping is seen for all wavelengths within 1 Mm of propagation. This length scale of damping could well explain a large amount of chromospheric heating with the rest of the energy left stored in the Alfvén waves propagating higher into the corona.

For waves with a particular wavelength of 400 km propagating in the presence of our steepest profile in the Alfvén speed, sufficient heating was generated due to the damping of phase-mixed Alfvén waves to balance radiative losses in the upper chromosphere/transition region when the ionisation degrees of the

plasma is in the range $\mu = 0.5181 - 0.6570$. This means that the phase mixing of Alfvén waves in partially ionised plasmas is indeed a viable mechanism for plasma heating.

Finally, we should mention that our approach used several simplifications that made the treatment of the problem of phase-mixing clearer. Key ingredients were neglected (e.g. height and time-dependence of dissipative coefficients and gravitational stratification), however, these might play an important role. As shown in Figure 2.5, the dissipative coefficients range by orders of magnitude over short distances. These coefficients dictate the heating rates of the simulated Alfvén waves and are considered constant within each simulation. In addition, the height range over which we found sufficient heating to balance radiative losses is less than a single wavelength. While we expect the wave damping to reduce when a vertically stratified plasma (at least in the context of the assignment of dissipative coefficients), the heating rates will remain sufficient within the range of values stated previously. Furthermore, as pointed out by Ofman et al. (1998) and Cargill et al. (2016), an assumed equilibrium density profile (at least in coronal plasmas) is not sustained due to the heating produced by the damping of phase-mixed Alfvén waves. Whether the same conclusion holds for chromospheric partially ionised plasma needs to be investigated by modifying our code to include a time-dependent Alfvén speed profile. It is our intention to expand the investigation of this problem and take into account the neglected processes in future analyses.

CHAPTER 5

Phase mixing of Alfvén waves in a single-fluid partially ionised plasma: the effect of various drivers

Understanding the dynamics of phase-mixed Alfvén waves propagating in partially ionised plasmas is crucial for elucidating various phenomena in astrophysical environments, such as spicules, fibrils or magnetic bright points. These waves play a fundamental role in transporting energy and momentum across vast regions of space, influencing the dynamics and contributing to the heating of the surrounding plasma. In Chapter 4, we examined the effects of phase mixing on Alfvén waves excited by a continuous single-frequency driver in a partially ionised single-fluid plasma environment, i.e., for frequencies much lower than the collisional frequency between particles. This investigation provided valuable insights into the evolution of wave energy and the associated heating mechanisms. However, due to the physical reality of the complex wave excitation mechanisms present in the solar atmosphere, the investigation of more sophisticated drivers becomes necessary.

Observations often approximate transverse displacements using single frequency sinusoidal wave profiles, however, it is highly unlikely that this displacement can wholly be represented by a wave consisting of a single frequency (Morton et al., 2016). The excitation of waves in the solar atmosphere is inherently complex, resulting from a superposition of various motions, including photospheric motions, intergranular buffeting, magnetic reconnection events, and interactions with existing magnetic field structures. These combined effects result in waves that are generated by a spectrum of frequencies. In this case, a driver consisting of multiple frequencies may be employed to more accurately model the observed disturbances in the solar atmosphere.

Additionally, observational evidence suggests that the observed displacements often seen in the solar atmosphere should be approximated by a sinusoidal wave lasting at most one to a few periods (see, e.g., Bate et al., 2022) or

interpreted as a pulse (see, e.g., Gosling et al., 2011). Hence, a more comprehensive understanding of the effect of various drivers on the efficiency of phase mixing and energy transport processes can be obtained through the investigation of wave propagation generated by a finite lifetime driver; more details will follow.

5.1 Various wave generation mechanisms

To begin our discussion of how varying the wave driver, affects the efficiency of the damping of phase mixed Alfvén waves in partially ionised solar plasmas, we first discuss a few possible scenarios where a different wave generation mechanism may be present, in doing so we give motivation to each of the new wave drivers considered.

5.1.1 Continuously driven waves

Continuous wave drivers have been inferred from the observation of decayless kink oscillations in coronal loops (see, e.g., Anfinogentov et al., 2013; Nisticò et al., 2013). The footpoints of coronal loops are firmly rooted in the photosphere providing compelling evidence for the existence of wave drivers that operate continuously within the lower solar atmosphere. While these disturbances will typically exhibit a dominant frequency, they are affected by convective photospheric motions and granular and intergranular motions, each influencing the characteristics of the wave profile excited. This interaction results in a broadband of frequencies that contribute to the behaviour of the resultant waves generated. Broadband wave drivers have been utilised extensively in various numerical simulations. For instance, the study by Karampelas and Van Doorsselaere (2024) replicated the effects of a broadband wave driver using a power-law-like approach, while Soler et al. (2017) investigated the propagation of torsional Alfvén waves from the photosphere to the corona, employing a broadband driver to obtain a proper estimation of the wave heating efficiency. Pascoe et al. (2015) characterised a broadband driver by approximating it as the cumulative effect of numerous discrete single-frequency wave drivers.

To begin an investigation into the efficiency of phase mixing at damping Alfvén waves generated by a broadband driver, we initially propose simulations employing a dual-frequency driver consisting of two distinct frequencies; one high-frequency (still lower than the ion-cyclotron and ion-neutral collisional frequencies, allowing for use of the single-fluid approximation) and a

low-frequency component. We refer the reader back to Chapter 3, where we outline the necessary numerical framework adjustments to extend our code to accommodate an arbitrary number of discrete frequencies. This approach is similar to that of Pascoe et al. (2015) whereby their footpoint driver is composed of several prescribed frequencies so that their sum is representative of a broadband signal.

5.1.2 Finite lifetime drivers

Magnetic reconnection stands as a cornerstone process in solar physics, serving as a driving force behind a multitude of solar phenomena such as solar flares, coronal mass ejections, and even the excitation of MHD waves. Magnetic reconnection occurs when magnetic field lines of opposite polarity break and reconnect, releasing energy in the form of heat and radiation, triggering various MHD waves. In the lower solar atmosphere, specifically in the photosphere and chromosphere, magnetic reconnection is believed to be the source of Ellerman bombs (EBs). EBs are intense brightenings seen in the extended wings of the hydrogen Balmer-α line (H-α), typically observed in complex bipolar active regions during periods of vigorous flux emergence (see, e.g., Watanabe et al., 2011; Vissers et al., 2013). Advanced numerical simulations by Hansteen et al. (2017, 2019) and Danilovic (2017) support the interpretation of EBs as markers of small-scale photospheric magnetic reconnection. Investigations by Rouppe van der Voort et al. (2016) and Joshi et al. (2020) identified ubiquitous EB-like brightenings in the quiet Sun, termed quiet Sun EBs (QSEBs), occurring far from regions of strong magnetic activity. These QSEBs present weaker enhancements of their H-α wings compared to those observed in regions of high solar activity (Nelson et al., 2017). The transient nature of EBs and QSEBs and their association with small-scale photospheric magnetic reconnection naturally present themselves as a potential source of pulse-like or finite lifetime driven Alfvén waves throughout the lower solar atmosphere. For a comprehensive review of EB properties, their diagnostics or their modelling (see, e.g., Rutten et al., 2013; Vissers et al., 2019; Fang et al., 2006). The transient nature of EBs and QSEBs and their association with small-scale photospheric magnetic reconnection naturally present themselves as a potential source of pulse-like or finite lifetime driven Alfvén waves throughout the partially ionised lower solar atmosphere. Understanding the behavior and propagation of these finite lifetime driven Alfvén waves in a partially ionised plasma is crucial for understanding their role in energy transport

and dissipation in the solar atmosphere, thereby motivating detailed modeling and simulations of phase-mixed Alfvén waves under these conditions.

5.2 Multi-frequency driver

In this section, we extend our numerical model from Chapter 4 to explore the impact of a multi-frequency driver on the behavior of Alfvén waves in partially ionised plasmas. By comparing the results with those obtained from a driver with a single-frequency, we can discern any unique signatures of multi-frequency drivers on wave propagation and damping processes in inhomogeneous partially ionised plasmas. Through this investigation, we seek to enhance our understanding of the intricate dynamics of Alfvén waves in partially ionised plasmas and their role in shaping astrophysical environments. The insights gained from this study have implications for wave studies in the partially ionised lower solar atmosphere.

Numerically, a multi-frequency wave driver can be implemented by summing together multiple harmonic drivers of varying frequencies and amplitudes. These frequencies can be made arbitrarily close to one another in period/frequency, resulting in a finite approximation of a continuous broadband driver. The initial conditions in the case of n harmonic drivers appear as per Equation (3.22). No further changes must be made to our code in order to simulate a driver of n frequencies.

By investigating the propagation and attenuation of phase mixed Alfvén waves with short lifetimes, we can further elucidate the intricate interplay between magnetic fields, plasma dynamics, and wave propagation in the partially ionised inhomogeneous solar atmosphere. Consequently, we expand upon our research presented in the previous chapter to encompass an exploration of diverse wave drivers, whose aim is to capture the range of wave generation mechanisms observed in the Sun. Our initial focus assesses the impact of a multi-frequency wave driver, before investigating finite lifetime sinusoidal drivers and pulse wave drivers.

5.2.1 Results

We retain the numerical setup discussed in previous chapters, including the Alfvén speed profiles given by Figure 4.3. As shown in Chapter 4, the presence of inhomogeneity is of key importance when calculating the damping lengths of phase-mixed Alfvén waves. We consider that Alfvén waves are generated by a

driver with two distinct frequencies of 13 and 67 mHz. Given the relationship between frequency and wavelength, the wavelengths corresponding to these frequencies vary with the Alfvén speed also. We continue, however, to select the Alfvén wave propagating along the magnetic field line that corresponds to the location of the maximum gradient in Alfvén speed (for profiles $P_2 - P_4$). Each of the Alfvén speed profiles have been designed in such a way that this maximum gradient also occurs for the dimensionless Alfvén speed equal to 1, or in dimensional units $v_{A0} = 20$ kms^{-1}. Hence these two frequencies correspond to wavelengths of 300 and 1500 km along the magnetic field line of interest, which is located at the maximum gradient of the Alfvén speed profile.

Here we present the solution obtained for each of the Alfvén speed profiles $P_1 - P_4$ introduced in Chapter 4 to show the efficiency of phase mixing on the damping of Alfvén waves in the partially ionised lower solar atmosphere.

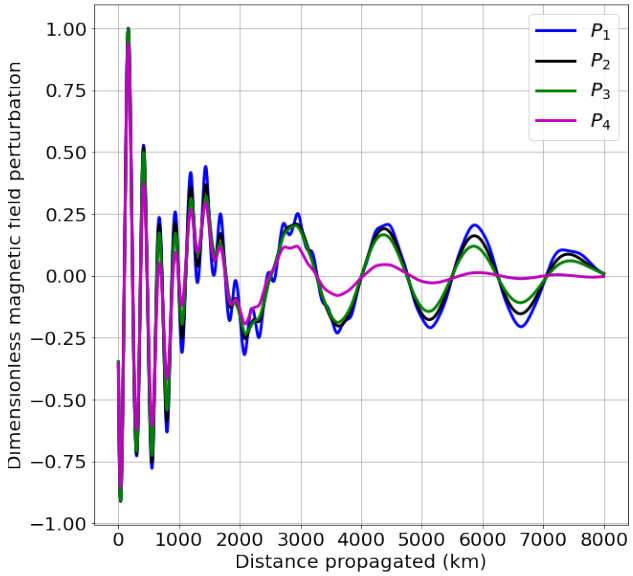

Figure 5.1: The variation of the dimensionless amplitude of magnetic field perturbation with coordinate z in the case of the four profiles of Alfvén waves ($P_1 - P_4$) defined in Chapter 4. Waves are driven by a two-frequency driver. Here we plot the results corresponding to an ionisation degree of $\mu = 0.6628$. Each simulation was terminated the moment the perturbation reached the end of the domain.

Examining Figure 5.1, it is clear that following the propagation of the wave across the 2−3 Mm range, the existence of even a modest gradient in the Alfvén

speed (as represented by profile P_2) significantly enhances the dissipation of the high-frequency component compared to the homogeneous scenario.

At the base of the domain, where the wave driver is located, the behaviour of the magnetic field perturbation is dominated by the high-frequency component of the driver. However, the high-frequency component of the Alfvén wave is killed off after propagating a distance comparable to the height of the chromosphere ($2 - 2.5$ Mm) while the low-frequency component propagates much further without full attenuation, suggesting that the energy stored in high-frequency waves is much more likely to contribute to the heating of the chromosphere since it dissipates over much smaller scales compared to the low-frequency oscillations that persist far out into the corona. This finding characterises the chromosphere as a filter for high-frequency waves, potentially explaining why we do not see such high-frequency waves persisting into the higher layers of the solar atmosphere, such as the corona and solar wind.

In order to evidence the effect of the ionisation degree on the damping of phase-mixed Alfvén waves excited by a multi-frequency driver, we plot the variation of the dimensionless magnetic field perturbation for the steepest Alfvén speed profile (P_4) for a range of ionisation degrees which span from very weakly ionised such that behaviour of the wave is dominated by neutrals, to strongly ionised, where the behaviour of the plasma is predominantly dictated by ions (see Figure 5.2).

Figure 5.2 re-confirms that ionisation degrees near $\mu = 0.6$ exhibit the most efficient damping of the phase-mixed Alfvén waves. This trend was consistent across all wavelength ranges, as discussed in Chapter 4. While the damping of Alfvén waves is evident in all considered ionisation degree cases, the result corresponding to $\mu = 0.6161$ shows that waves are overdamped, the high-frequency component dissipates within a single wavelength of propagation, underscoring the chromosphere's effectiveness in damping high-frequency disturbances. A wave with a wavelength of approximately 300 km, propagating in the presence of a steep inhomogeneity in a plasma with approximately equally neutral and ion populations will damp within about one wavelength, making them excellent candidates for heating the lower solar atmosphere.

For Alfvén waves propagating in a plasma with ionisation degrees approaching the limits of full ionisation ($\mu = 0.5$) or full neutrality ($\mu = 1$), the dissipative mechanisms, such as diffusion and shear viscosity, weaken correspondingly. Consequently, the damping weakens for Alfvén waves propagating in plasma that is either highly ionised or highly neutral, irrespective of the steepness

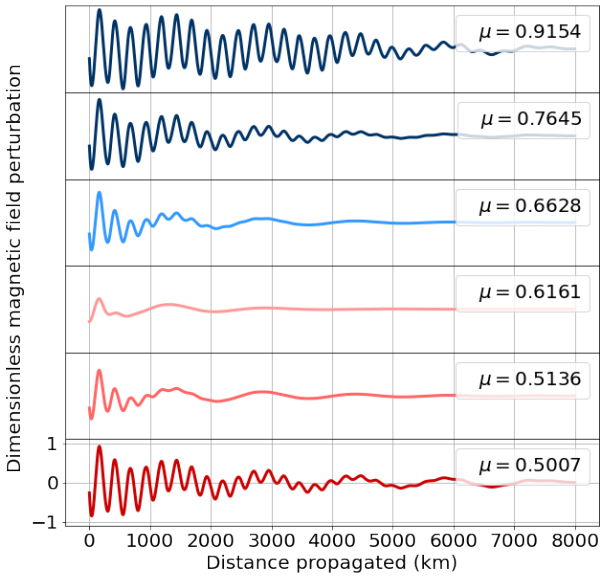

Figure 5.2: The evolution of the dimensionless magnetic field perturbation with distance generated by a dual-frequency driver for the P_4 Alfvén speed profile. Each subplot corresponds to a different ionisation degree, as indicated in the legend. The color gradient within the plot loosely represents a temperature profile, where blue signifies a cooler, weakly ionised plasma, while red indicates a hotter, strongly ionised plasma.

of the Alfvén speed gradient, as depicted in the top three and bottom two panels of Figure 5.2. This demonstrates the importance of strong transport coefficients in damping Alfvén waves.

In order to showcase the efficiency of the chromospheric plasma as a filter for high-frequency waves, we present a time series of the perturbation at two distinct locations in the domain, represented by the perturbation at the base of the domain, where no attenuation has occurred and a secondary location at a dimensional height comparable to the height of the chromosphere (2.5 Mm). We then take a Fourier transform of the signal at these two locations and plot the magnitude of the dominant frequencies.

In each simulation, the initial amplitude of the high-frequency component was made four times greater, such that at larger heights remnants of this component were more evident, while changes in the low-frequency component were also visible. Figure 5.3 shows that while the high-frequency component dominates the behaviour of the pulse at the base of the domain, the strength of this component is greatly reduced by the time it has propagated to the secondary location (2.5 Mm in height). This trend holds across all three ionisation degrees, with the high-frequency component experiencing complete attenuation in the simulation where an ionisation degree of $\mu = 0.6161$ is used.

Throughout the majority of simulations, a relatively small portion of the low-frequency component has damped in comparison to the high-frequency counterpart, with the remaining energy propagating to higher altitudes. The only exception is the case where an ionisation degree of $\mu = 0.6161$ and Alfvén speed profile P_4 is used. This effective damping occurs due to the combination of large dissipative coefficients and transversal gradients. The (near) complete attenuation of the high-frequency component, throughout all simulations, underscores the role of partially ionised chromospheric plasma as a filter for high-frequency Alfvén waves, providing a reason for the lack of observations of high-frequency Alfvén waves in the lower solar atmosphere. The two columns in Figure 5.3 correspond to the Alfvén speed profiles given by P_1 (left) and P_4 (right), allowing for the isolation of the transversal inhomogeneity's effect. Discrepancies between the left and right columns illustrate variations in attenuation attributed to the presence of an inhomogeneous Alfvén speed profile. Clearly, the inhomogeneous profile enhances attenuation across all simulations for both the low and high-frequency component. Nonetheless, the high-frequency component undergoes a relatively greater degree of attenuation.

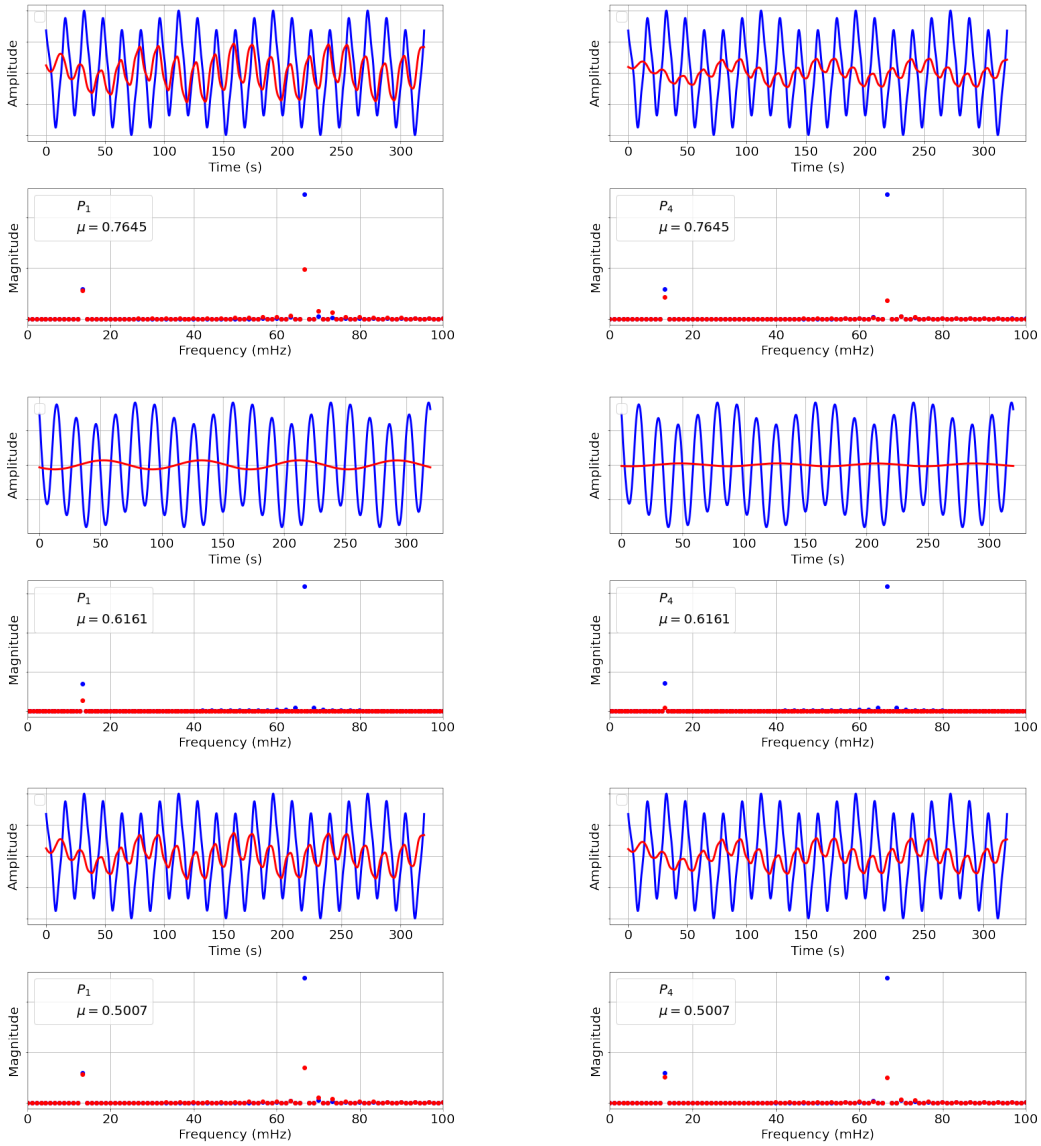

Figure 5.3: The time series of sinusoidally excited Alfvén waves at two different heights. The initial profile (depicted in blue) corresponds to the time series of the perturbation at the base of the domain, where the wave originates. The second profile (shown in red) represents the time series of the perturbation at a distance of 2.5 Mm from the base of the domain. Beneath each wave profile is the signal presented in frequency space, with colors matching the respective profiles described above. The discrepancy in magnitudes among the frequencies arises from the various dissipation mechanisms present in the chromosphere. The decrease in the magnitude of the high-frequency component of the signal demonstrates the chromosphere's effectiveness at dissipating high-frequency waves.

5.3 Finite lifetime drivers

Pulsating wave drivers have been employed extensively in numerical models conducting wave propagation/heating studies (see, e.g., Kumar et al., 2024; Chmielewski et al., 2014; Srivastava and Singh, 2023; Thurgood and McLaughlin, 2013; Tsiklauri, 2016). The problem of phase mixing of Alfvén pulses in fully ionised coronal holes has been investigated by Hood et al. (2002), who found that the amplitude decay rate behaved algebraically rather than exponentially, as was found earlier by Heyvaerts and Priest (1983). The authors assumed an initial profile disregarding the effects of the transversal Alfvén speed profile and the effects of diffusion during the excitation phase, eliminating the requirement of a time-dependent initial condition (i.e., the wave driver at the base of the domain). This reduces the computing expense greatly, examples of simulation outputs with these considerations have been presented in Chapter 3. In addition to this, the dissipative coefficients assumed here were roughly 6-7 orders of magnitude larger than formula predicts, requiring the underlying assumption of turbulence to explain this enhancement. In this investigation, we seek to address these shortcomings by introducing a time-dependent finite lifetime driver. This is accomplished by implementing the same methodology as the continuous drivers discussed earlier, with the distinction that the driver is turned off after a specified duration has elapsed, achieving the finite lifetime nature of this driver. A key distinction between this method and that employed by Hood et al. (2002) is that in our simulations, the perturbation is subject to phase mixing, diffusion and viscosity from the moment the magnetic field line is perturbed, providing more realistic simulations.

One of the main aims of this investigation is to explore the variation in damping of a finitely driven wave compared with a continuously excited wave. While working in the region of the solar atmosphere that is partially ionised, considering a wave driver with a lifetime any longer than a single period is likely to yield results very similar to that of a continuously driven wave when considering the attenuation of waves with wavelengths of at least a few hundred kilometers over distances comparable to the height of the chromosphere. We vary the frequency of the driver to achieve a varying initial wavelength along the magnetic field line of interest (as always, this corresponds to the magnetic field line at the location of the maximal gradient in Alfvén speed), allowing for comparisons of the efficiency of damping with respect to the frequency of the driver.

5.3.1 Numerical limitations

For certain ionisation degrees, we found that once the driver has been switched off, a high-frequency back reaction propagates in the wake of the pulse that -based on simulations of varying resolutions - is a numerical artefact. Unlike a numerical instability, this back reaction does not grow with time or propagation. The various damping mechanisms we consider work to dissipate this numerical solution. The amplitude of the back reaction is limited by the presence of the various diffusive quantities present in the simulation. For simulations whose ionisation degrees result in small dissipative coefficients, the amplitude of the back reaction can be comparable to the amplitude of the initial perturbation, however, for simulations where the chosen ionisation degree resulted in large dissipative coefficients, this back reaction becomes negligible or does not exist at all when we set an ionisation degree that is close to $\mu = 0.6$, the value which produced optimal damping and heating from the study conducted by McMurdo et al. (2023) and presented in Chapter 4. While many numerical codes include an artificial diffusive quantity to deal with instabilities or anomalous numerical artefacts, we do not impose any such increased anomalous diffusion. Since our investigation is focused on how the damping of phase mixed Alfvén pulses is affected by the ionisation degree, we impose only the physical diffusive quantities predicted by formulae for that specific population of ions and neutrals. To give the reader a visual representation of this effect, the back reaction can be seen in Figure 5.4, when considering an ionisation degree of $\mu = 0.7645$, Alfvén speed profile given by the P_3 profile and a driver producing an initial wavelength of 300 km.

It is highly likely that this effect occurs due to the various truncation errors involved in the finite difference approximations and finite time step used in the RK4 time-stepping routine and is a direct consequence of turning off the driver. The changes in wave profile observed for the finite lifetime driver due to the consideration of differing spatial and temporal resolutions were not seen in the case of the continuous driver. In order to avoid the influence of this back reaction on the damping of waves, here we consider ionisation degrees where this back reaction is negligible. The focus of this investigation is to study numerically the damping of phase mixed Alfvén pulses propagating in the presence of a transversally inhomogeneous Alfvén speed and examine the effects of the ionisation degree and wave driver frequency on this damping.

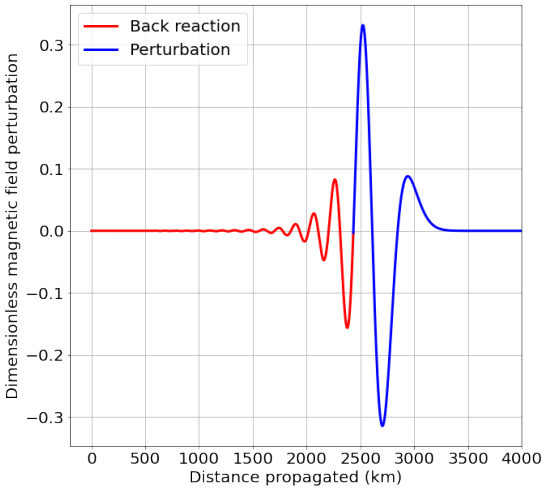

Figure 5.4: The profile of an Alfvén pulse excited using a finite lifetime sinusoidal driver. The initial perturbation is coloured in blue, while the high-frequency numerical back reaction is shown in red. The pulse was excited to a maximum dimensionless value of 1 and allowed to propagate until the end of the numerical domain. This simulation was performed for an ionisation degree $\mu = 0.7645$, Alfvén speed profile given by P_3 and a driver producing an initial wavelength of 300 km.

5.3.2 Results

For reasons explained in the previous section, we are going to consider a range of ionisation degrees $\mu = 0.504 - 0.663$, which corresponds to the neutral population making up approximately $2\% - 50\%$ of the total plasma population respectively. These ionisation degrees ensure a sufficiently small numerical back reaction discussed earlier. In our results, we accept back reaction amplitudes of the order of a few percent of the maximum amplitude of the wave. Note that as the ionisation degree approaches $\mu = 0.6$ this back reaction disappears as in the case when considering a lower frequency driver and hence larger wavelength, due to the reduction in the local longitudinal gradient of the perturbation and subsequent smaller *overshooting* errors in the finite difference formulae.

In order to demonstrate the variation in damping profiles obtained from simulating a finitely driven wave, we present the finite lifetime driven wave at various time steps, overplotted is the envelope of the continuously driven wave under the same conditions (i.e., Alfvén speed profile, ionisation degree and frequency of wave driver), normalised to align with the initial maximum and

minimum of the profile of the finite lifetime pulse. At the start of the simulation, the initial profile of the magnetic field line is unperturbed. Hence the first time step we plot corresponds to the moment the pulse has been perturbed for a single period. The profile of this pulse has already undergone some initial damping since phase mixing, and the various transport mechanisms begin working immediately upon perturbation of the magnetic field line. However, since the pulse perturbation is excited identically to the continuous driver, at least until the driver is turned off, the initial behaviour of the finitely driven and continuously driven waves are identical.

We begin by demonstrating the variation in behaviour indicative of all our results through a range of examples, considering cases of strong phase mixing, no phase mixing, and simulations for which the ionisation degree results in both strong diffusive quantities as well as weaker values.

Figure 5.5 shows that the continuously driven wave exhibits more efficient damping for all ionisation degrees considered. As the pulse profile expands, its effective wavelength increases such that the damping due to longitudinal gradients (predominantly Cowling diffusion) becomes less effective. In the case of the continuous driver, the persistent energy injected into the base of the domain works to preserve the wavelength of the Alfvén wave subject to phase mixing. This effect is not seen in the case of the driver with a finite lifetime, as there are no preceding waves. This result tells us that the dissipative mechanisms associated with longitudinal gradients (i.e., Cowling diffusion) are more important than the cross-field gradients (i.e., Ohmic diffusion and shear viscosity) when damping phase mixed Alfvén pulses, showcasing the importance of neutrals in dissipating Alfvén pulses in a partially ionised plasma. The widening effect we see in the case of the homogeneous Alfvén speed (left column) is due to the truncation errors involved in the finite difference approximations used throughout the numerical solver. In order to reduce this in future simulations, we could increase the order of the finite difference approximations and/or increase the resolution of the simulations, both of which result in additional computational expense. In order to ascertain the importance of the Alfvén speed profile on the attenuation of these pulses, we carry out a comparative study between the results of simulations adopting a homogeneous Alfvén speed profile and those with an inhomogeneous profile.

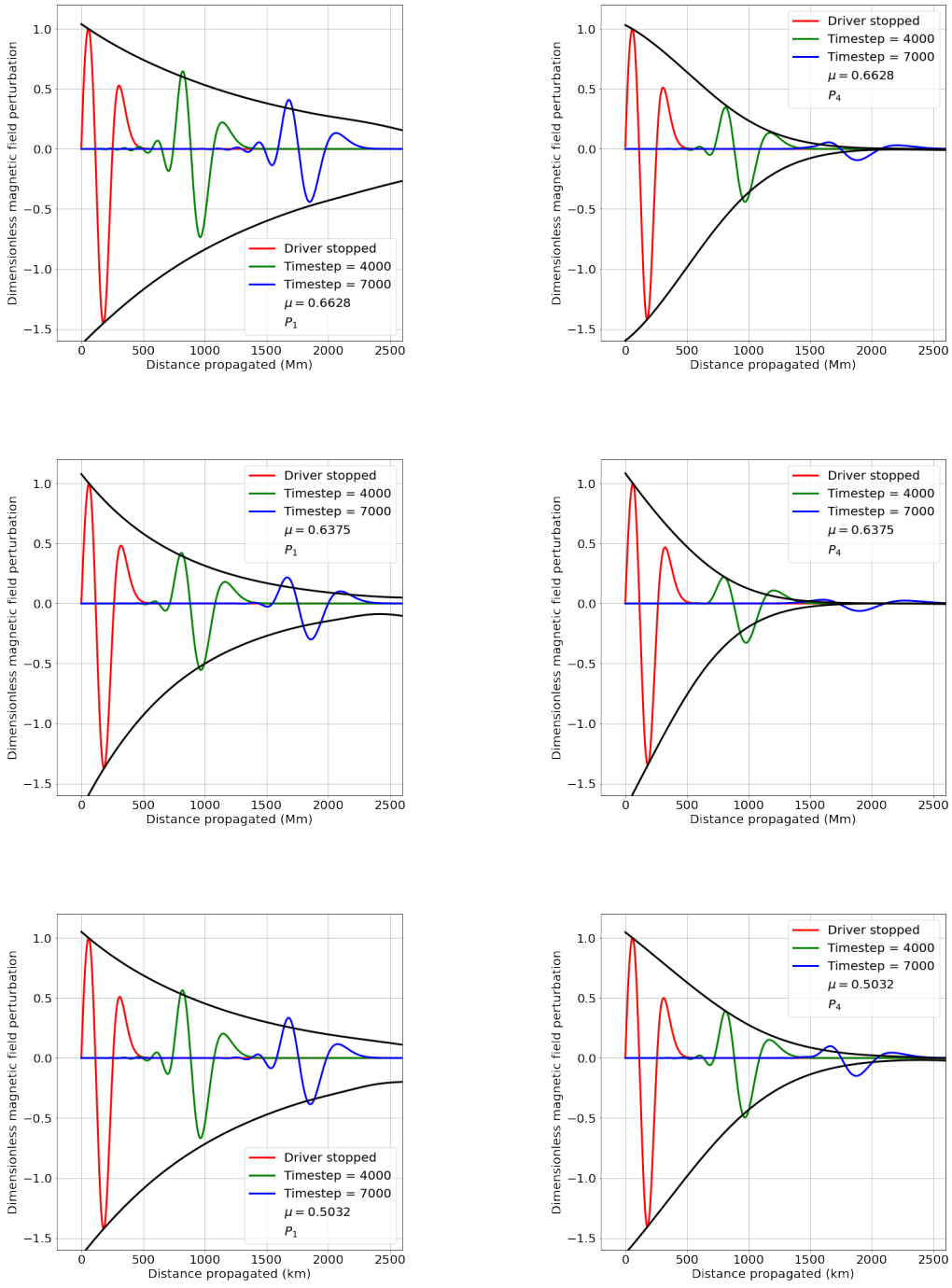

Figure 5.5: The evolution of a sinusoidally excited Alfvén pulse at three simulation time steps. The initial profile corresponds to the moment the driver terminates and represents a pulse with a wavelength of 300 km. Subsequent time steps reveal the evolution in the wave profile. Additionally, the envelope of the continuously excited Alfvén wave, generated under identical conditions, is superimposed for comparison (black line). Differences arise solely from the finite lifetime nature of the pulse, which lacks a continual energy injection at the domain's base. Here the two columns correspond to the P_1 and P_4 profiles.

5.3.3 Variation in damping due to Alfvén speed profile

Phase mixing works to enhance the dissipative mechanisms associated with cross-field derivatives. Due to the finite nature of the considered driver, the magnetic tension between field lines now causes an increase in the width of the pulse, since there is no constant injection of energy at the base of the domain working to regulate the wavelength throughout the simulation. Since the pulse widens with propagation, it is insufficient to use the amplitude of the wave as a proxy for the energy remaining within the disturbance, instead, we measure the variation in the total displacement of the wave to provide a more accurate representation. The displacement of a wave is defined as the absolute value of the area between the wave's profile and the z-axis along which it propagates. We now investigate the rate of change of the total displacement with propagation for a number of different cases. Here we study the variation in displacement for ionisation degrees ranging from $\mu = 0.504 - 0.663$ (with a dimensional frequency of 67 mHz, resulting in an initial effective wavelength of 300 km along the magnetic field that aligns with the location of maximal gradient in Alfvén speed), as can be seen in Figure 5.6, where all Alfvén speed profiles are distinguished by colour.

Our results show that the waves propagating in the presence of a steep Alfvén speed profile reduce in their total displacement far more effectively than those in a more weakly inhomogeneous ($P_2 - P_3$) or homogeneous profile (P_1). This clearly shows that while remnants of the perturbation are expected to protrude into the higher layers of the solar atmosphere, waves propagating in the presence of a strongly inhomogeneous Alfvén speed still deposit the majority of their wave energy before propagating a distance comparable to the height of the chromosphere. Clearly, throughout all simulations displayed in Figure 5.6, there is a distinct difference between the homogeneous case (P_1) and the most weakly varying inhomogeneous case (P_2). The effects seen in Figure 5.5 of the pulse widening in the case of the homogeneous profile, are understood to be small due to this distinct difference between the blue lines (representing P_1) and the black line (representing P_2) in Figure 5.6. The reduction in damping that occurs between the top-left, top right and middle-left panels in Figure 5.6, shows an initial decrease in ionisation degree, followed by an increase. This effect occurs due to the multivalued nature of the ionisation degree as plotted with height in Figure 2.1. The damping rates evident in the homogeneous case are presented as an upper bound (due to the additional dissipation occurring numerically). The true value is expected to reduce with

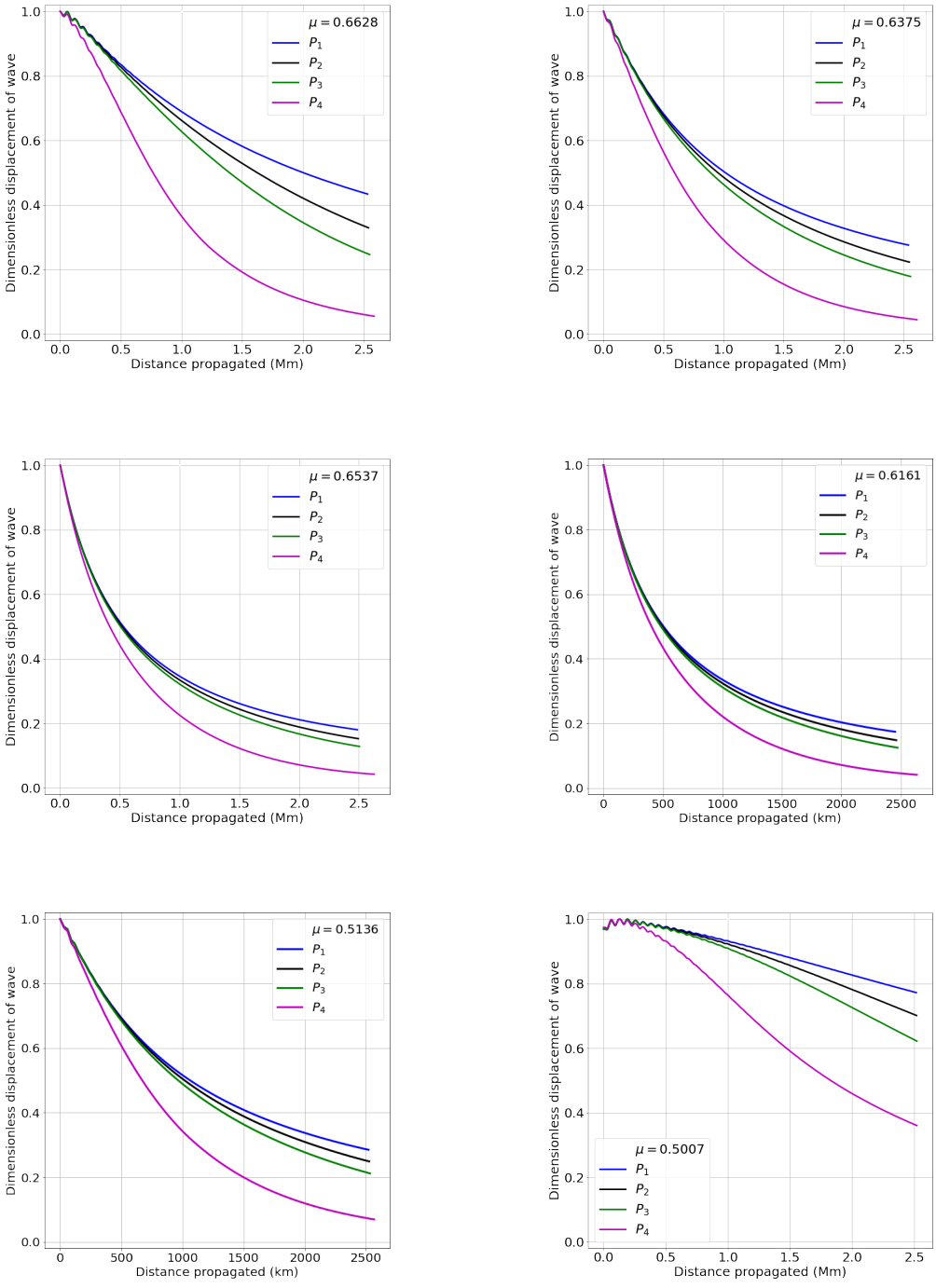

Figure 5.6: The variation in the displacement of each of the Alfvén pulses with propagation for the four different Alfvén speed profiles given by $P_1 - P_4$ profiles (shown by different colours), for six different ionisation degrees and an initial wavelength of 300 km.

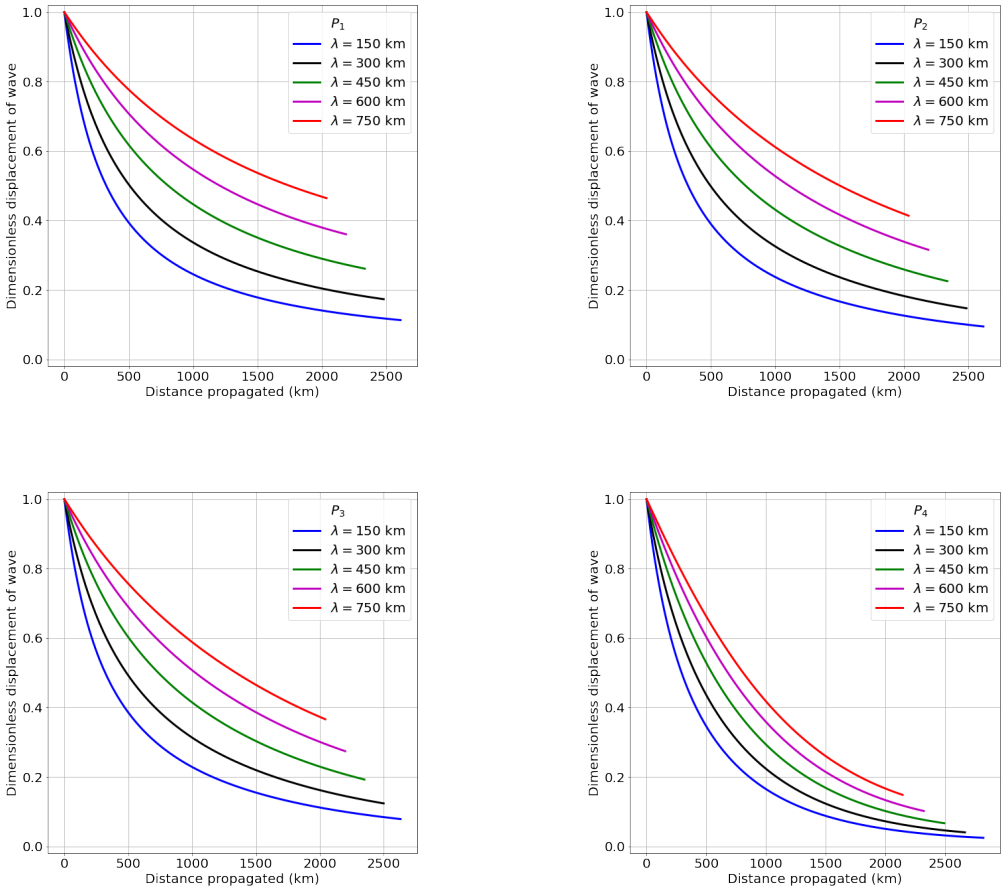

Figure 5.7: The variation in the displacement of finitely excited Alfvén waves with distance propagated for each of the four different Alfvén speed profiles considering a single ionisation degree given by $\mu = 0.6161$.

increased simulation resolution and an increased order of the finite difference approximations employed in the numerical modelling.

5.3.4 Variation in damping due to frequency

In the present study, we investigated five different frequencies of wave driver, with dimensional values varying from 133 - 27 mHz, which, prior to any stretching of the profiles of the waves (due to phase mixing), produce wavelengths of $150 - 750$ km, respectively. We choose again to present the variation in total displacement of the wave rather than the amplitude, to distinguish between the effects of phase mixing on widening the pulse. Retaining amplitude as our dependent variable is likely to lead to an overestimation in the efficiency of phase mixing at damping Alfvén waves excited for a finite lifetime.

The results of our simulations are shown in Figure 5.7 where we calculate

the propagated distance by measuring the distance the middle peak has propagated from the moment the driver is turned off. Simulations are terminated once the perturbation reaches the boundary of our numerical domain, in order to avoid effects corresponding to wave reflection. The centre peak was chosen to avoid the influence of an elongated wave profile in the presence of steep Alfvén speed gradients. The reason for the increased propagated distance with reduced initial wavelength can be easily explained. The middle peak occurs earlier in the domain for the shorter wavelengths allowing for the simulation to persist longer. The displacement of pulses with larger effective wavelengths are naturally larger than those with shorter wavelengths, hence, we normalise the total displacement of each pulse such that the initial displacement is identical between all simulations. Figure 5.7 clearly demonstrates that pulses with a shorter initial wavelength reduce their total displacement far more effectively than those with larger wavelengths; this result is analogous to the conclusions drawn in Chapter 4. The pulses with the shortest wavelengths dissipate their wave initially very quickly, with their decay rate dying off exponentially with propagation. In the case of Alfvén waves propagating in the presence of an inhomogeneous Alfvén speed, this initial rapid decay followed by a subsequent tapering-off of the decay rate can be attributed to the widening of the pulse, leading to shallower longitudinal gradients, resulting in dissipation mechanisms associated with these gradients becoming less effective. Waves with larger wavelengths decay at a much steadier rate. In the presence of the homogeneous Alfvén speed, it is only the shortest of wavelengths that dissipate their energy over the distance comparable to the height of the chromosphere, while for the steepest Alfvén speed profile, all wavelengths dissipate over 80 % of their wave energy within the same distance, highlighting the efficiency of phase mixing in damping Alfvén waves in partially ionised solar plasmas.

The oscillatory behaviour of the displacement evident in ionisation degrees at the extremes of values considered in Figures 5.6 and 5.8, is a numerical phenomenon, arising from deactivating the wave driver within a weakly diffusive plasma. This effect is particularly noticeable in the case of a high-frequency driver, due to the increased truncation errors relative to the wavelength. Examining the results, we do not expect this numerical effect to play a major role in the qualitative conclusions we draw.

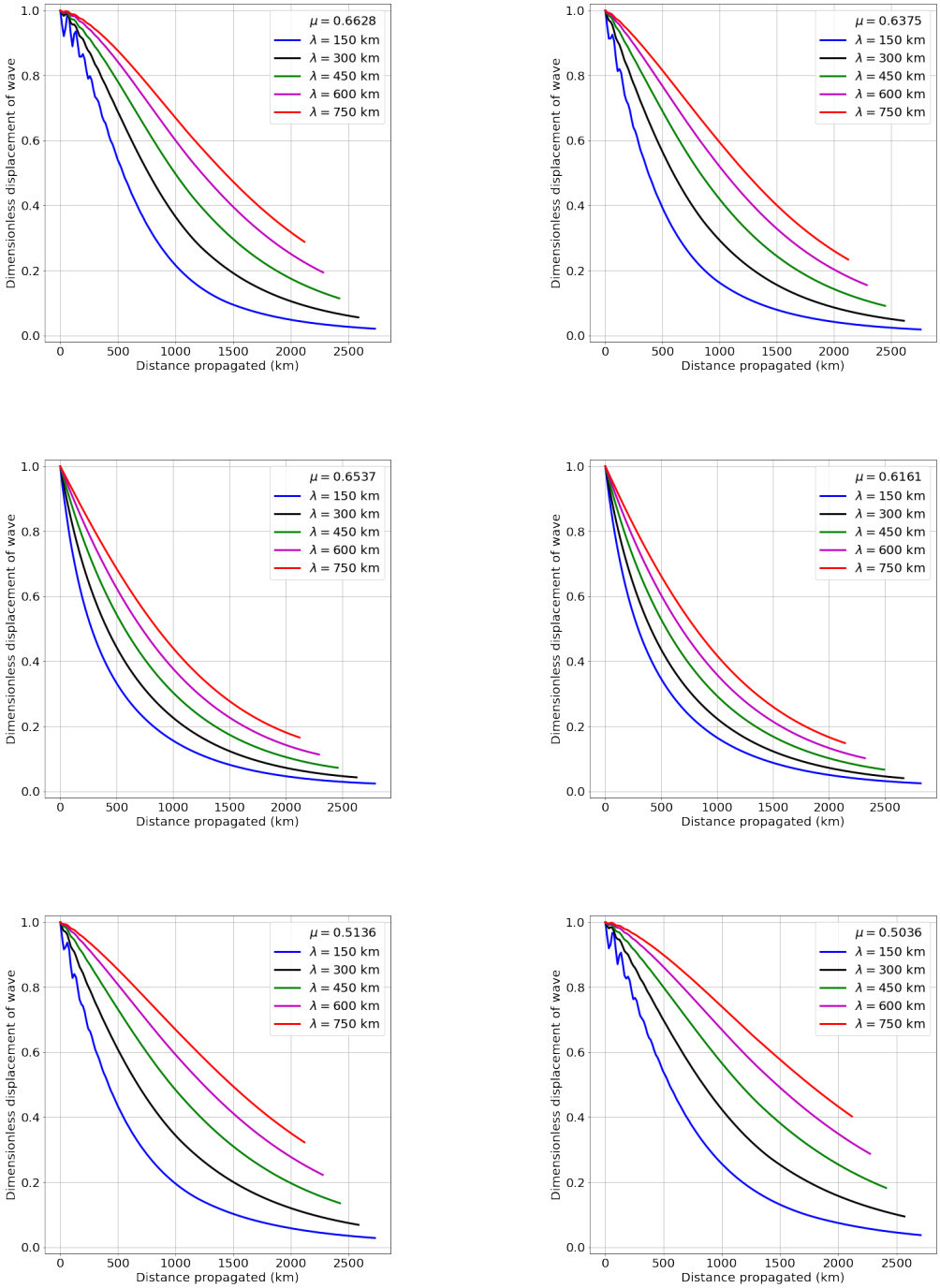

Figure 5.8: The variation in the displacement of finitely excited Alfvén waves with distance for the five different wavelengths for six different ionisation degrees in the case of the Alfvén speed profile given by P_4.

5.3.5 Heating rates

To truly investigate the efficiency of each considered driver at heating the surrounding plasma, we conduct a comparison in the heating rates obtained for the continuously driven and the finitely driven Alfvén waves, the results are shown in Figure 5.9. The heating profile of the continuously driven wave occurs at the point of the maximum amplitude of the wave and then decays as the perturbation decays. This occurs due to the large value of Cowling diffusion and its connection to the amplitude of the perturbation in Equation (4.21). The component of heating related to cross-field derivative increases to its maximum as phase mixing is allowed to progress, however, it serves only as a minor contribution towards the total heating rate.

The maximum heating rates for the two differently driven waves are initially identical, i.e., for time steps in the excitation phase of the finitely driven wave and the continually driven wave. However, due to the variation in the damping profiles of the two waves, we can focus on the evolution of the heating rates with distance, rather than the maximal values obtained. Since we have already shown that continuously drive phase mixed Alfvén waves can balance the radiative losses of the quiet solar chromosphere given an amplitude of 2.5 km s^{-1} propagating in a plasma with ionisation degrees $\mu = 0.5181 - 0.6570$, the same conclusion can be drawn for pulses. Due to the variation in behaviour of each wave, their heating rates will vary with propagated distance. The location of maximal heating propagates concurrently with the pulse and can be tracked and plotted against the heating profile obtained in the case of the continuously driven wave, once a steady state has been achieved. The results of our analysis shown in Figure 5.9 are displayed for a range of ionisation degrees and Alfvén speed profiles shown in the legend of each panel. We choose not to present the heating rates obtained from the viscous heating rate (Q_ζ in Equation 4.21) since it is many orders of magnitude less than the Ohmic heating and plays a secondary role. Note that the cases utilising a homogeneous Alfvén speed profile, result in the absence of transversal gradients and hence the absence of a heating component corresponding to Ohmic diffusion. Consequently, only heating resulting from longitudinal gradients (Cowling diffusion) is observed.

Figure 5.9 illustrates the dimensionless heating rates derived from simulations involving both continuously driven waves and those that are driven for a finite lifetime. The highest combined heating rates occur at the base of the domain, primarily due to the magnitude of the Cowling diffusion, which is

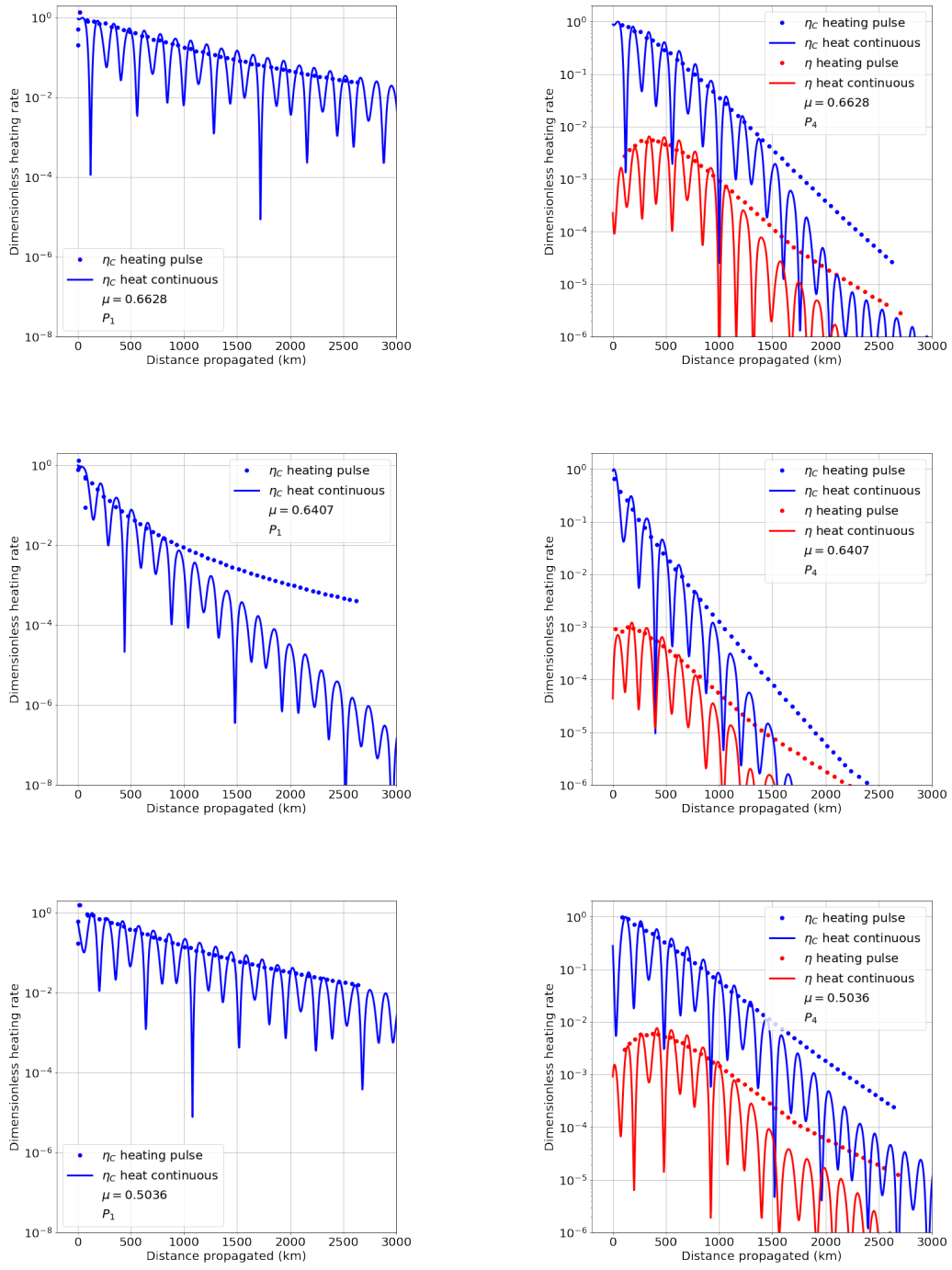

Figure 5.9: The profile of the heating rate obtained from the continuously excited sinusoidal wave driver (solid lines) is plotted with the tracked maximum heating rate of the finitely driven wave (dots) over the propagated distance. The discrepancy between the results shown in the two columns arises from the existence of an inhomogeneous Alfvén speed profile, depicted in the right-hand column. Each row corresponds to a distinct ionisation degree, consistent with the ionisation degrees used in Figure 5.5.

orders of magnitude larger than Ohmic diffusion. The Ohmic diffusion heating term grows with propagation to a point where it achieves its maximum value, before reducing due to the reduction in amplitude of the perturbation. The behaviour of the two waves studied here (continuous and finitely driven) are initially identical at the base of the domain (due to the way in which the finitely driven wave is excited). The slight discrepancies between the finitely driven wave (dots) and the continuously driven wave (solid lines) at a propagated distance close to zero, occur since we plot the heating profile of the continuously driven wave once a steady state has been achieved, hence the initial perturbation has propagated far away from the domain. This behaves slightly differently to the preceding wave since this propagates into a perturbed environment (rather than unperturbed in the case of the initial perturbation) and hence the heating at the base of the domain presents some slight variation in behaviour. Nevertheless, the purpose of this investigation is to study the evolution of the heating profile with propagation, since we have already shown these waves are capable of providing sufficient heating to counterbalance the radiative losses of the quiet Sun's chromosphere, see Chapter 4.

As depicted in Figure 5.5, instances arise where the amplitude of the pulses surpasses that of continuously driven waves, illustrated by the envelope plotted over the pulse profiles at various simulation time steps. The heating rate, given by Equation (4.21), is proportional to the square of the amplitude of the perturbation and the transversal and parallel gradients of the magnetic field perturbation. One of the effects that phase mixing has on the finitely driven waves, not evident in the case of the continuously driven waves, is the widening of the pulse profile, causing the longitudinal gradients to reduce, subsequently leading to a lower heating rate associated with the Cowling diffusion. These two competing effects of the increased amplitude yet reduced longitudinal gradients, result in the variation in heating profiles with propagation, as evidenced in Figure 5.9. Moreover, while transverse gradients in continuously driven waves can only grow to a certain extent before naturally realigning, another limiting behavior restricts transverse gradients in finitely driven waves. As the finitely driven waves propagate, magnetic tension between neighboring field lines results in an elongation and flattening of the disturbances profile. This occurs due to the lack of a continuous energy injection at the base of the domain that preserves the wavelength of the disturbance with propagation, and results in the magnetic tension not allowing these transversal gradients to grow excessively large. This limitation constrains the component of the heating

rate corresponding to Ohmic diffusion such that (for early times and distances propagated $\lesssim$ 500 km) it does not exceed values observed in simulations of continuously driven Alfvén waves, contrary to initial expectations. Only later in the simulations did the heating rates corresponding to the finitely driven wave significantly exceed those of the continually driven wave. This characteristic primarily stems from the greater amplitude of these disturbances at larger altitudes, leading to a rather paradoxical conclusion - does this really mean pulses heat the plasma more effectively than the continuously driven waves? To be able to answer this question, it is crucial to remember that although waves with larger amplitudes usually result in higher heating rates, this factor does not substantially address the atmospheric heating issue if waves do not damp, since there can be no conversion of waves' energy into heat occurring. Therefore, while the heating rates obtained for waves generated with a finite lifetime driver tend to exceed those excited by a continuous driver (at larger distances at least), this is attributed to the reduced damping rather than any particular efficiency in heating the solar atmosphere.

5.4 Conclusions

The investigation presented in Section 5.2, into wave propagation and damping in the solar atmosphere yields significant findings regarding waves that are generated by a dual-frequency driver. Our results show that even small gradients in the Alfvén speed, notably amplify the dissipation of high-frequency components as depicted in Figure 5.1, especially evident in regions with ionisation degrees near $\mu = 0.6$, as seen in Figure 5.2. Conversely, plasma nearing full ionisation or neutrality experiences weakened damping mechanisms, as illustrated in the top three and bottom two panels of Figure 5.2, consistent with findings presented in Chapter 4, underscoring the critical role of large transport coefficients in wave damping. Moreover, our analysis, depicted in Figure 5.3, elucidates the chromosphere's role as a filter for high-frequency Alfvén waves, evidenced by the attenuation of the high-frequency component and the persistence of the low-frequency counterpart. These observations contribute to our understanding of why high-frequency Alfvén waves are rarely observed in the solar atmosphere.

In addition, the investigation presented in Section 5.3 sheds light on the intricate behavior of wave damping in two distinct scenarios: finitely driven pulses and continuously driven waves. Our results, as depicted in Figure 5.5,

highlight instances where the amplitude of pulses surpasses that of continuously driven waves, leading to an impact on the evolution of the heating rate with propagation. We find that the heating rate, which depends on the square of the perturbation amplitude and the gradients of the magnetic field perturbation, is influenced by the interaction between amplitude and the longitudinal and transverse gradients. Phase mixing of finitely driven waves broadens the pulse profile, reducing longitudinal gradients and thereby lowering the heating rate associated with Cowling diffusion. This results in significant variations in heating profiles during propagation, as shown in Figure 5.9. Furthermore, as depicted in Figure 5.6, we observe a significant enhancement in the damping of phase mixed pulses in the presence of inhomogeneous Alfvén speed profiles, particularly notable for the extremes of the ionisation degrees simulated. Figures 5.7–5.8 illustrate the variation in damping rates attributed to the frequency of the driver, aligning with conclusions drawn in Chapter 4, where higher frequency waves demonstrate more effective damping.

While transverse gradients in the case of continuously driven waves exhibit a natural limit, finitely driven waves display similar behavior, thus constraining their growth. As waves propagate, magnetic tension between neighboring field lines elongates and flattens disturbances' profiles. This limitation on transverse gradients curtails the component of the heating rate corresponding to Ohmic diffusion. Interestingly, our simulations demonstrate that while heating rates corresponding to finitely driven waves initially replicate those of continuously driven waves, they can significantly exceed them at later stages, for certain plasma configurations. This phenomenon primarily arises from the greater amplitude of finitely driven disturbances at higher altitudes.

In conclusion, while waves with substantial amplitudes typically result in significant heating rates, the effectiveness of wave damping remains crucial. In general, we find the pulses to damp to a lesser extent than the continually driven waves for the same propagated distance. Our findings underscore the importance of understanding the complex interplay between the wave driver used in modelling, damping mechanisms, and propagation dynamics in resolving the atmospheric heating problem.

CHAPTER 6

Phase mixing of Alfvén waves in a two-fluid partially ionised plasma

6.1 Introduction

The results presented in Chapter 4 were obtained by adopting a single-fluid approach to modelling Alfvén waves. We showed that waves with a wavelength of the order of a few hundred kilometers are likely to damp within the lower solar atmosphere due to the short damping lengths obtained through simulations. They damp very effectively over distances comparable to the height of the chromosphere. Using either amplitude (in the case of the continuous driver) or total wave displacement (in the case of the finitely driven Alfvén pulses) as a proxy for energy, these results suggest that most of the energy stored in these waves is converted into other forms of energy, including heat. In addition to this damping, we showed that the resultant heating rates were sufficient to balance the radiative losses in the quiet Sun's chromosphere. Using a single-fluid framework allowed for modelling waves with frequencies much lower than the collisional frequency between particles. This approach is most suitable when modelling waves comparable to those seen by observers (see, e.g., Chae et al., 2022; Bate et al., 2022). However, that is not to say that higher frequency waves do not exist in the solar atmosphere, direct observations are merely beyond the capabilities of current technology. It is potentially very informative to investigate the effect phase mixing has on Alfvén waves in a frequency regime that is of the same order as the collisional frequency between particles, so much higher frequencies than employed in Chapters 4 and 5. In this limit we can use a two-fluid framework, where the fluid of charged particles can interact through collisions with the neutral fluid. Kraskiewicz et al. (2023) simulated monochromatic two-fluid Alfvén waves in the partially ionised solar chromosphere and found that small amplitude Alfvén waves damped very weakly, however, they did not include either transversal gradients, viscosity or diffusion. They did,

however, find that non-linear Alfvén waves excited by a large-amplitude driver could cause significant chromospheric heating and plasma outflows. Pelekhata et al. (2023) found supporting conclusions to Kraskiewicz et al. (2023) using the JOANNA code (Wójcik et al., 2017). Kuźma et al. (2020) found that high-frequency Alfvén waves driven at the bottom of the photosphere experience strong damping and those with an amplitude greater than 0.1 kms^{-1} can drive magnetoacoustic waves in higher atmospheric layers with corresponding heating rates large enough to compensate for the corresponding radiative and thermal-conduction energy losses. Martínez-Gómez et al. (2017) found that for high-frequency waves, resistive quantities became important transport mechanisms for dissipating wave energy, some of which we include in Equation (2.59), the subject of this present investigation. Russell and Fletcher (2013) found that wave damping is highly sensitive to the period and that while waves with frequencies > 1 Hz are damped effectively, waves with periods longer than 10 s pass through the chromosphere with relatively little damping. However, it is worth mentioning that lower frequency waves can still damp very effectively when considering large transversal gradients (see, e.g., McMurdo et al., 2023, and the results presented in Chapter 4), which was not accounted for in the study by Russell and Fletcher (2013). In this chapter, we focus on presenting the results derived from various simulations using the two-fluid numerical model introduced in Chapter 3.

The governing equation describing the spatial and temporal evolution of the velocity perturbation of charged particles was derived in Chapter 2, see Equation (2.59). Certain terms present in the two-fluid model do not directly appear under the single-fluid approximation, such as terms proportional with the collisional frequency between ions and neutrals, derivatives of the Alfvén speed, and terms containing the ratio of the ion-neutral densities. Since the mass of ions (assumed only to be hydrogen ions, essentially protons) and neutral hydrogen atoms are nearly identical, the ratio of their density can be thought of simply as the ratio of the number density ratio of ions and neutrals, both of which vary across the field in order to fulfill the requirement of transversal inhomogeneity. In order to simplify the problem, we are going to consider their transverse dependence to be proportional to one another, resulting in a coordinate-independent ratio. Expanding this investigation to encompass an overall transverse function necessitates no numerical adjustments, however, we defer this to future investigations. Nonetheless, it offers the potential to model

more realistic plasma configurations, where large gradients could be produced by misaligned neutral and ion density profiles.

A distinguishing feature absent in the single-fluid investigation, but apparent in the outcomes of the two-fluid modeling, is the influence of ionisation degree on wave propagation speed, as was eluded to in the conclusion of Chapter 2. Several terms dependent on the ionisation degree are connected with terms involving the (square of the) Alfvén speed, effectively causing a modification of the propagation speed as these terms vary with ionisation degree. A similar effect was seen in the case of magnetoacoustic waves by Soler et al. (2013), where the speed of propagation was influenced by the ionisation degree considered. This feature manifests in simulation outputs as a wavelength variation (for a given wave driver frequency). Consequently, complexities arise when evaluating the efficiency of wave damping across varying ionisation degrees, as the increased damping rate for shorter wavelengths cannot be fully addressed in the findings.

Hence, this alteration of wavelength due to ionisation degree might be considered an additional damping effect. Although there is no transport of momentum, this effect can be thought of as analogous to vertical stratification, where changes in wavelength are caused by variations in the Alfvén speed with increased height. In the solar atmosphere as the density decreases with height meaning the speed of an Alfvén wave increases with height (so long as the height dependence of the magnetic field is weaker than the square root of the density), this means that Alfvén waves will naturally have a shorter wavelength closer to the solar surface, where dissipative mechanisms associated with longitudinal gradients have a stronger effect. While theoretically feasible to calculate a frequency for each ionisation degree resulting in identical wavelengths across simulations, such an approach raises equally many challenges concerning variation in damping due to the driver frequency. The dependency of the damping rate on the ionisation degree may differ depending on whether another investigation was to employ different reasoning. We do not impose any definitive criteria in this present study and aim to draw conclusions irrespective of this phenomenon. In addition to this, the gradient of the collisional frequency affects the speed of propagation, albeit to a far lesser extent. These effects are presented and discussed further in the results section to follow.

Before we continue, however, we wish to draw the readers attention back to some earlier comments made at the beginning of Chapter 4. In order for the neutral fluid to be appropriately described as a fluid, one must consider

waves with a lower frequency than the collisional frequency between neutral particles. We found in the partially ionised solar atmosphere, that of all the combinations of collisional frequencies between particles, the neutral-neutral collisional frequency took the smallest values. However, it must be noted that the ion-neutral collisional frequency only exceeds that of the neutral-neutral collisional frequency by a factor of ≈ 1.3 (owing to the ratio of the collisional cross sectional values chosen for ion-neutral and neutral-neutral collisions). That is why, in the results to follow, we are able to model waves with frequencies close to the collisional frequency between ions and neutrals but not exceeding that. If higher frequency waves were to be studied, the neutral fluid must not be described in terms of a separate fluid, but rather a collection of particles interacting with a collisionally coupled ionised fluid. We omit further details as this is beyond the scope of the present thesis.

6.2 Results

Here we present an initial set of results as a proof of concept of the additional effects phase mixing can have on the damping of high-frequency Alfvén waves in partially ionised plasmas. We begin by presenting a set of examples representative of the more general results to follow in future work. In each panel below we present the wave profile of two Alfvén waves, each generated by a sinusoidal wave driver with equal frequencies, each panel representing a different ionisation degree. The variation in wave profiles is achieved by the presence of a homogeneous (blue line) and an inhomogeneous (red line) Alfvén speed profile given by P_1 and P_4, respectively. Figure 2.2 shows that the collisional frequency varies by many orders of magnitude from the bottom of the photosphere to the top of the chromosphere, however, we set the frequency of waves to be studied in this chapter to be comparable with the collisional frequency between ions and neutrals at the top of the chromosphere, to allow for direct comparisons across a range of ionisation degrees in the solar atmosphere. Hence, we consider a wave driver with a dimensional frequency of 8 Hz, with future directions of study presented in Chapter 7. We retain a continuous sinusoidal wave driver for each simulation, and the resulting variation in wavelength from panel to panel is a result of the ionisation degree dependent quantities multiplying terms corresponding to the (square of the) Alfvén speed. The variation in wavelength within each panel (i.e., between the red and blue line), while a much smaller effect (most visible in the bottom

right panel representing $\mu = 0.6537$), is as a result of the direct appearance of transversal derivatives multiplying the (square of the) Alfvén speed depicted in the governing equation, where a homogeneous plasma renders these terms zero. The various parameters we chose in order to non-dimensionalise our equation and begin this investigation are $v_{A0} = 20$ km s^{-1} and $L = 10$ km.

The panels that correspond to an ionisation degree of by $\mu = 0.6407$ and $\mu = 0.6537$ (the bottom two panels) show an extraordinary increase in damping in the presence of an inhomogeneous Alfvén speed profile. These disturbances are wholly damped within two periods, contrasting with the homogeneous case which undergoes a fairly steady attenuation. This stark reduction in damping is a result of the various ionisation degree-dependent quantities in Equation (2.59) related to the transversal derivatives, which become greatly enhanced in the presence of an inhomogeneous Alfvén speed profile. This effect is attributed to phase mixing, and these initial results are qualitatively analogous to those presented in previous chapters.

As theory predicts, phase mixing emerges as an efficient damping mechanism for Alfvén waves by enhancing the significance of dissipative coefficients associated with cross-field gradients. It is important to note that excluding viscosity from our simulations, results in the homogeneous and inhomogeneous Alfvén speed profiles yielding identical wave propagation profiles since all transversal gradients correspond to either ion or neutral shear viscosity coefficients. The collisional frequency does give rise to transversal gradients, but its manifestation requires the presence of neutral viscosity, as evident from the fourth term on the right-hand side of Equation (2.59).

Figure 6.1 also shows that the wavelength is ionisation degree-dependent. This effect can be seen when studying Equation (2.59) since ionisation degree dependent quantities multiply the (square of the) Alfvén speed, effectively increasing/decreasing the speed of propagation as these coefficients are varied. While it is hard to distinguish between the effects of the ionisation degree on the efficiency of damping due to this variation in wavelength, we aim to investigate the influence of varying the ion-neutral collisional frequency on the behaviour of the wave and its damping, in order to gain deeper understanding into the qualitative characteristics of various solutions to Equation (2.59).

6.2.1 Importance of ion-neutral collisions

Measuring the importance of ion-neutral collisions on the damping lengths obtained for phase mixed Alfvén waves in a two-fluid plasma can achieved

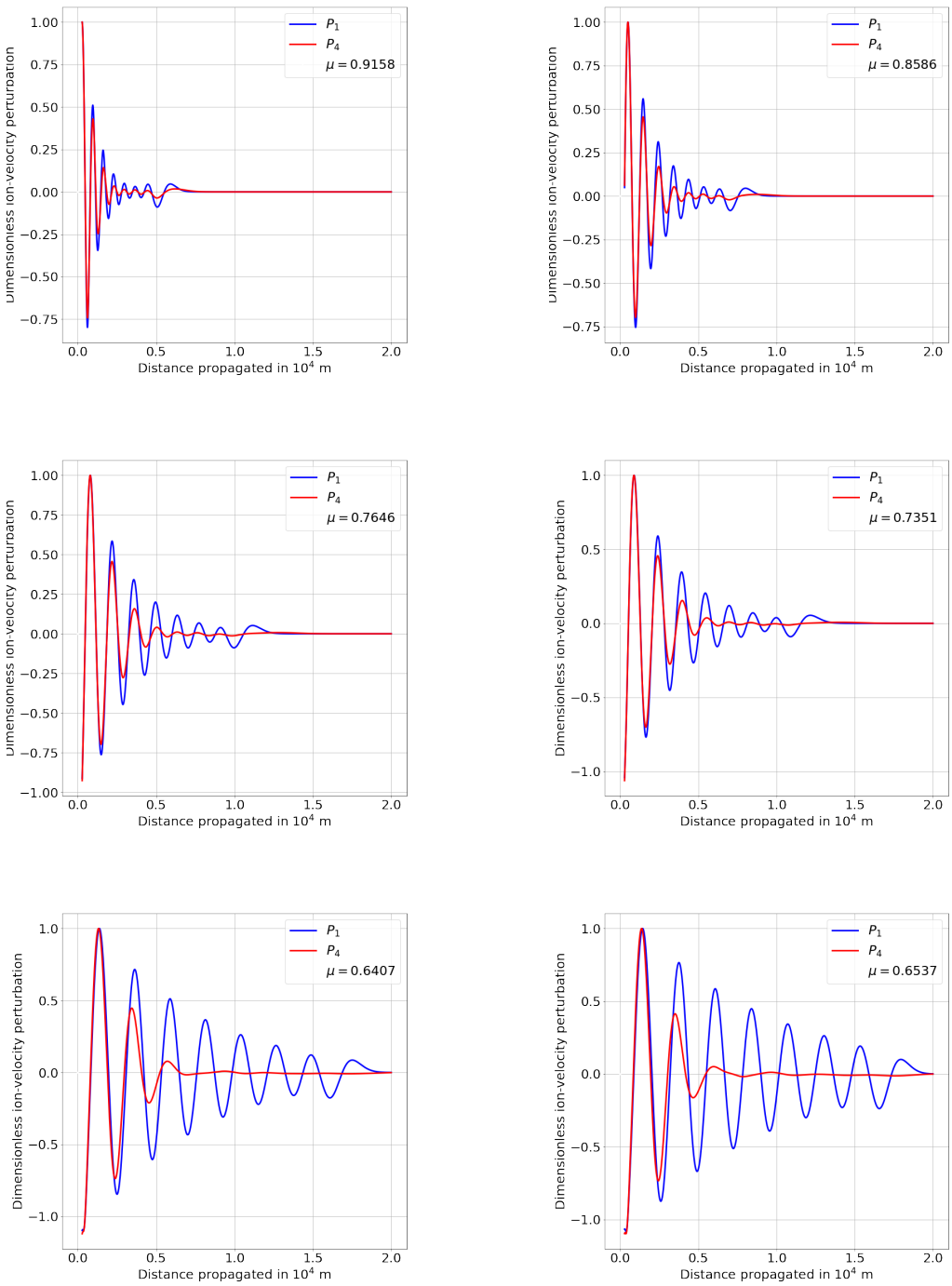

Figure 6.1: The spatial evolution of sinusoidally excited Alfvén waves in a two-fluid plasma. The variations shown within each subplot stem exclusively from the inclusion of a gradient in the Alfvén speed profile. Distinctions across panels are determined by transverse derivatives of the collisional frequency, along with ionisation-dependent factors, namely the ion-neutral collisional frequency term and the shear viscosity coefficients.

by varying the neutral density by various user defined factors. We impose no changes on the viscosity as a result of this, in an attempt to isolate the effects of increased ion-neutral collisions on the damping rates of the waves considered. We present results representative of the partially ionised chromosphere below in Figure 6.2 for a single ionisation degree of $\mu = 0.7351$ for the steepest inhomogeneous Alfvén speed profile given by P_4.

Figure 6.2 illustrates the sensitivity of the solution to the ion-neutral collisional frequency. As this frequency increases, the obtained damping lengths significantly decrease. This reduction is primarily due to the enhanced damping effects typical of a more collisional plasma, naturally a wave will lose energy over shorter timescales when we introduce a larger collisional frequency. Additionally, a secondary damping effect arises from the reduced effective Alfvén speed and the resulting shorter wavelength. Shorter wavelength Alfvén waves inherently have reduced damping lengths due to the increased significance of longitudinal damping effects such as viscosity and collisions. The reduction in wavelength is due to the combined effect of the terms related to the increased ion-neutral collisional frequency, which multiply the square of the Alfvén speed in Equation (2.59). For a collisional frequency reduced by a factor of 5 (Figure 6.2, top left panel) resulted in a damping length of an order of magnitude larger than that obtained for the case where the ion-neutral collisional frequency was enhanced by a factor of 5 (Figure 6.2, bottom right panel).

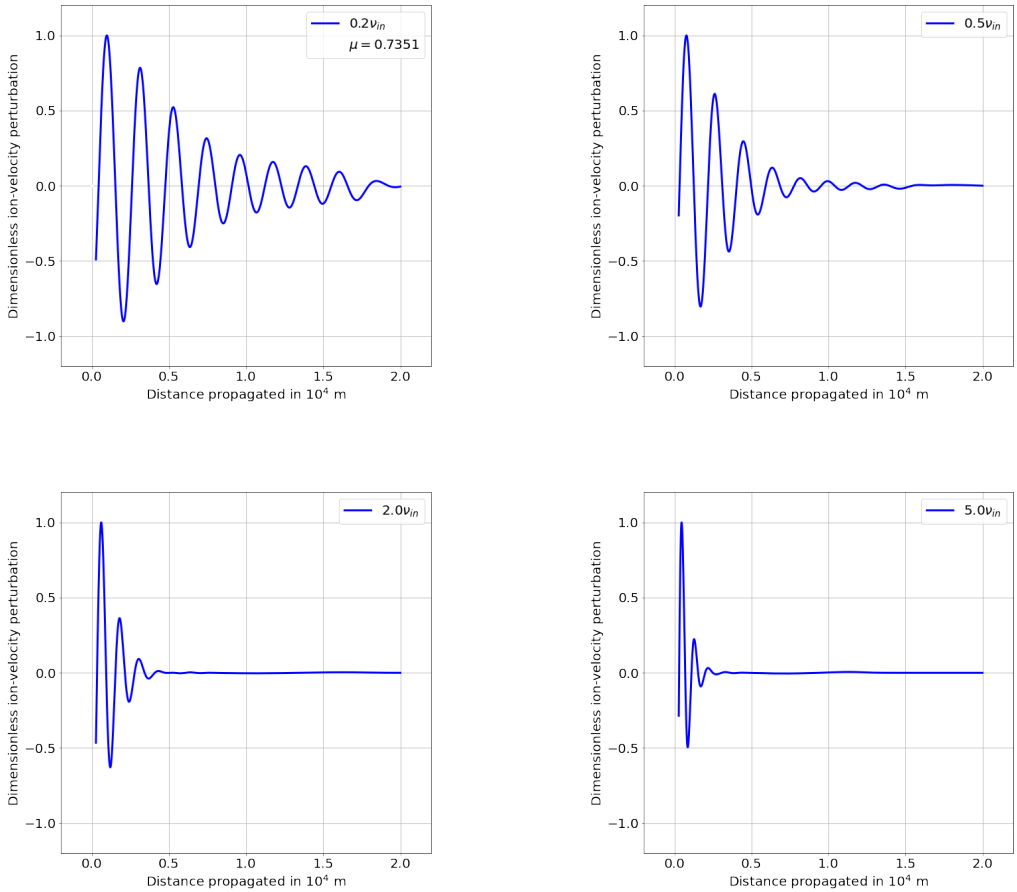

Figure 6.2: The evolution of Alfvén waves under varying ion-neutral collisional frequencies across four different cases propagating in the presence of the Alfvén speed profile given by P_4. Each subplot represents a different collisional frequency. As the collisional frequency increases, the damping of the Alfvén waves becomes more pronounced, illustrating the sensitivity of wave propagation to collisional effects. The effective wavelength and damping lengths decrease with higher collisional frequencies, highlighting the impact of collisions on wave dynamics in partially ionised plasmas.

6.3 Conclusions

In summary, our initial results provide a foundational understanding of the additional effects of phase mixing on damping high-frequency Alfvén waves in partially ionised plasmas, as depicted in Figure 6.1. In general, we found that the presence of an inhomogeneous Alfvén speed profile considerably increased damping rates across all ionisation degrees as shown in Figure 6.1. Notably, Figure 6.1 demonstrates that the presence of an inhomogeneous Alfvén speed profile leads to remarkable damping enhancements particularly for waves propagating in a plasma with ionisation degrees close to $\mu = 0.6$, attributed to phase mixing enhancing the efficiency of the various damping mechanisms, which achieve their maximum for ionisation degrees close to this value.

We demonstrate the sensitivity of the solutions obtained on the collisional frequency between ions and neutrals. Increasing the ion-neutral collisional frequency results in a reduction in wavelength and increases the damping rates greatly.

Without taking into account the variation in wavelength seen in both Figure 6.1 and 6.2, one has to conclude that as we approach a more collisional plasma, which is naturally dominated by neutrals (as per the numerous figures presenting the solar parameters based upon the AL C7 model, Avrett and Loeser, 2008), we obtain shorter and shorter damping lengths. We propose this initial set of results to demonstrate a proof of concept of the effects of phase mixing in the two-fluid regime and wish to address the effect of a reduced wavelength in more detail in future work. Furthermore, in a future work we plan to address the heating produced by phase-mixed Alfvén waves subject to viscosity and collisions between particles and compare these values with the average radiative loss in the solar chromosphere.

Overall, we conclude that phase mixing can act as a dominant damping mechanism for two-fluid Alfvén waves in partially ionised plasmas, with its importance varying depending on the ionisation degree considered. We propose that conducting a comprehensive parameter study in future research will offer more insight as we delve deeper into the phenomenon of phase mixing under the frequency regime of a two-fluid plasma. These findings serve as a proof of concept for broader investigations, shedding light on the significant role of ionisation degree-dependent quantities on the attenuation of Alfvén wave profiles.

CHAPTER 7

Conclusions and future research prospects

7.1 Thesis summary

The present thesis contains a detailed summary of my research investigating the phase mixing of Alfvén waves in partially ionised solar plasmas. Such inhomogeneous plasma environments are characteristic of solar atmospheric regions (such as the solar photosphere and chromosphere) where the temperature is not high enough to ensure a completely ionised plasma. In this case, the plasma is made up of negatively and positively charged particles (electrons and protons in the case of a purely hydrogen plasma) and neutrals that interact with each other through collisions. Partially ionised plasmas are known to host a number of specific transport processes that receive a different connotation in the light of the collisional processes that take place.

To answer the above scientific question, we have introduced some fundamental concepts and motivations for the research presented in Chapter 1. Here, we reviewed some key results on the role of waves in the solar atmosphere, essential concepts and results from the field of partially ionised plasmas, we reviewed the current state-of-the-art in the field of phase mixing, highlighting the shortcomings of the present modelling of this problem and we presented the methodology that stays at the foundation of our research.

The mathematical framework for our analysis is presented in Chapter 2 where we derived the governing equations in a single-fluid and two-fluid approximation. As stated, the distinction between these working frameworks resides in the frequency regime in which physical effects are investigated. While in the case of a two-fluid plasma, the frequencies are comparable with the collisional frequencies (but lower than the cyclotron frequency) of particles, the single-fluid approximation assumes that the frequencies are much smaller than the collisional frequency between all particles. For each case we have discussed what sort of transport mechanisms operate.

Chapter 3 introduces the numerical setup designed to simulate Alfvén waves propagating in plasma environments with density inhomogeneities. It captures and resolves the intricate interplay between various ionisation degree-dependent dissipative processes and phase mixing, and their impact on Alfvén wave attenuation. Through these numerical models, we present the effects of phase mixing in partially ionised environments. Continuously excited Alfvén waves, characterised by frequencies much lower than ion-neutral collisional frequencies, are modeled within a single-fluid framework. Remarkably, our simulations, presented in Chapter 4, reveal that Alfvén waves with a wavelength of 400 km and an amplitude of 2.5 kms^{-1}, propagating within a plasma with an ionisation degree ranging between $\mu = 0.5181$ and $\mu = 0.6570$, possess the capability to balance the radiative losses within the quiet Sun's chromosphere.

In Chapter 5, we revisited the problem of phase mixing in a single fluid approximation, however, we investigated the efficiency of this process depending upon the nature of the driver. In particular, we introduced two additional wave drivers (a multi-frequency and a finite lifetime driver), offering insights into the chromosphere's efficacy as a filter for high-frequency (short wavelength) Alfvén waves. Through Fourier analysis of the perturbations at two locations, one at the domain's base and a second at a distance comparable to the height of the transition region (top of the chromosphere), we unveil the chromosphere's role in filtering high-frequency perturbations, preventing them from reaching larger heights in the solar atmosphere. This important result explains the lack of high-frequency wave observations in the lower solar atmosphere and the effective damping of high-frequency waves (and consequently plasma heating) in the solar chromosphere. In this chapter, we have explored the unique behavior of phase-mixed Alfvén waves induced by a finite lifetime pulse-like wave driver. Unlike continuously driven waves, pulse-driven waves exhibit a widening of the wave profile with propagation, increasing the wavelength of the resultant perturbation. This behaviour can be attributed to the absence of a continuous injection of energy at the base of the domain and the presence of an inhomogeneous Alfvén speed. This phenomenon subsequently leads to variations in heating profiles, wherein heating rates at later times exceed those observed in continuously driven waves. We attribute this to the reduced attenuation stemming from the increased pulse width and subsequent reduction in longitudinal gradients. Notably, the reduction in wave damping is not counterbalanced by the reduction in amplitude caused by the widening of the pulse.

We proposed a secondary numerical model in Chapter 6, suited to describing the phase mixing of Alfvén waves in partially ionised plasmas with frequencies comparable to the ion-neutral collisional frequency, i.e., we employed a two-fluid (charges and neutrals) framework. While the results presented in this chapter are intended to be primarily a proof of concept on the effects associated with phase mixing of Alfvén waves in this frequency regime, we observed consistent findings with the single-fluid approximation and novel insights unique to the two-fluid framework. Similar to the single-fluid approach, steep gradients in Alfvén speed and the presence of substantial dissipative coefficients (especially prevalent at ionisation degrees near $\mu = 0.6$) led to diminished damping lengths compared to homogeneous scenarios or results from simulations of ionisation degrees with correspondingly low dissipative coefficients. Notably, specific ionisation degree-dependent quantities in the two-fluid governing equation affected the propagation speed of the Alfvén wave, a characteristic typically discerned only in the single-fluid approximation through consideration of vertical stratification.

The purpose of the present thesis has been to develop an area of new research, combining partial ionisation and phase mixing, with the aim to present quantitative and qualitative results emphasising the importance of partial ionisation, phase mixing and the complex interplay between the two on Alfvén wave damping in the solar atmosphere. Throughout this study, it has been essential to simplify the various governing equations to allow for progress to be made. Nevertheless, we acknowledge the limitations inherent in these simplifications. In future endeavors, we aim to address these simplifications to better understand the impacts of partial ionisation and phase mixing on Alfvén wave damping and subsequent heating of the surrounding plasma.

7.2 Future work

We recognise that the results presented in this thesis deal with the problem of phase mixing of Alfvén waves assuming several simplifications. However, one of the main aims of the study summarised here was to carry out a proof of concept investigation and to investigate the consequences of a partially ionised plasma on the efficiency of phase mixing. That is why the research presented here can be expanded in many ways. A summary of the possible pathways is given below.

One way our research can be expanded is by including the effect of plasma stratification, as studied by De Moortel et al. (1999); Smith et al. (2007); McLaughlin et al. (2011). In particular, we look to investigate the effectiveness of phase-mixed Alfvén waves in a stratified solar atmosphere where dissipative coefficients are given by a realistic solar atmospheric model (e.g., VAL, FAL, AL) in a single-fluid limit, where the magnetic field is represented by a 2D expanding magnetic configuration, similar to the method developed and studied by Ruderman et al. (1998); Ruderman and Petrukhin (2018). We wish to extend the models of the previously mentioned authors to include a vertically stratified partially ionised lower solar atmosphere (photosphere, chromosphere, transition region and corona). We expect these additions to further increase the heating rates associated with the damping of phase-mixed Alfvén waves, providing further evidence that the damping of Alfvén waves strongly contributes to heating the solar chromosphere. Indeed, Ruderman et al. (1998) found that expanding magnetic field lines tend to increase the efficiency of phase mixing and lead to a more efficient damping of Alfvén waves. The length scales involved in a single-fluid framework are of the order of observational resolution of various instruments, meaning that many of the parameters, such as wavelength and perturbation amplitudes, can be taken from observations, as was the case for our presented results.

In addition, most MHD wave models (including our own) assume an environment that remains static or evolves only slowly compared to the period of the waves so that both timescales (the timescale on which the medium evolves and the period of the wave) are clearly separated. However, at chromospheric temperatures, cooling happens on a timescale of about 100 seconds. This timescale is the order of the period and/or damping time of many waves and oscillations observed in the solar atmosphere. A modification in the local temperature, and hence the local density structure, will alter the MHD wave behavior and, for phase mixing, this process could either be a self-enhancing mechanism (by continuously creating extra density structuring, leading to drifting of the heating layer), be self-destructive (by eventually smoothing out the original density inhomogeneity, e.g., see Cargill et al., 2016) or shifts the location of heating (McLaughlin et al., 2011). Using an extended version of the code we developed, one could determine the efficiency of MHD wave phase mixing in maintaining hot chromospheric plasma by undertaking a comprehensive parameter study to determine the range of parameters and dissipation coefficients for which rapid heating and cooling of the local plasma critically alters

phase mixing. This approach requires a model where the plasma parameters are time-dependent, which poses increased numerical complexities since the matrix detailed in Chapter 3 now needs to be reconstructed at each time step as each parameter changes in time. Perhaps a WKB approximation may be appropriate here, allowing for a framework by which the background quantities vary slowly compared to the oscillations of the magnetic field lines, allowing for a simplification of the governing equation one must solve.

Our investigation on the problem of phase mixing of Alfvén waves in two fluid plasmas can be considered as a very good starting point for a more detailed analysis of this problem. The consideration of separate fluids for charges and neutrals involves much richer physics, and the analysis of all possible effects that could play a role in the problem of wave damping due to phase mixing can be carried out in the future. Many extensions can be applied to the two-fluid code in order to study phase-mixed Alfvén waves at frequencies of the order of the collisional frequency between particles (charged and neutral). Since we found that the short wavelength phase-mixed Alfvén waves could balance radiative losses in the quiet chromosphere, it is only reasonable to expect even shorter wavelength (i.e. higher frequency) waves will heat the plasma more effectively. Now, the dominant dissipative mechanism is the momentum transfer between various species, while other "classical" transport mechanisms will be used to ensure the creation of transversal gradients. As Kraskiewicz et al. (2023) and Pelekhata et al. (2023) found that high-frequency waves are the most promising candidates for chromospheric heating, a full parametric study could shed light on the efficiency of phase mixing on damping Alfvén waves in a two-fluid plasma incorporating a large range of driver frequencies. Vertical and longitudinal inhomogeneity can be included to accurately model high-frequency waves propagating in the presence of small-scale plasma density inhomogeneities. However, depending on the frequencies of the wave driver, the longitudinal scale height may be much smaller than the density scale heights in the chromosphere. Nevertheless, this model also allows us to include non-equilibrium ionisation effects (i.e., the continuous change in the ionisation degree of the plasma due to the increase in the temperature) that will provide further insight into the way Alfvén waves are damped in partially ionised plasmas.

Another important addition to the problem of Alfvén wave phase mixing in a two-fluid approximation is the problem of ionisation non-equilibrium.

As propagating Alfvén waves undergo damping and transfer their kinetic energy into heat, the chemical composition of the plasma is constantly changing, meaning that source and sink terms in the mass conservation equations for charges and fluids must be considered. In this situation, the species loses momentum due to the effects of recombination and ionisation that can modify the efficiency of phase mixing. When calculating the energy balance produced by phase-mixed Alfvén waves, non-LTE effects can be taken into account, which will allow for the investigation of the full consequences of heating processes on the formation of various optically thick chromospheric spectral lines (e.g., Mg, Ca and H_α) and allows for forward modeling of plasma heating in partially ionised solar plasmas to be carried out.

Bibliography

Albidah, A. B., Brevis, W., Fedun, V., Ballai, I., Jess, D. B., Stangalini, M., Higham, J. and Verth, G. (2021), 'Proper orthogonal and dynamic mode decomposition of sunspot data', *Philosophical Transactions of the Royal Society of London Series A* **379**(2190), 20200181.

Albidah, A. B., Fedun, V., Aldhafeeri, A. A., Ballai, I., Brevis, W., Jess, D. B., Higham, J., Stangalini, M., Silva, S. S. A. and Verth, G. (2022), 'Magnetohydrodynamic Wave Mode Identification in Circular and Elliptical Sunspot Umbrae: Evidence for High-order Modes', *Astrophys. J.* **927**(2), 201.

Albidah, A. B., Fedun, V., Aldhafeeri, A. A., Ballai, I., Jess, D. B., Brevis, W., Higham, J., Stangalini, M., Silva, S. S. A., MacBride, C. D. and Verth, G. (2023*a*), 'The Temporal and Spatial Evolution of Magnetohydrodynamic Wave Modes in Sunspots', *Astrophys. J.* **954**(1), 30.

Albidah, A. B., Fedun, V., Aldhafeeri, A. A., Ballai, I., Jess, D. B., Brevis, W., Higham, J., Stangalini, M., Silva, S. S. A., MacBride, C. D. and Verth, G. (2023*b*), 'The temporal and spatial evolution of MHD wave modes in sunspots', *arXiv e-prints* p. arXiv:2305.19418.

Alfvén, H. (1942), 'Existence of Electromagnetic-Hydrodynamic Waves', *Nature* **150**(3805), 405–406.

Alfvén, H. (1947), 'Magneto hydrodynamic waves, and the heating of the solar corona', *Mon. Not. Roy. Astron. Soc.* **107**, 211.

Alharbi, A., Ballai, I., Fedun, V. and Verth, G. (2021), 'Slow magnetoacoustic waves in gravitationally stratified two-fluid plasmas in strongly ionized limit', *Mon. Not. Roy. Astron. Soc.* **501**(2), 1940–1950.

Anfinogentov, S., Nisticò, G. and Nakariakov, V. M. (2013), 'Decay-less kink oscillations in coronal loops', *Astron. Astrophys.* **560**, A107.

Antolin, P., Yokoyama, T. and Van Doorsselaere, T. (2014), 'Fine Strand-like Structure in the Solar Corona from Magnetohydrodynamic Transverse Oscillations', *Astrophys. J. Lett.* **787**(2), L22.

Aschwanden, M. J., Fletcher, L., Schrijver, C. J. and Alexander, D. (1999*a*), 'Coronal Loop Oscillations Observed with the Transition Region and Coronal Explorer', *Astrophys. J.* **520**(2), 880–894.

Aschwanden, M. J., Fletcher, L., Schrijver, C. J. and Alexander, D. (1999*b*), 'Coronal Loop Oscillations Observed with the Transition Region and Coronal Explorer', *Astrophys. J.* **520**(2), 880–894.

Aschwanden, M. J. and Nhalil, N. V. (2023), 'The universality of power law slopes in the solar photosphere and transition region observed with HMI and IRIS', *Frontiers in Astronomy and Space Sciences* **10**, 1099346.

Avrett, E. H. and Loeser, R. (2008), 'Models of the Solar Chromosphere and Transition Region from SUMER and HRTS Observations: Formation of the Extreme-Ultraviolet Spectrum of Hydrogen, Carbon, and Oxygen', *Astrophys. J. Suppl.* **175**(1), 229–276.

Ballai, I., Erdélyi, R. and Hargreaves, J. (2006), 'Slow magnetohydrodynamic waves in stratified and viscous plasmas', *Physics of Plasmas* **13**(4), 042108.

Ballai, I., Forgács-Dajka, E. and Marcu, A. (2019), 'Dispersive shock waves in partially ionised plasmas', *Advances in Space Research* **63**(4), 1472–1482.

Ballai, I., Oliver, R. and Alexandrou, M. (2015), 'Dissipative instability in partially ionised prominence plasmas', *Astron. Astrophys.* **577**, A82.

Ballai, I., Pintér, B., Oliver, R. and Alexandrou, M. (2017), 'Dissipative instability in a partially ionised prominence plasma slab', *Astron. Astrophys.* **603**, A78.

Ballester, J. L., Alexeev, I., Collados, M., Downes, T., Pfaff, R. F., Gilbert, H., Khodachenko, M., Khomenko, E., Shaikhislamov, I. F., Soler, R., Vázquez-Semadeni, E. and Zaqarashvili, T. (2018), 'Partially Ionized Plasmas in Astrophysics', *Space Sci. Rev.* **214**(2), 58.

Bate, W., Jess, D. B., Nakariakov, V. M., Grant, S. D. T., Jafarzadeh, S., Stangalini, M., Keys, P. H., Christian, D. J. and Keenan, F. P. (2022), 'High-frequency Waves in Chromospheric Spicules', *Astrophys. J.* **930**(2), 129.

Bellot Rubio, L. and Orozco Suárez, D. (2019), 'Quiet Sun magnetic fields: an observational view', *Living Reviews in Solar Physics* **16**(1), 1.

Biermann, L. (1946), 'Zur Deutung der chromosphärischen Turbulenz und des Exzesses der UV-Strahlung der Sonne', *Naturwissenschaften* **33**(4), 118–119.

Braginskii, S. I. (1965), 'Transport Processes in a Plasma', *Reviews of Plasma Physics* **1**, 205.

Browning, P. K. and Priest, E. R. (1984), 'Kelvin-Helmholtz instability of a phased-mixed Alfven wave', *Astron. Astrophys.* **131**(2), 283–290.

Brueckner, G. E. and Bartoe, J. D. F. (1983), 'Observations of high-energy jets in the corona above the quiet sun, the heating of the corona, and the acceleration of the solar wind', *Astrophys. J.* **272**, 329–348.

Cally, P. S. and Andries, J. (2010), 'Resonant Absorption as Mode Conversion?', *Solar Phys.* **266**(1), 17–38.

Cargill, P. J., De Moortel, I. and Kiddie, G. (2016), 'Coronal Density Structure and its Role in Wave Damping in Loops', *Astrophys. J.* **823**(1), 31.

Carlsson, M., De Pontieu, B. and Hansteen, V. H. (2019), 'New View of the Solar Chromosphere', *Ann. Rev. Astron. Astrophys.* **57**, 189–226.

Carlsson, M. and Stein, R. F. (1992), 'Non-LTE Radiating Acoustic Shocks and CA II K2V Bright Points', *Astrophys. J. Lett.* **397**, L59.

Chae, J., Cho, K., Lim, E.-K. and Kang, J. (2022), 'Propagating Alfvénic Waves Observed in the Chromosphere around a Small Sunspot: Tales of 3-minute Waves and 10-minute Waves', *Astrophys. J.* **933**(1), 108.

Chmielewski, P., Srivastava, A. K., Murawski, K. and Musielak, Z. E. (2014), 'Impulsively Generated Linear and Non-linear Alfven Waves in the Coronal Funnels', *Acta Physica Polonica A* **125**, 158–164.

Courant, R., Friedrichs, K. and Lewy, H. (1928), 'Über die partiellen differenzengleichungen der mathematischen physik', *Mathematische Annalen* **100**, 32–74.

Cranmer, S. R. and van Ballegooijen, A. A. (2005), 'On the Generation, Propagation, and Reflection of Alfvén Waves from the Solar Photosphere to the Distant Heliosphere', *Astrophys. J. Suppl.* **156**(2), 265–293.

Cranmer, S. R., van Ballegooijen, A. A. and Edgar, R. J. (2007), 'Self-consistent Coronal Heating and Solar Wind Acceleration from Anisotropic Magnetohydrodynamic Turbulence', *Astrophys. J. Suppl.* **171**(2), 520–551.

Danilovic, S. (2017), 'Simulating Ellerman bomb-like events', *Astron. Astrophys.* **601**, A122.

Davila, J. M. (1987), 'Heating of the Solar Corona by the Resonant Absorption of Alfven Waves', *Astrophys. J.* **317**, 514.

de la Cruz Rodríguez, J. and van Noort, M. (2017), 'Radiative Diagnostics in the Solar Photosphere and Chromosphere', *Space Sci. Rev.* **210**(1-4), 109–143.

De Moortel, I., Hood, A. W., Ireland, J. and Arber, T. D. (1999), 'Phase mixing of Alfvén waves in a stratified and open atmosphere', *Astron. Astrophys.* **346**, 641–651.

De Pontieu, B., Martens, P. C. H. and Hudson, H. S. (2001), 'Chromospheric Damping of Alfvén Waves', *Astrophys. J.* **558**(2), 859–871.

de Pontieu, B., McIntosh, S., Hansteen, V. H., Carlsson, M., Schrijver, C. J., Tarbell, T. D., Title, A. M., Shine, R. A., Suematsu, Y., Tsuneta, S., Katsukawa, Y., Ichimoto, K., Shimizu, T. and Nagata, S. (2007), 'A Tale of Two Spicules: The Impact of Spicules on the Magnetic Chromosphere', *Pub. Astron. Soc. Japan* **59**, S655.

Delaboudinière, J. P., Artzner, G. E., Brunaud, J., Gabriel, A. H., Hochedez, J. F., Millier, F., Song, X. Y., Au, B., Dere, K. P., Howard, R. A., Kreplin, R., Michels, D. J., Moses, J. D., Defise, J. M., Jamar, C., Rochus, P., Chauvineau, J. P., Marioge, J. P., Catura, R. C., Lemen, J. R., Shing, L., Stern, R. A., Gurman, J. B., Neupert, W. M., Maucherat, A., Clette, F., Cugnon, P. and Van Dessel, E. L. (1995), 'EIT: Extreme-Ultraviolet Imaging Telescope for the SOHO Mission', *Solar Phys.* **162**(1-2), 291–312.

Díaz-Suárez, S. and Soler, R. (2024), 'Numerical simulations of turbulence in prominence threads induced by torsional oscillations', *Astron. Astrophys.* **684**, A13.

Ebadi, H. and Hosseinpour, M. (2013), 'Phase mixing of standing Alfvén waves with shear flows in solar spicules', *Astrophys. Space Sci.* **343**(1), 11–17.

Edlén, B. (1945), 'The identification of the coronal lines (George Darwin Lecture)', *Mon. Not. Roy. Astron. Soc.* **105**, 323.

Erdélyi, R. and Ballai, I. (2007), 'Heating of the solar and stellar coronae: a review', *Astronomische Nachrichten* **328**(8), 726–733.

Erdélyi, R., Ballai, I. and Ruderman, M. S. (1999), Strongly Nonlinear Resonant MHD Waves in the Steady Solar Magnetic Canopy, *in* A. Wilson and et al., eds, 'Magnetic Fields and Solar Processes', Vol. 9 of *ESA Special Publication*, p. 263.

Euler, L. (1768), *Institutionum Calculi integralis, 1.*

Evans, D. J. and Roberts, B. (1990), 'The Oscillations of a Magnetic Flux Tube and Its Application to Sunspots', *Astrophys. J.* **348**, 346.

Fang, C., Tang, Y. H., Xu, Z., Ding, M. D. and Chen, P. F. (2006), 'Spectral Analysis of Ellerman Bombs', *Astrophys. J.* **643**(2), 1325–1336.

Fontenla, J. M., Avrett, E. H. and Loeser, R. (1993), 'Energy Balance in the Solar Transition Region. III. Helium Emission in Hydrostatic, Constant-Abundance Models with Diffusion', *Astrophys. J.* **406**, 319.

Forteza, P., Oliver, R., Ballester, J. L. and Khodachenko, M. L. (2007), 'Damping of oscillations by ion-neutral collisions in a prominence plasma', *Astron. Astrophys.* **461**(2), 731–739.

Gafeira, R., Lagg, A., Solanki, S. K., Jafarzadeh, S., van Noort, M., Barthol, P., Blanco Rodríguez, J., del Toro Iniesta, J. C., Gandorfer, A., Gizon, L., Hirzberger, J., Knölker, M., Orozco Suárez, D., Riethmüller, T. L. and Schmidt, W. (2017), 'Morphological Properties of Slender Ca II H Fibrils Observed by SUNRISE II', *Astrophys. J. Suppl.* **229**(1), 6.

Goossens, M., Erdélyi, R. and Ruderman, M. S. (2011), 'Resonant MHD Waves in the Solar Atmosphere', *Space Sci. Rev.* **158**(2-4), 289–338.

Goossens, M. and Ruderman, M. S. (1995), 'Conservation laws and connection formulae for resonant MHD waves', *Physica Scripta Volume T* **60**, 171–184.

Goossens, M., Ruderman, M. S. and Hollweg, J. V. (1995), 'Dissipative MHD solutions for resonant AlfvÉn waves in 1-dimensional magnetic flux tubes', *Solar Phys.* **157**(1-2), 75–102.

Göppert-Mayer, M. (2009), 'Elementary processes with two quantum transitions', *Annalen der Physik* **521**(7-8), 466–479.

Gosling, J. T., Tian, H. and Phan, T. (2011), Pulsed Alfvén Waves in the Solar Wind, *in* 'AGU Fall Meeting Abstracts', Vol. 2011, pp. SH11C–08.

Grant, S. D. T., Jess, D. B., Zaqarashvili, T. V., Beck, C., Socas-Navarro, H., Aschwanden, M. J., Keys, P. H., Christian, D. J., Houston, S. J. and Hewitt, R. L. (2018), 'Alfvén wave dissipation in the solar chromosphere', *Nature Physics* **14**(5), 480–483.

Grotrian, W. (1939), 'Zur Frage der Deutung der Linien im Spektrum der Sonnenkorona', *Naturwissenschaften* **27**(13), 214–214.

Gudiksen, B., Carlsson, M., Hansteen, V., Hayek, W., Leenaarts, J. and Martínez-Sykora, J. (2011), 'The stellar atmosphere simulation code bifrost', *Astronomy & Astrophysics - ASTRON ASTROPHYS* **531**.

Guo, M., Van Doorsselaere, T., Karampelas, K. and Li, B. (2019), 'Wave Heating in Simulated Multistranded Coronal Loops', *Astrophys. J.* **883**(1), 20.

Hansteen, V. H., Archontis, V., Pereira, T. M. D., Carlsson, M., Rouppe van der Voort, L. and Leenaarts, J. (2017), 'Bombs and Flares at the Surface and Lower Atmosphere of the Sun', *Astrophys. J.* **839**(1), 22.

Hansteen, V., Ortiz, A., Archontis, V., Carlsson, M., Pereira, T. M. D. and Bjørgen, J. P. (2019), 'Ellerman bombs and UV bursts: transient events in chromospheric current sheets', *Astron. Astrophys.* **626**, A33.

He, J. S., Tu, C. Y., Marsch, E., Guo, L. J., Yao, S. and Tian, H. (2009), 'Upward propagating high-frequency Alfvén waves as identified from dynamic wave-like spicules observed by SOT on Hinode', *Astron. Astrophys.* **497**(2), 525–535.

Heyvaerts, J. and Priest, E. R. (1983), 'Coronal heating by phase-mixed shear Alfven waves.', *Astron. Astrophys.* **117**, 220–234.

Heyvaerts, J. and Priest, E. R. (1984), 'Coronal heating by reconnection in DC current systems - A theory based on Taylor's hypothesis', *Astron. Astrophys.* **137**(1), 63–78.

Hillier, A., Arregui, I. and Matsumoto, T. (2024), 'Nonlinear Wave Damping by Kelvin–Helmholtz Instability-induced Turbulence', *Astrophys. J.* **966**(1), 68.

Hillier, A., Barker, A., Arregui, I. and Latter, H. (2019), 'On Kelvin-Helmholtz and parametric instabilities driven by coronal waves', *Mon. Not. Roy. Astron. Soc.* **482**(1), 1143–1153.

Hillier, A., Isobe, H., Shibata, K. and Berger, T. (2011), 'Numerical Simulations of the Magnetic Rayleigh-Taylor Instability in the Kippenhahn-Schlüter Prominence Model', *Astrophys. J. Lett.* **736**(1), L1.

Hillier, A., Matsumoto, T. and Ichimoto, K. (2017), 'Investigating prominence turbulence with Hinode SOT Dopplergrams', *Astron. Astrophys.* **597**, A111.

Hillier, A., Morton, R. J. and Erdélyi, R. (2013), 'A Statistical Study of Transverse Oscillations in a Quiescent Prominence', *Astrophys. J. Lett.* **779**(2), L16.

Hillier, A. S. (2024), 'On the ambipolar diffusion formulation for ion-neutral drifts in the non-negligible drift velocity limit', *Philosophical Transactions of the Royal Society of London Series A* **382**(2272), 20230229.

Holweger, H. and Mueller, E. A. (1974), 'The Photospheric Barium Spectrum: Solar Abundance and Collision Broadening of Ba II Lines by Hydrogen', *Solar Phys.* **39**(1), 19–30.

Hood, A. W., Brooks, S. J. and Wright, A. N. (2002), 'Coronal heating by the phase mixing of individual pulses propagating in coronal holes', *Proceedings of the Royal Society of London Series A* **458**(2026), 2307.

Hood, A. W., Ireland, J. and Priest, E. R. (1997), 'Heating of coronal holes by phase mixing.', *Astron. Astrophys.* **318**, 957–962.

Hoskin, M., Union, I. A., of the History, I. U. and of Science, P. (1900), *The General History of Astronomy*, number v. 2, pt. 1 *in* 'The General History of Astronomy', Cambridge University Press.
URL: *https://books.google.co.uk/books?id=qrRz-sXyXJYC*

Howard, R. (1959), 'Observations of Solar Magnitic Fields.', *Astrophys. J.* **130**, 193.

Howson, T. A., De Moortel, I. and Antolin, P. (2017*a*), 'Energetics of the Kelvin-Helmholtz instability induced by transverse waves in twisted coronal loops', *Astron. Astrophys.* **607**, A77.

Howson, T. A., De Moortel, I. and Antolin, P. (2017*b*), 'The effects of resistivity and viscosity on the Kelvin- Helmholtz instability in oscillating coronal loops', *Astron. Astrophys.* **602**, A74.

Howson, T. A., De Moortel, I. and Antolin, P. (2017*c*), 'The effects of resistivity and viscosity on the Kelvin- Helmholtz instability in oscillating coronal loops', *Astron. Astrophys.* **602**, A74.

Hudson, H. S. (1991), 'Solar flares, microflares, nanoflares, and coronal heating', *Solar Phys.* **133**(2), 357–369.

Ionson, J. A. (1978), 'Resonant absorption of Alfvénic surface waves and the heating of solar coronal loops.', *Astrophys. J.* **226**, 650–673.

Ireland, J. and Priest, E. R. (1997), 'Phase-mixing in Dissipative Alfvén Waves', *Solar Phys.* **173**(1), 31–51.

Jafarzadeh, S., Solanki, S. K., Stangalini, M., Steiner, O., Cameron, R. H. and Danilovic, S. (2017), 'High-frequency Oscillations in Small Magnetic Elements Observed with Sunrise/SuFI', *Astrophys. J. Suppl.* **229**(1), 10.

Jafarzadeh, S., Wedemeyer, S., Szydlarski, M., De Pontieu, B., Rezaei, R. and Carlsson, M. (2019), 'The solar chromosphere at millimetre and ultraviolet wavelengths. I. Radiation temperatures and a detailed comparison', *Astron. Astrophys.* **622**, A150.

Jess, D. B., Mathioudakis, M., Erdélyi, R., Crockett, P. J., Keenan, F. P. and Christian, D. J. (2009*a*), 'Alfvén Waves in the Lower Solar Atmosphere', *Science* **323**(5921), 1582.

Jess, D. B., Mathioudakis, M., Erdélyi, R., Crockett, P. J., Keenan, F. P. and Christian, D. J. (2009*b*), 'Alfvén Waves in the Lower Solar Atmosphere', *Science* **323**(5921), 1582.

Joshi, J., Rouppe van der Voort, L. H. M. and de la Cruz Rodríguez, J. (2020), 'Signatures of ubiquitous magnetic reconnection in the lower solar atmosphere', *Astron. Astrophys.* **641**, L5.

Judge, P., Kleint, L., Casini, R., de Wijn, A. G., Schad, T. and Tritschler, A. (2024), 'Magnetic Fields and Plasma Heating in the Sun's Atmosphere', *Astrophys. J.* **960**(2), 129.

Karampelas, K. and Van Doorsselaere, T. (2024), 'Decayless oscillations in 3D coronal loops excited by a power-law driver', *Astron. Astrophys.* **681**, L6.

Karampelas, K., Van Doorsselaere, T. and Antolin, P. (2017), 'Heating by transverse waves in simulated coronal loops', *Astron. Astrophys.* **604**, A130.

Karpen, J. T., Dahlburg, R. B. and Davila, J. M. (1994), 'The Effects of Kelvin-Helmholtz Instability on Resonance Absorption Layers in Coronal Loops', *Astrophys. J.* **421**, 372.

Keller, C. U., Schüssler, M., Vögler, A. and Zakharov, V. (2004), 'On the Origin of Solar Faculae', *Astrophys. J. Lett.* **607**(1), L59–L62.

Khomenko, E. and Collados, M. (2012), 'Heating of the Magnetized Solar Chromosphere by Partial Ionization Effects', *Astrophys. J.* **747**(2), 87.

Khomenko, E., Collados, M., Díaz, A. and Vitas, N. (2014), 'Fluid description of multi-component solar partially ionized plasma', *Physics of Plasmas* **21**(9), 092901.

Khomenko, E., Collados, M., Vitas, N. and González-Morales, P. A. (2021), 'Influence of ambipolar and Hall effects on vorticity in three-dimensional simulations of magneto-convection', *Philosophical Transactions of the Royal Society of London Series A* **379**(2190), 20200176.

Khomenko, E., Vitas, N., Collados, M. and de Vicente, A. (2018), 'Three-dimensional simulations of solar magneto-convection including effects of partial ionization', *Astron. Astrophys.* **618**, A87.

Klimchuk, J. A. (2006), 'On Solving the Coronal Heating Problem', *Solar Phys.* **234**(1), 41–77.

Kraskiewicz, J., Murawski, K., Zhang, F. and Poedts, S. (2023), 'Monochromatic Two-Fluid Alfvén Waves in the Partially Ionised Solar Chromosphere', *Solar Phys.* **298**(1), 11.

Kumar, M., Murawski, K., Kadowaki, L., Kuźma, B. and Kilpua, E. K. J. (2024), 'Impulsively generated waves in two-fluid plasma in the solar chromosphere: Heating and generation of plasma outflows', *Astron. Astrophys.* **681**, A60.

Kuźma, B., Wójcik, D., Murawski, K., Yuan, D. and Poedts, S. (2020), 'Numerical simulations of the lower solar atmosphere heating by two-fluid nonlinear Alfvén waves', *Astron. Astrophys.* **639**, A45.

Leenaarts, J., Carlsson, M. and Rouppe van der Voort, L. (2012), 'The Formation of the Hα Line in the Solar Chromosphere', *Astrophys. J.* **749**(2), 136.

Leenaarts, J., Carlsson, M. and Rouppe van der Voort, L. (2015), 'On Fibrils and Field Lines: the Nature of Hα Fibrils in the Solar Chromosphere', *Astrophys. J.* **802**(2), 136.

Leenaarts, J., de la Cruz Rodríguez, J., Danilovic, S., Scharmer, G. and Carlsson, M. (2018), 'Chromospheric heating during flux emergence in the solar atmosphere', *Astron. Astrophys.* **612**, A28.

Leighton, R. B. (1959), 'Observations of Solar Magnetic Fields in Plage Regions.', *Astrophys. J.* **130**, 366.

Lighthill, M. J. (1952), 'On Sound Generated Aerodynamically. I. General Theory', *Proceedings of the Royal Society of London Series A* **211**(1107), 564–587.

Lites, B. W., Rutten, R. J. and Kalkofen, W. (1993), 'Dynamics of the Solar Chromosphere. I. Long-Period Network Oscillations', *Astrophys. J.* **414**, 345.

Lockyer, J. (1869), 'The Recent Total Eclipse of the Sun', *Nature* **1**, 14–15.

Lodders, K. (2003), 'Solar System Abundances and Condensation Temperatures of the Elements', *Astrophys. J.* **591**(2), 1220–1247.

Magyar, N. and Van Doorsselaere, T. (2016), 'Damping of nonlinear standing kink oscillations: a numerical study', *Astron. Astrophys.* **595**, A81.

Magyar, N., Van Doorsselaere, T. and Goossens, M. (2017), 'Generalized phase mixing: Turbulence-like behaviour from unidirectionally propagating MHD waves', *Scientific Reports* **7**, 14820.

Martínez-Gómez, D., Soler, R. and Terradas, J. (2017), 'Multi-fluid Approach to High-frequency Waves in Plasmas. II. Small-amplitude Regime in Partially Ionized Media', *Astrophys. J.* **837**(1), 80.

Martinez-Sykora, J., De Pontieu, B., Hansteen, V. and Carlsson, M. (2015), 'The role of partial ionization effects in the chromosphere', *Philosophical Transactions of the Royal Society of London Series A* **373**(2042), 20140268–20140268.

Martínez-Sykora, J., Hansteen, V. and Moreno-Insertis, F. (2011), 'On the Origin of the Type II Spicules: Dynamic Three-dimensional MHD Simulations', *Astrophys. J.* **736**(1), 9.

Martínez-Sykora, J., Pontieu, B. D., Hansteen, V. H., van der Voort, L. R., Carlsson, M. and Pereira, T. M. D. (2017), 'On the generation of solar spicules and alfvénic waves', *Science* **356**(6344), 1269–1272.
URL: *https://www.science.org/doi/abs/10.1126/science.aah5412*

Mather, J. F., Ballai, I. and Erdélyi, R. (2018), 'Dissipative instabilities in a partially ionised prominence plasma slab. II. The effect of compressibility', *Astron. Astrophys.* **610**, A56.

Matthaeus, W. H., Zank, G. P., Oughton, S., Mullan, D. J. and Dmitruk, P. (1999), 'Coronal Heating by Magnetohydrodynamic Turbulence Driven by Reflected Low-Frequency Waves', *Astrophys. J. Lett.* **523**(1), L93–L96.

McIntosh, S. W., de Pontieu, B., Carlsson, M., Hansteen, V., Boerner, P. and Goossens, M. (2011), 'Alfvénic waves with sufficient energy to power the quiet solar corona and fast solar wind', *Nature* **475**(7357), 477–480.

McLaughlin, J. A., de Moortel, I. and Hood, A. W. (2011), 'Phase mixing of nonlinear visco-resistive Alfvén waves', *Astron. Astrophys.* **527**, A149.

McMurdo, M., Ballai, I., Verth, G., Alharbi, A. and Fedun, V. (2023), 'Phase Mixing of Propagating Alfvén Waves in a Single-fluid Partially Ionized Solar Plasma', *Astrophys. J.* **958**(1), 81.

Melis, L., Soler, R. and Ballester, J. L. (2021), 'Alfvén wave heating in partially ionized thin threads of solar prominences', *Astron. Astrophys.* **650**, A45.

Melis, L., Soler, R. and Terradas, J. (2023), 'Self-consistent equilibrium models of prominence thin threads heated by Alfvén waves propagating from the photosphere', *Astron. Astrophys.* **676**, A25.

Mignone, A., Bodo, G., Massaglia, S., Matsakos, T., Tesileanu, O., Zanni, C. and Ferrari, A. (2007), 'PLUTO: A Numerical Code for Computational Astrophysics', *Astrophys. J. Suppl.* **170**(1), 228–242.

Mocanu, G., Marcu, A., Ballai, I. and Orza, B. (2008), 'The problem of phase mixed shear Alfvén waves in the solar corona revisited', *Astronomische Nachrichten* **329**(8), 780.

Morton, R. J., Erdélyi, R., Jess, D. B. and Mathioudakis, M. (2011), 'Observations of Sausage Modes in Magnetic Pores', *Astrophys. J. Lett.* **729**(2), L18.

Morton, R. J., Tomczyk, S. and Pinto, R. (2015), 'Investigating Alfvénic wave propagation in coronal open-field regions', *Nature Communications* **6**, 7813.

Morton, R. J., Tomczyk, S. and Pinto, R. F. (2016), 'A Global View of Velocity Fluctuations in the Corona below 1.3 R $_{\odot}$ with CoMP', *Astrophys. J.* **828**(2), 89.

Morton, R. J., Verth, G., Hillier, A. and Erdélyi, R. (2014), 'The Generation and Damping of Propagating MHD Kink Waves in the Solar Atmosphere', *Astrophys. J.* **784**(1), 29.

Mumford, S. J., Fedun, V. and Erdélyi, R. (2015), 'Generation of Magnetohydrodynamic Waves in Low Solar Atmospheric Flux Tubes by Photospheric Motions', *Astrophys. J.* **799**(1), 6.

Nelson, C. J., Freij, N., Reid, A., Oliver, R., Mathioudakis, M. and Erdélyi, R. (2017), 'IRIS Burst Spectra Co-spatial to a Quiet-Sun Ellerman-like Brightening', *Astrophys. J.* **845**(1), 16.

Nisticò, G., Nakariakov, V. M. and Verwichte, E. (2013), 'Decaying and decayless transverse oscillations of a coronal loop', *Astron. Astrophys.* **552**, A57.

Nóbrega-Siverio, D., Martínez-Sykora, J., Moreno-Insertis, F. and Carlsson, M. (2020), 'Ambipolar diffusion in the Bifrost code', *Astron. Astrophys.* **638**, A79.

Ofman, L., Davila, J. M. and Steinolfson, R. S. (1994), 'Nonlinear studies of coronal heating by the resonant absorption of Alfvén waves', *Geophys. Res. Lett.* **21**(20), 2259–2262.

Ofman, L., Klimchuk, J. A. and Davila, J. M. (1998), 'A Self-consistent Model for the Resonant Heating of Coronal Loops: The Effects of Coupling with the Chromosphere', *Astrophys. J.* **493**(1), 474–479.

O'Gorman, E., Kervella, P., Harper, G. M., Richards, A. M. S., Decin, L., Montargès, M. and McDonald, I. (2017), 'The inhomogeneous submillimeter atmosphere of Betelgeuse', *Astron. Astrophys.* **602**, L10.

Okamoto, T. J. and De Pontieu, B. (2011), 'Propagating Waves Along Spicules', *Astrophys. J. Lett.* **736**(2), L24.

Oppenheim, M., Dimant, Y., Longley, W. and Fletcher, A. C. (2020), 'Newly Discovered Source of Turbulence and Heating in the Solar Chromosphere', *Astrophys. J. Lett.* **891**(1), L9.

Osterbrock, D. E. (1961), 'The Heating of the Solar Chromosphere, Plages, and Corona by Magnetohydrodynamic Waves.', *Astrophys. J.* **134**, 347.

Pagano, P. and De Moortel, I. (2017), 'Contribution of mode-coupling and phase-mixing of Alfvén waves to coronal heating', *Astron. Astrophys.* **601**, A107.

Parnell, C. E. and De Moortel, I. (2012), 'A contemporary view of coronal heating', *Philosophical Transactions of the Royal Society of London Series A* **370**(1970), 3217–3240.

Pascoe, D. J., Wright, A. N., De Moortel, I. and Hood, A. W. (2015), 'Excitation and damping of broadband kink waves in the solar corona', *Astron. Astrophys.* **578**, A99.

Patsourakos, S. and Vial, J.-C. (2002), 'Soho Contribution to Prominence Science', *Solar Phys.* **208**(2), 253–281.

Pelekhata, M., Murawski, K. and Poedts, S. (2023), 'Generation of solar chromosphere heating and coronal outflows by two-fluid waves', *Astron. Astrophys.* **669**, A47.

Popescu Braileanu, B. and Keppens, R. (2021), 'Effects of ambipolar diffusion on waves in the solar chromosphere', *Astron. Astrophys.* **653**, A131.

Priest, E. (2014), *Magnetohydrodynamics of the Sun*, Cambridge University Press.

Prokopyszyn, A. P. K. and Hood, A. W. (2019), 'Investigating the damping rate of phase-mixed Alfvén waves', *Astron. Astrophys.* **632**, A93.

Prokopyszyn, A. P. K., Hood, A. W. and De Moortel, I. (2019), 'Phase mixing of nonlinear Alfvén waves', *Astron. Astrophys.* **624**, A90.

Rezaei, R., Bello González, N. and Schlichenmaier, R. (2012), 'The formation of sunspot penumbra. Magnetic field properties', *Astron. Astrophys.* **537**, A19.

Roberts, B. (1979), 'Spicules: The resonant response to granular buffeting?', *Solar Phys.* **61**(1), 23–34.

Rouppe van der Voort, L. H. M., Rutten, R. J. and Vissers, G. J. M. (2016), 'Reconnection brightenings in the quiet solar photosphere', *Astron. Astrophys.* **592**, A100.

Ruderman, M. S., Nakariakov, V. M. and Roberts, B. (1998), 'Alfven wave phase mixing in two-dimensional open magnetic configurations.', *Astron. Astrophys.* **338**, 1118–1124.

Ruderman, M. S. and Petrukhin, N. S. (2018), 'Phase mixing of Alfvén waves in two-dimensional magnetic plasma configurations with exponentially decreasing density', *Astron. Astrophys.* **620**, A44.

Ruderman, M. S. and Roberts, B. (2002), 'The Damping of Coronal Loop Oscillations', *Astrophys. J.* **577**(1), 475–486.

Russell, A. J. B. and Fletcher, L. (2013), 'Propagation of Alfvénic Waves from Corona to Chromosphere and Consequences for Solar Flares', *Astrophys. J.* **765**(2), 81.

Rutten, R. J., Vissers, G. J. M., Rouppe van der Voort, L. H. M., Sütterlin, P. and Vitas, N. (2013), Ellerman bombs: fallacies, fads, usage, *in* 'Journal of Physics Conference Series', Vol. 440 of *Journal of Physics Conference Series*, IOP, p. 012007.

Sakurai, T., Goossens, M. and Hollweg, J. V. (1991*a*), 'Resonant Behaviour of Magnetohydrodynamic Waves on Magnetic Flux Tubes - Part One', *Solar Phys.* **133**(2), 227–245.

Sakurai, T., Goossens, M. and Hollweg, J. V. (1991*b*), 'Resonant Behaviour of Magnetohydrodynamic Waves on Magnetic Flux Tubes II. Absorption of Sound Waves by Sunspots', *Solar Phys.* **133**(2), 247–262.

Sarp Yalim, M., Prasad, A., Pogorelov, N., Zank, G. and Hu, Q. (2020), 'Effects of Cowling Resistivity in the Weakly-Ionized Chromosphere', *arXiv e-prints* p. arXiv:2007.12275.

Schlichenmaier, R., von der Lühe, O., Hoch, S., Soltau, D., Berkefeld, T., Schmidt, D., Schmidt, W., Denker, C., Balthasar, H., Hofmann, A., Strassmeier, K. G., Staude, J., Feller, A., Lagg, A., Solanki, S. K., Collados, M., Sigwarth, M., Volkmer, R., Waldmann, T., Kneer, F., Nicklas, H. and Sobotka, M. (2016), 'Active region fine structure observed at 0.08 arcsec resolution', *Astron. Astrophys.* **596**, A7.

Schwarzschild, M. (1948), 'On Noise Arising from the Solar Granulation.', *Astrophys. J.* **107**, 1.

Scudder, J. D. (1996), 'Dreicer order ambipolar electric fields at Parker's steady state solar wind sonic critical point', *J. Geophys. Res.* **101**(A6), 13461–13472.

Scudder, J. D. (1997), 'Theoretical Approaches to the Description of Magnetic Merging: The Need for Finite βe, Anisotropic, Ambipolar Hall MHD', *Space Sci. Rev.* **80**, 235–267.

Shelyag, S., Khomenko, E., de Vicente, A. and Przybylski, D. (2016), 'Heating of the Partially Ionized Solar Chromosphere by Waves in Magnetic Structures', *Astrophys. J. Lett.* **819**(1), L11.

Shelyag, S., Mathioudakis, M. and Keenan, F. P. (2012), 'Mechanisms for MHD Poynting Flux Generation in Simulations of Solar Photospheric Magnetoconvection', *Astrophys. J. Lett.* **753**(1), L22.

Shimizu, T. (1995), 'Energetics and Occurrence Rate of Active-Region Transient Brightenings and Implications for the Heating of the Active-Region Corona', *Pub. Astron. Soc. Japan* **47**, 251–263.

Smith, P. D., Tsiklauri, D. and Ruderman, M. S. (2007), 'Enhanced phase mixing of Alfvén waves propagating in stratified and divergent coronal structures', *Astron. Astrophys.* **475**(3), 1111–1123.

Sobotka, M., Švanda, M., Jurčák, J., Heinzel, P., Del Moro, D. and Berrilli, F. (2013), 'Dynamics of the solar atmosphere above a pore with a light bridge', *Astron. Astrophys.* **560**, A84.

Solanki, S. K., Barthol, P., Danilovic, S., Feller, A., Gandorfer, A., Hirzberger, J., Riethmüller, T. L., Schüssler, M., Bonet, J. A., Martínez Pillet, V., del Toro Iniesta, J. C., Domingo, V., Palacios, J., Knölker, M., Bello González, N., Berkefeld, T., Franz, M., Schmidt, W. and Title, A. M. (2010), 'SUNRISE: Instrument, Mission, Data, and First Results', *Astrophys. J. Lett.* **723**(2), L127–L133.

Soler, R., Ballester, J. L. and Zaqarashvili, T. V. (2015), 'Overdamped Alfvén waves due to ion-neutral collisions in the solar chromosphere', *Astron. Astrophys.* **573**, A79.

Soler, R., Carbonell, M., Ballester, J. L. and Terradas, J. (2013), 'Alfvén Waves in a Partially Ionized Two-fluid Plasma', *Astrophys. J.* **767**(2), 171.

Soler, R., Terradas, J., Oliver, R. and Ballester, J. L. (2017), 'Propagation of Torsional Alfvén Waves from the Photosphere to the Corona: Reflection, Transmission, and Heating in Expanding Flux Tubes', *Astrophys. J.* **840**(1), 20.

Srivastava, A. K., Ballester, J. L., Cally, P. S., Carlsson, M., Goossens, M., Jess, D. B., Khomenko, E., Mathioudakis, M., Murawski, K. and Zaqarashvili, T. V. (2021), 'Chromospheric Heating by Magnetohydrodynamic Waves and Instabilities', *Journal of Geophysical Research (Space Physics)* **126**(6), e029097.

Srivastava, A. K. and Singh, B. (2023), 'Numerical Simulations of the Decaying Transverse Oscillations in the Cool Jet', *Physics* **5**(3), 655–671.

Stangalini, M., Erdélyi, R., Boocock, C., Tsiklauri, D., Nelson, C. J., Del Moro, D., Berrilli, F. and Korsós, M. B. (2021), 'Torsional oscillations within a magnetic pore in the solar photosphere', *Nature Astronomy* **5**, 691–696.

Stangalini, M., Giannattasio, F., Erdélyi, R., Jafarzadeh, S., Consolini, G., Criscuoli, S., Ermolli, I., Guglielmino, S. L. and Zuccarello, F. (2017), 'Polarized Kink Waves in Magnetic Elements: Evidence for Chromospheric Helical Waves', *Astrophys. J.* **840**(1), 19.

Stangalini, M., Verth, G., Fedun, V., Aldhafeeri, A. A., Jess, D. B., Jafarzadeh, S., Keys, P. H., Fleck, B., Terradas, J., Murabito, M., Ermolli, I., Soler, R., Giorgi, F. and MacBride, C. D. (2022), 'Large scale coherent magnetohydrodynamic oscillations in a sunspot', *Nature Communications* **13**, 479.

Stein, R. F. (1967), 'Generation of Acoustic and Gravity Waves by Turbulence in an Isothermal Stratified Atmosphere', *Solar Phys.* **2**(4), 385–432.

Stein, R. F. (1968), 'Waves in the Solar Atmosphere. I. The Acoustic Energy Flux.', *Astrophys. J.* **154**, 297.

Stone, J. M., Tomida, K., White, C. J. and Felker, K. G. (2020), 'The athena++ adaptive mesh refinement framework: Design and magnetohydrodynamic solvers', *The Astrophysical Journal Supplement Series* **249**(1), 4.

Thurgood, J. O. and McLaughlin, J. A. (2013), '3D Alfvén wave behaviour about proper and improper magnetic null points', *Astron. Astrophys.* **558**, A127.

Tomczyk, S., McIntosh, S. W., Keil, S. L., Judge, P. G., Schad, T., Seeley, D. H. and Edmondson, J. (2007), 'Alfvén Waves in the Solar Corona', *Science* **317**(5842), 1192.

Tsiklauri, D. (2016), 'Collisionless, phase-mixed, dispersive, Gaussian Alfven pulse in transversely inhomogeneous plasma', *Physics of Plasmas* **23**(12), 122906.

van Ballegooijen, A. A., Asgari-Targhi, M., Cranmer, S. R. and DeLuca, E. E. (2011), 'Heating of the Solar Chromosphere and Corona by Alfvén Wave Turbulence', *Astrophys. J.* **736**(1), 3.

Van Damme, H. J., De Moortel, I., Pagano, P. and Johnston, C. D. (2020), 'Chromospheric evaporation and phase mixing of Alfvén waves in coronal loops', *Astron. Astrophys.* **635**, A174.

van der Holst, B., Sokolov, I. V., Meng, X., Jin, M., Manchester, W. B., I., Tóth, G. and Gombosi, T. I. (2014*a*), 'Alfvén Wave Solar Model (AWSoM): Coronal Heating', *Astrophys. J.* **782**(2), 81.

van der Holst, B., Sokolov, I. V., Meng, X., Jin, M., Manchester, W. B., I., Tóth, G. and Gombosi, T. I. (2014*b*), 'Alfvén Wave Solar Model (AWSoM): Coronal Heating', *Astrophys. J.* **782**(2), 81.

Vernazza, J. E., Avrett, E. H. and Loeser, R. (1981), 'Structure of the solar chromosphere. III. Models of the EUV brightness components of the quiet sun.', *Astrophys. J. Suppl.* **45**, 635–725.

Verth, G., Terradas, J. and Goossens, M. (2010), 'Observational Evidence of Resonantly Damped Propagating Kink Waves in the Solar Corona', *Astrophys. J. Lett.* **718**(2), L102–L105.

Vigeesh, G., Fedun, V., Hasan, S. S. and Erdélyi, R. (2012), 'Three-dimensional Simulations of Magnetohydrodynamic Waves in Magnetized Solar Atmosphere', *Astrophys. J.* **755**(1), 18.

Vissers, G. J. M., Rouppe van der Voort, L. H. M. and Rutten, R. J. (2013), 'Ellerman Bombs at High Resolution. II. Triggering, Visibility, and Effect on Upper Atmosphere', *Astrophys. J.* **774**(1), 32.

Vissers, G. J. M., Rouppe van der Voort, L. H. M. and Rutten, R. J. (2019), 'Automating Ellerman bomb detection in ultraviolet continua', *Astron. Astrophys.* **626**, A4.

Vranjes, J. (2014), 'Viscosity effects on waves in partially and fully ionized plasma in magnetic field', *Mon. Not. Roy. Astron. Soc.* **445**(2), 1614–1624.

Vranjes, J. and Krstic, P. S. (2013), 'Collisions, magnetization, and transport coefficients in the lower solar atmosphere', *Astron. Astrophys.* **554**, A22.

Wang, J., Lee, J., Liu, C., Cao, W. and Wang, H. (2022), 'A High-resolution Study of Magnetic Field Evolution and Spicular Activity around the Boundary of a Coronal Hole', *Astrophys. J.* **924**(2), 137.

Watanabe, H., Vissers, G., Kitai, R., Rouppe van der Voort, L. and Rutten, R. J. (2011), 'Ellerman Bombs at High Resolution. I. Morphological Evidence for Photospheric Reconnection', *Astrophys. J.* **736**(1), 71.

Withbroe, G. L. and Noyes, R. W. (1977), 'Mass and energy flow in the solar chromosphere and corona.', *Ann. Rev. Astron. Astrophys.* **15**, 363–387.

Wójcik, D., Murawski, K., Musielak, Z. E., Konkol, P. and Mignone, A. (2017), 'Numerical Simulations of Torsional Alfvén Waves in Axisymmetric Solar Magnetic Flux Tubes', *Solar Phys.* **292**(2), 31.

Yadav, R., de la Cruz Rodríguez, J., Kerr, G. S., Díaz Baso, C. J. and Leenaarts, J. (2022), 'Radiative losses in the chromosphere during a C-class flare', *Astron. Astrophys.* **665**, A50.

Zaqarashvili, T. V., Carbonell, M., Ballester, J. L. and Khodachenko, M. L. (2012), 'Cut-off wavenumber of Alfvén waves in partially ionized plasmas of the solar atmosphere', *Astron. Astrophys.* **544**, A143.

Zaqarashvili, T. V., Khodachenko, M. L. and Rucker, H. O. (2011), 'Magneto-hydrodynamic waves in solar partially ionized plasmas: two-fluid approach', *Astron. Astrophys.* **529**, A82.

APPENDIX A

Derivation of Equation 2.55

This appendix contains a more detailed derivation of Equation 2.55, with detailed algebraic manipulations. We begin our derivation by incorporating Ohmic diffusion and ambipolar diffusion into the momentum equation. With regards to the induction equation, we assume that the impact of the pressure gradient and gravitational effects can be considered negligible. That means that the length scales over which we consider the phase mixing of Alfvén waves to develop to be smaller than the length scales over which the density, pressure and gravity vary. The non-ideal induction and moment equations are therefore given by

$$\frac{\partial \mathbf{B}}{\partial t} = \nabla \times (\mathbf{v} \times \mathbf{B}) + \eta \nabla^2 \mathbf{B} + \nabla \times \left\{ \frac{\eta_A}{|\mathbf{B}|^2} \left[(\nabla \times \mathbf{B}) \times \mathbf{B} \right] \times \mathbf{B} \right\}, \tag{A.1}$$

and

$$\rho_0 \left(\frac{\partial \mathbf{v}}{\partial t} + \mathbf{v} \cdot \nabla \mathbf{v} \right) = \mathbf{j} \times \mathbf{B} + \rho_0 \zeta \left[\nabla^2 \mathbf{v} + \frac{1}{3} \nabla (\nabla \cdot \mathbf{v}) \right]. \tag{A.2}$$

In the present study we assume a density inhomogeneity across the field and a homogeneous background magnetic field oriented in the z direction. The unidirectional vertical magnetic field has to be constant, as any alteration from this would result in a net Lorentz force in the equilibrium state that is not balanced. For instance, assuming a magnetic field of the form $B_0(x)\hat{\mathbf{z}}$, would result in a force $(B_0/\mu_0)(dB_0/dx)$ oriented in the x direction that is not opposed by any force, so the forces in equilibrium state are not balanced.

Clearly imposing an inhomogeneous background magnetic field does not allow for accurate mathematical progress. Fortunately, we do not have to assume anything about the profile of an inhomogeneous density profile and hence we continue with this setup for all remaining calculations.

Assuming constant equilibrium background quantities, other than the density, and perturbing the system with amplitudes much smaller than the equilibrium quantities, we arrive at the linearised induction and momentum equations

given by

$$\frac{\partial b}{\partial t} = B_0 \frac{\partial v}{\partial z} + \eta \left(\frac{\partial^2 b}{\partial x^2} + \frac{\partial^2 b}{\partial z^2} \right) + \eta_A \frac{\partial^2 b}{\partial z^2}. \tag{A.3}$$

and

$$\frac{\partial v}{\partial t} = \frac{B_0}{\mu_0 \rho_0(x)} \frac{\partial b}{\partial z} + \zeta \left(\frac{\partial^2 v}{\partial x^2} + \frac{\partial^2 v}{\partial z^2} \right). \tag{A.4}$$

In order to solve these coupled equations, we may eliminate either the velocity perturbation or the magnetic field perturbation by differentiating Equation (A.3) with respect to t and differentiating Equations (A.4) with respect to z giving

$$\frac{\partial^2 b}{\partial t^2} = B_0 \frac{\partial^2 v}{\partial z \partial t} + \left(\eta \frac{\partial^2}{\partial x^2} + \eta_C \frac{\partial^2}{\partial z^2} \right) \frac{\partial b}{\partial t}. \tag{A.5}$$

and

$$\frac{\partial^2 v}{\partial z \partial t} = \frac{B_0}{\mu_0 \rho_0(x)} \frac{\partial^2 b}{\partial z^2} + \zeta \left(\frac{\partial^2}{\partial x^2} + \frac{\partial^2}{\partial z^2} \right) \frac{\partial v}{\partial z}. \tag{A.6}$$

Inserting Equation (A.6) into Equation (A.5) we arrive at

$$\frac{\partial^2 b}{\partial t^2} = v_A^2(x) \frac{\partial^2 b}{\partial z^2} + B_0 \zeta \left(\frac{\partial^2}{\partial x^2} + \frac{\partial^2}{\partial z^2} \right) \frac{\partial v}{\partial z} + \left(\eta \frac{\partial^2}{\partial x^2} + \eta_C \frac{\partial^2}{\partial z^2} \right) \frac{\partial b}{\partial t}. \tag{A.7}$$

To remove the dependence of the velocity perturbation, we rearrange Equation (A.3) to give

$$\frac{\partial v}{\partial z} = \frac{1}{B_0} \left(\frac{\partial b}{\partial t} - \eta \frac{\partial^2 b}{\partial x^2} - \eta_C \frac{\partial^2 b}{\partial z^2} \right). \tag{A.8}$$

We then substitute this into Equation (A.7) to give our governing equation for Alfvén waves in partially ionised inhomogeneous plasmas

$$\begin{aligned} \frac{\partial^2 b}{\partial t^2} = v_A^2(x) \frac{\partial^2 b}{\partial z^2} + \left[(\eta + \zeta) \frac{\partial^2}{\partial x^2} + (\eta_C + \zeta) \frac{\partial^2}{\partial z^2} \right] \frac{\partial b}{\partial t} \\ - \zeta \left[\eta \frac{\partial^2}{\partial x^2} + \eta_C \frac{\partial^2}{\partial z^2} \right] \nabla^2 b. \end{aligned} \tag{A.9}$$

One key feature present in the above equation (and often overlooked in applications to solar corona) is the terms proportional to the products of dissipative coefficients. Since we are working in the partially ionised lower solar atmosphere, these terms are large and hence their products have the potential to be not only important but dominant. In our calculations we have also assumed the dissipative coefficients are height independent.

APPENDIX B

Derivation of Equation 2.59

The governing equation given by Equation (2.59) is derived by first linearising the equations of motion for the ionised and neutral fluids given by

$$\frac{\partial v_i}{\partial t} = \frac{B_0}{\mu_0 \rho_i(x)} \frac{\partial b}{\partial z} + \tilde{\nu}_{in}(x)\,(v_n - v_i) + \zeta_i \nabla^2 v_i \tag{B.1}$$

and

$$\frac{\partial v_n}{\partial t} = -\frac{\rho_i(x)}{\rho_n(x)} \tilde{\nu}_{in}(x)\,(v_n - v_i) + \zeta_n \nabla^2 v_n. \tag{B.2}$$

In the above equations the quantities v_i and v_n denote the ion and neutral velocities, respectively, $\rho_i(x)$ and $\rho_n(x)$ denote the ion and neutral mass densities, b is the magnetic field perturbation, while B_0 denotes the constant background magnetic field. $\tilde{\nu}_{in}(x)$ denotes the ion-neutral collisional frequency noting that since the neutral density, $\rho_n(x)$, varies transversally this implies that the ion neutral collisional frequency must also. ζ_i and ζ_n denote the ion and neutral shear viscosity coefficients, whose values are given by Equations (2.39) and (2.40), respectively. Note that here, we have assumed the contribution from electrons to be negligible.

As only the charged particles are influenced by the presence of the magnetic field, the linearised induction equation is given by

$$\frac{\partial b}{\partial t} = B_0 \frac{\partial v_i}{\partial z}. \tag{B.3}$$

We begin by differentiating Equation (B.1) with respect to time twice

$$\frac{\partial^3 v_i}{\partial t^3} = \frac{B_0}{\mu_0 \rho_i(x)} \frac{\partial b}{\partial z \partial t^2} + \tilde{\nu}_{in}(x) \left(\frac{\partial^2 v_n}{\partial t^2} - \frac{\partial^2 v_i}{\partial t^2} \right) + \zeta_i \nabla^2 \frac{\partial^2 v_i}{\partial t^2}. \tag{B.4}$$

In order to solve this equation we need to eliminate two of the three perturbation quantities v_i, v_n or b. We chose to retain only the ion velocity perturbation. Hence, we differentiate Equation (B.3) with respect to z and time giving

$$\frac{\partial^3 b}{\partial z \partial t^2} = B_0 \frac{\partial^3 v_i}{\partial z^2 \partial t}. \tag{B.5}$$

We can then rewrite Equation (B.4) in terms of only the velocity perturbation quantities as

$$\frac{\partial^3 v_i}{\partial t^3} = v_A(x)^2 \frac{\partial^3 v_i}{\partial z^2 \partial t} + \tilde{\nu}_{in}(x) \left(\frac{\partial^2 v_n}{\partial t^2} - \frac{\partial^2 v_i}{\partial t^2} \right) + \zeta_i \nabla^2 \frac{\partial^2 v_i}{\partial t^2}. \tag{B.6}$$

Clearly we need to evaluate the second derivative of v_n with respect to time in order to remove dependence of v_n from our governing equation. The following steps are those required to do so, details are provided at each equation. The second order derivative of the neutral velocity perturbation, seen above, is obtained by differentiating Equation (B.2) with respect to time and is given by

$$\frac{\partial^2 v_n}{\partial t^2} = -\frac{\rho_i(x)}{\rho_n(x)} \tilde{\nu}_{in}(x) \left(\frac{\partial v_n}{\partial t} - \frac{\partial v_i}{\partial t} \right) + \zeta_n \nabla^2 \frac{\partial v_n}{\partial t}. \tag{B.7}$$

We differentiate Equation (B.1) with respect to time, and obtain

$$\frac{\partial^2 v_i}{\partial t^2} = \frac{B_0}{\mu_0 \rho_i(x)} \frac{\partial^2 b}{\partial z \partial t} + \tilde{\nu}_{in}(x) \left(\frac{\partial v_n}{\partial t} - \frac{\partial v_i}{\partial t} \right) + \zeta_i \nabla^2 \frac{\partial v_i}{\partial t}. \tag{B.8}$$

Next, we differentiate Equation (B.3) with respect to z, and obtain

$$\frac{\partial^2 b}{\partial z \partial t} = B_0 \frac{\partial^2 v_i}{\partial z^2}. \tag{B.9}$$

After substituting Equation (B.9) into Equation (B.8), we obtain

$$\frac{\partial^2 v_i}{\partial t^2} = v_A^2(x) \frac{\partial^2 v_i}{\partial z^2} + \tilde{\nu}_{in}(x) \left(\frac{\partial v_n}{\partial t} - \frac{\partial v_i}{\partial t} \right) + \zeta_i \nabla^2 \frac{\partial v_i}{\partial t}. \tag{B.10}$$

We subtract Equation (B.10) from Equation (B.7) and, after some simplifications, we obtain

$$\begin{aligned} \left(\frac{\partial^2 v_n}{\partial t^2} - \frac{\partial^2 v_i}{\partial t^2} \right) = \tilde{\nu}_{in}(x) \left(\frac{\partial v_n}{\partial t} - \frac{\partial v_i}{\partial t} \right) \left(-\frac{\rho_i(x)}{\rho_n(x)} - 1 \right) + \zeta_n \nabla^2 \frac{\partial v_n}{\partial t} - \\ - \zeta_i \nabla^2 \frac{\partial v_i}{\partial t} - v_A^2(x) \frac{\partial^2 v_i}{\partial z^2}. \end{aligned} \tag{B.11}$$

We substitute Equation (B.11) in to Equation (B.6), and obtain

$$\frac{\partial^3 v_i}{\partial t^3} = v_A^2(x)\frac{\partial^3 v_i}{\partial z^2 \partial t} + \tilde{\nu}_{in}(x)\left[\tilde{\nu}_{in}(x)\left(\frac{\partial v_n}{\partial t} - \frac{\partial v_i}{\partial t}\right)\left(-\frac{\rho_i(x)}{\rho_n(x)} - 1\right)\right] + \tilde{\nu}_{in}(x)\zeta_n\nabla^2\frac{\partial v_n}{\partial t} - \tilde{\nu}_{in}(x)\zeta_i\nabla^2\frac{\partial v_i}{\partial t} - \tilde{\nu}_{in}(x)v_A^2(x)\frac{\partial^2 v_i}{\partial z^2} + \zeta_i\nabla^2\frac{\partial^2 v_i}{\partial t^2}. \tag{B.12}$$

We now rearrange Equation (B.10) to form

$$\tilde{\nu}_{in}(x)\left(\frac{\partial v_n}{\partial t} - \frac{\partial v_i}{\partial t}\right) = \frac{\partial^2 v_i}{\partial t^2} - v_A^2(x)\frac{\partial^2 v_i}{\partial z^2} - \zeta_i\nabla^2\frac{\partial v_i}{\partial t}. \tag{B.13}$$

We then substitute Equation (B.13) in to Equation (B.12) to give

$$\frac{\partial^3 v_i}{\partial t^3} = v_A^2(x)\frac{\partial^3 v_i}{\partial z^2 \partial t} + \tilde{\nu}_{in}(x)\left[\left(\frac{\partial^2 v_i}{\partial t^2} - v_A^2(x)\frac{\partial^2 v_i}{\partial z^2} - \zeta_i\nabla^2\frac{\partial v_i}{\partial t}\right)\left(-\frac{\rho_i(x)}{\rho_n(x)} - 1\right)\right] + \tilde{\nu}_{in}(x)\left[\zeta_n\nabla^2\frac{\partial v_n}{\partial t} - \zeta_i\nabla^2\frac{\partial v_i}{\partial t} - v_A^2(x)\frac{\partial^2 v_i}{\partial z^2}\right] + \zeta_i\nabla^2\frac{\partial^2 v_i}{\partial t^2}. \tag{B.14}$$

We then rearrange Equation (B.10) in secondary way to form

$$\frac{\partial v_n}{\partial t} = \frac{1}{\tilde{\nu}_{in}(x)}\left(\frac{\partial^2 v_i}{\partial t^2} - v_A^2(x)\frac{\partial^2 v_i}{\partial z^2} - \zeta_i\nabla^2\frac{\partial v_i}{\partial t} + \tilde{\nu}_{in}(x)\frac{\partial v_i}{\partial t}\right). \tag{B.15}$$

We then substitute Equation (B.15) in Equation (B.14) to give an equation that describes the temporal and spatial variation of the ion velocity perturbation, v_i, in the form

$$\frac{\partial^3 v_i}{\partial t^3} = v_A^2(x)\frac{\partial^3 v_i}{\partial z^2 \partial t} + \tilde{\nu}_{in}(x)\left[\left(\frac{\partial^2 v_i}{\partial t^2} - v_A^2(x)\frac{\partial^2 v_i}{\partial z^2} - \zeta_i\nabla^2\frac{\partial v_i}{\partial t}\right)\left(-\frac{\rho_i(x)}{\rho_n(x)} - 1\right)\right] + \tilde{\nu}_{in}(x)\left[\zeta_n\nabla^2\left(\frac{1}{\tilde{\nu}_{in}(x)}\left(\frac{\partial^2 v_i}{\partial t^2} - v_A^2(x)\frac{\partial^2 v_i}{\partial z^2} - \zeta_i\nabla^2\frac{\partial v_i}{\partial t} + \tilde{\nu}_{in}(x)\frac{\partial v_i}{\partial t}\right)\right)\right] - \tilde{\nu}_{in}(x)\left[\zeta_i\nabla^2\frac{\partial v_i}{\partial t} + v_A^2(x)\frac{\partial^2 v_i}{\partial z^2}\right] + \zeta_i\nabla^2\frac{\partial^2 v_i}{\partial t^2}. \tag{B.16}$$

After some algebra and introducing $\chi = \rho_i(x)/\rho_n(x) = \text{constant}$, Equation (B.16) reduces to

$$\frac{\partial^3 v_i}{\partial t^3} = v_A^2(x)\frac{\partial^3 v_i}{\partial z^2 \partial t} - \tilde{\nu}_{in}(x)\frac{\partial^2 v_i}{\partial t^2}(\chi + 1) + \tilde{\nu}_{in}(x)v_A^2(x)\chi\frac{\partial^2 v_i}{\partial z^2} + \tilde{\nu}_{in}(x)\zeta_n\nabla^2\left(\frac{1}{\tilde{\nu}_{in}(x)}\left\{\frac{\partial^2 v_i}{\partial t^2} - v_A^2(x)\frac{\partial^2 v_i}{\partial z^2} - \zeta_i\nabla^2\frac{\partial v_i}{\partial t} + \tilde{\nu}_{in}(x)\frac{\partial v_i}{\partial t}\right\}\right) + \zeta_i\nabla^2\frac{\partial^2 v_i}{\partial t^2} + \tilde{\nu}_{in}(x)\zeta_i\chi\nabla^2\frac{\partial v_i}{\partial t}. \tag{B.17}$$

This equation is solved using the numerical techniques described in Chapter 3 and the results are presented in Chapter 6.